Enhanced Navigation and Tether Management of Inspection Class Remotely Operated Vehicles

by

Jonathan Zand
B.A.Sc., University of British Columbia, 2005

A Thesis Submitted in Partial Fulfillment
of the Requirements for the Degree of

MASTER OF APPLIED SCIENCE

in the Department of Mechanical Engineering

Enhanced Navigation and Tether Management of Inspection Class Remotely Operated Vehicles

by

Jonathan Zand
B.A.Sc., University of British Columbia, 2005

Supervisory Committee

Dr. Bradley Buckham, (Department of Mechanical Engineering)
Co-Supervisor

Dr. Daniela Constantinescu, (Department of Mechanical Engineering)
Co-Supervisor

Dr. Afzal Suleman, (Department of Mechanical Engineering)
Departmental Member

Abstract

Supervisory Committee
Dr. Bradley Buckham, (Department of Mechanical Engineering)
Co-Supervisor
Dr. Daniela Constantinescu, (Department of Mechanical Engineering)
Co-Supervisor
Dr. Afzal Suleman, (Department of Mechanical Engineering)
Departmental Member

Remotely Operated Vehicles (ROVs) provide access to underwater environments too deep and dangerous for commercial divers. A tether connects the ROV to a vessel on the surface, providing power and communication channels. During extended manoeuvres, hydrodynamic forces on the tether produce large tensions which hinder ROV manoeuvrability. The research presented in this thesis focuses on the design of new tether management strategies that alleviate the tether disturbance problem, and the implementation of a navigation suite for tracking the ROV position and velocity which are needed to close the loop on the tether management method. To improve the estimation of the ROV state, an Extended Kalman Filter (EKF) is developed.

An inspection class Falcon™ ROV was used for this research. Typical of the ROVs in its class, the Falcon™ ROV has a neutrally buoyant tether which reacts to hydrodynamic forces that accumulate over its length when exposed to currents or when the ROV attempts to move at high speed. Dynamics models of the ROV and the tether were utilized in numerical simulations of deepwater Falcon™ operations and were also embedded in the process model of the EKF. The parameters of these Falcon™ dynamic models, including the propulsive thrusts, hydrodynamic drag forces and added masses, were identified through a series of shallow water tests. The physical parameters of the ROV tether were measured in a dry laboratory.

Transect and transit manoeuvres at 200m depth were investigated through numerical simulation of the tether and ROV. The position of the ship relative to the ROV was optimized to minimize steady-state tether disturbance for transect manoeuvres and to maximize sustained transit speed for transit manoeuvres. Driving the ship to lead the ROV by 26m was found to be optimal for the transect manoeuvres at 200m depth. At the 0.2m/s transect speed, this optimal configuration produces 25N of tether disturbance, whereas the conventional method was shown to produce tether disturbances up to 43N. The fastest sustainable ROV transit speed for operations at 200m depth with the neutrally buoyant tether was found to be 0.67m/s and was obtained by driving the ship 90m ahead of the ROV. Beyond this speed, the demanded ROV thrust exceeds capacity during long transits. However, attaching a depressor mass to the otherwise neutrally buoyant tether provides more control of the tether profile through ship motion. With use of a depressor, controlled ship and winch motion further reduce tether disturbance and allowed ROV transit speeds exceeding 1m/s.

A navigation suite was developed to track ROV position and velocity with the accuracy and frequency necessary for the proposed tether management strategies. The Falcon™ ROV was instrumented with an acoustic positioning system, a Doppler Velocity Log (DVL), a depth sensor, a compass, and an Inertial Measurement Unit (IMU). Asynchronous measurements from the individual devices were processed with an EKF that used a kinetic model of translational motion to blend the data into a single estimate of the vehicle state. The EKF performance was tested experimentally with measurements collected during a shallow water test. The accuracy of the EKF estimate of ROV position was quantified through comparison with optical motion measurements. The optical

motion measurement system accurately tracked ROV position at 100Hz, but needed optical markers mounted to a mast on the ROV to be above the water surface, restricting the test domain to shallow water.

ROV operations are typically beyond commercial diver depth, so the shallow water test results were extended to deepwater operation by applying the EKF to numerically simulated instrument measurements generated for a 200m deep ROV manoeuvre. The EKF estimated ROV position at 10Hz with root mean square (RMS) errors less than 3.5m. The ROV velocity was also estimated at 10Hz with RMS errors less than 0.04m/s.

Table of Contents

List of Tables

List of Figures

Acronyms

Symbol	Description
AUV	Autonomous Underwater Vehicle
DC	Direct Current, Constant Voltage
DOF	Degree of Freedom
DVL	Doppler Velocity Log
EKF	Extended Kalman Filter
GPS	Global Positioning System
HUGIN	High Precision Untethered Geosurvey and Inspection System
IMU	Inertial Measurement Unit
INS	Inertial Navigation System
KF	Kalman Filter
LBL	Long Baseline Acoustic Positioning System
LED	Light Emitting Diode
MMQ	Miniature MEMs Quartz
MRU	Motion Reference Unit
PID	Proportional Integral Derivative
RK45	Runge Kutte 4^{th} order adaptive integration algorithm
RMS	Root Mean Square
ROPOS	Remotely Operated Platform for Ocean Science
ROV	Remotely Operated Vehicle
ROVM	Remotely Operated Vehicle Manipulator
RPM	Rotations Per Minute
RS485	Recommended Standard 485
SBL	Short Baseline Acoustic Positioning System
USBL	Ultra Short Baseline Acoustic Positioning System
UUV	Unmanned Underwater Vehicle - Either ROV or AUV

Acknowledgments

The efforts, suggestions, and companionship of many others contributed to the success of this work. I would like to thank Dr. Brad Buckham for his immense support and thoughtful guidance throughout the project. Dr. Daniela Constantinescu also provided support and guidance for which I am very grateful. I wish you both continued success in your research careers.

Suboceanic Sciences Canada Ltd. generously provided access to their Falcon™ ROV. Mike Wood, Suboceanic director of operations, imparted an ROV operator's perspective, providing a practical foundation for research goals. Hopefully this work can be applied to your future missions to ease your operations and expand your capabilities.

The team at Dynamic Systems Analysis Ltd. provided software implementation and technical support for numerical simulations. Dean's Kalman research provided a starting point, and his software for multi-threaded measurement collection was tremendously useful for the project. Ryan's tireless maintenance and development of the ProteusDS™ software provided a powerful framework for numerical simulations of the ROV and tether dynamics.

I also thank friends and fellow researchers who provided a helping hand. Some, such as Serdar, Kerem, and Bonnie, spent many late evenings with me in a cold and dark boathouse doing 'just one more' set of wet tests. Off topic discussions with my office mates, Scott and Clayton, on renewable energy viability and day to day ordeals provoked many creative thoughts. May we all find some warm sunny days to go for a sail.

Chapter 1. Introduction to Remotely Operated Vehicles

1.1 Unmanned Underwater Vehicles and Applications

Marine environments cover most of the earth's surface and contain an abundance of fascinating biological, geophysical and manmade components. At great depths, hydrothermal vents and ocean crust formations continue to intrigue scientists in a range of disciplines. Unfamiliar species living in the deep ocean and their abilities to survive in such an extreme environment are the focus of many biologists. Industrial projects, from underwater mining to trans-continental communication lines have provided abundant resources and advanced technological capabilities. Modern industrial projects and scientific research demand interaction with the deep sea.

Much underwater research and development is conducted in the shallower coastal regions. The regulation of commercial and recreational fisheries is challenged by the difficulty of surveying aquatic life over sustained time periods. With the emergence of aquaculture farms and other floating commercial operations comes a need for monitoring the environmental impacts on nearby habitats. The assessment of seafloor terrain for mooring design and cable and pipe routing requires detailed geographic surveys. Maintenance, repairs, and non-destructive testing of floating installations and their moorings often requires accessing and observing submerged equipment.

Employing commercial divers remains the most adept approach for performing the complex installation, surveillance and maintenance of costal infrastructure. However, the pressure encountered, even in a coastal domain, pushes the human body to its functional limit. Commercial divers with surface supplied air are limited to 60m safe working depths. Deeper dives can be performed with the use of mixed gas and lengthy decompression periods, but add considerable cost in equipment and risk. Obviously, an (Unmanned) Underwater Vehicle (UUV) that can perform the required task is a much safer alternative in shallower waters and is a required alternative for deeper waters. Even within shallow waters, the operation of a mobile and navigable UUV is free of the fatigue constraints faced by a human diver.

The electromagnetic waves which work so well for above surface communication are highly attenuated in water. Acoustic waves can be efficiently transmitted, but multi-path reflections, ambient noise, the slower translational speed, and the limited bandwidth of acoustic telemetry systems combine to hinder the effectiveness of acoustic communication. Acoustic modems are capable of sending simple UUV command signals [1], but suffer from considerable transmission delay and are not able to provide the real-time video feedback a human pilot requires to make control decisions.

Some submerged data collection tasks can be completed with Autonomous Underwater Vehicles (AUVs) like the ones shown in Figure 1-1. These vehicles are usually a streamlined torpedo shaped, with a single thruster for surge propulsion. Their motion is predominantly in surge, with yaw and pitch controlled with actuated fins. Their autonomous nature makes them well suited for long missions of simple predetermined tasks, but their reliance on an onboard power supply with limited capacity necessitates

efficiency. Ocean gliders [2] reduce energy consumption for low speed missions by using buoyancy control and pitch control to generate lift that provides horizontal motion with the use of the vertical buoyancy force. Currently, low level controllers [3, 4, 5] and high level mission planners, otherwise referred to as autonomous agents [6, 7, 8], can be combined to execute generic surveying missions with AUVs. However, more complex tasks requiring human pilot involvement must be performed with another class of unmanned underwater vehicle - submerged Remotely Operated Vehicles (ROVs).

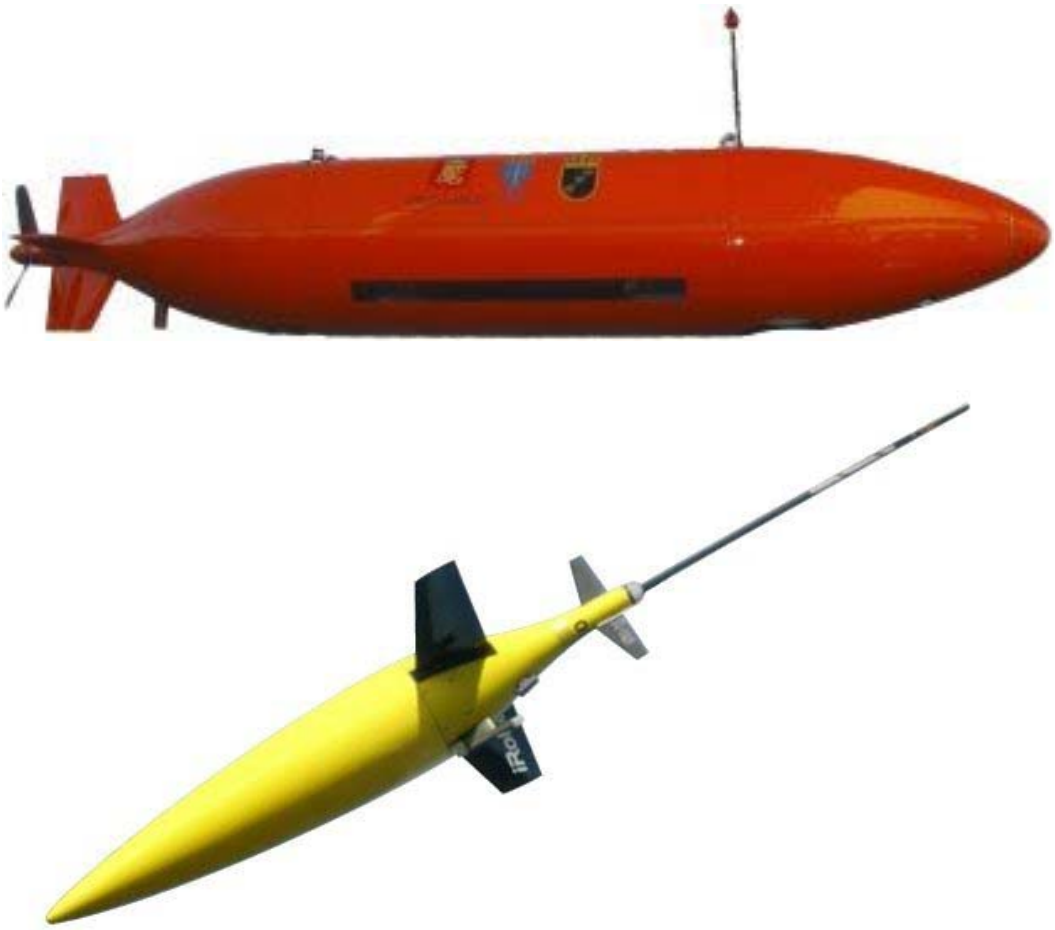

Figure 1-1. Commercial AUV Products. Top: the HUGIN™ AUV manufactured by Kongsberg Maritime uses a single transom mounted thruster for surge propulsion and four individually controlled rudder blades for heading, pitch, and roll control. Bottom: the Seaglider™ manufactured by iRobot varies its buoyancy to glide through the water column over month long missions. Images courtesy of http://auvac.org/resources/configuration.

Submerged ROVs use a tether to physically connect the ROV to the pilot's surface station. The tether provides power and high-bandwidth telemetry for the ROV. Cameras provide video feedback to the pilot, who controls the motion of the ROV through actuation of several onboard propeller type thrusters. ROVs are also fitted with lights to illuminate their surroundings viewed by the video camera. Manipulators, navigation sensors, and scientific instruments can also be fitted to ROVs to achieve specific tasks.

The collective power and telemetry requirements of these devices reinforce the necessity of the tether. Several commercially available ROV products are shown in Figure 1-2.

a)ROPOS™ HYSUB™ 40 work-class ROV
(http://www.ROPOS.com)

b) Falcon™ inspection class ROV
(http://www.cdis.ae/marine_02p.html)

c)VideoRay™ inspection class ROV
(http://www.videoray.com)

Figure 1-2. Commercial ROV Products.

ROVs are designed for unsteady, omni-directional motion, with actuation, stability and functionality constraints requiring a more bluff and open frame shape than the streamlined AUVs. These remotely piloted vehicles range in size from small hand-held inspection class to the multi-ton work class ROVs. Inspection class ROVs are primarily used for visual observations of submerged objects. They typically have a 1cm diameter neutrally buoyant tether and operate at depths up to 300m. Work class ROVs are capable of full ocean depth operations and are fitted with multiple tools including manipulators to interact with the underwater environment. These large ROVs required large and costly surface equipment to support them. The large power budget of a work class ROV is met by high voltage transmission through kilometre scale tethers with diameters exceeding 2cm. These tethers are negatively buoyant, and are often used in conjunction with a

depressor or submerged tether management system to mitigate the tether's influence on the ROV dynamics.

The portability and lower operating costs of inspection class ROVs make them more desirable to employ than work class ROVs. However, work class ROVs are more adept at manoeuvring in large currents and are fitted with sophisticated navigation sensors for ROV position tracking. Improving the manoeuvrability and position tracking of inspection class ROVs will expand the tasks which they can fulfill, and reduce the cost of conducting the coastal operations mentioned earlier.

1.2 Tether Disturbance, ROV Control and Tether Regulation

The tether, which is essential in providing the remote human control of the ROV for complex tasks, has some drawbacks. It can tangle or snag on submerged objects. During ROV operations, hydrodynamic forces accumulate on the tether, either due to currents or motion of the ROV, that limit ROV manoeuvrability and, in extreme cases, overpower the ROV thrusters. Even during normal operation, tether disturbance significantly affects the ROV dynamics. To compensate the tether disturbance, sophisticated adaptive controllers [9, 10] or high feedback gains [11] have been employed. In most cases, the ROV pilot's experience and intuition are relied on to maintain a tolerable ROV tether configuration.

Proper tether management is necessary to mitigate the tether disturbance and ensure controllability of the vehicle. Unfortunately, without significant alteration to the typical tethered ROV system, the only means to shape the tether profile, and thus reduce the tension at the ROV connection, is positioning of the surface ship and active control of the tether winch on the surface vehicle. As such, complete control of the tether is impossible

and the intelligent use of the ship and winch can only seek to regulate the tether profile to reduce the tether disturbance. Work class ROVs have the infrastructure, thrust capacity, and negatively buoyant tethers to operate without being exceedingly hindered by tether disturbance. On the other hand, inspection class ROVs have lower thrust capacity and neutrally buoyant tethers, and often deal with relatively larger drag forces due to the search manoeuvres they conduct and the tidal flows they encounter in coastal waters. By using the surface ship and winch to regulate tether disturbance on inspection class ROVs, one could increase the maximum transit speed of a small ROV and improve low speed manoeuvrability in the face of high ambient current.

1.3 ROV Navigation

Accurate tracking of the ROV position is vital to almost all ROV operations. In survey and search missions, the location of significant features noted by the human pilot through the video cameras must be recorded. The first part of submerged object recovery is locating the object with the ROV. Without accurate ROV position reporting, it is nearly impossible to locate a submerged object. Poor visibility, marine growths, and sediment deposits surround the object and hinder sighting the object even if the object's position is well known. When the exact location of an object is not known, the ROV must cover large areas to search for it. Position tracking allows efficient search paths to be traversed – the ROV operator can avoid significant overlap in the search pattern. Once the ROV has accurately located the object, it can return to the surface to be fitted with a retrieval device, such as a carabineer with retrieval line and directly return to the located object.

The ROV position, velocity and orientation provide the necessary feedback for advanced ROV controllers [9, 10, 11]. Model based ROV controllers rely on parametric

approximations to the ROV hydrodynamics and there are several dynamic parameters that must be estimated. The uncertainty in these parameters, as well as large unknown disturbances (tether disturbance or forces due to unknown currents) necessitates the use of accurate navigation information as feedback. Furthermore, navigation feedback for ROV controllers must be accurate and without delay to avoid unstable oscillations and overshoots in the ROV motion. Accurate real-time navigation data also improves the performance of a human pilot during manual operation by providing the pilot with up to date ROV state estimates that facilitate faster decision making. In the context of tether management, navigation data allows better tether regulation by providing a real-time estimate of the relative location of the ROV to the surface ship.

The aquatic environment in which ROVs operate renders many of the land based navigation techniques ineffective. Underwater navigation systems are discussed in the next three subsections.

1.3.1 Acoustic Positioning

The same electromagnetic signal attenuation that necessitates the use of a tether also renders the satellite GPS unusable for underwater position tracking. Acoustic systems analogous to GPS can be used, but are tedious to deploy, and can contain significant measurement error.

Acoustic positioning operates on similar principles as GPS, but requires local reference transducers transmitting acoustic waves instead of satellites emitting electromagnetic waves. Also, since the reference stations (transducers) are local to the tracking target, most acoustic positioning systems operate on a repeated ping, while GPS transmits a continuously varying signal. The range between an ROV mounted transducer and a

reference station is calculated from the time for acoustic waves to travel between the two transducers. The ranges from the ROV transducer to several reference stations are used to trilaterate ROV position.

Several reference station configurations are common, each with their own merits. Long Base Line (LBL) configurations consist of stationary reference stations distributed throughout the survey area, and are perhaps the most accurate, but most tedious to set up. Short Base Line (SBL) configurations space the reference stations apart on the surface vessel, where they can be permanently mounted, but accurate surface vessel position and orientation measurements are needed to make accurate ROV measurements in earth fixed coordinates. Ultra Short Baseline (USBL) systems contain all the reference transducers in a single instrument and rely on phase lag to resolve direction to the ROV transducer. Like SBL systems, accurate tracking of the USBL reference instrument's position and orientation is needed for useful ROV position tracking. Reference station locations and acoustic paths for LBL and SBL configurations are depicted in Figure 1-3.

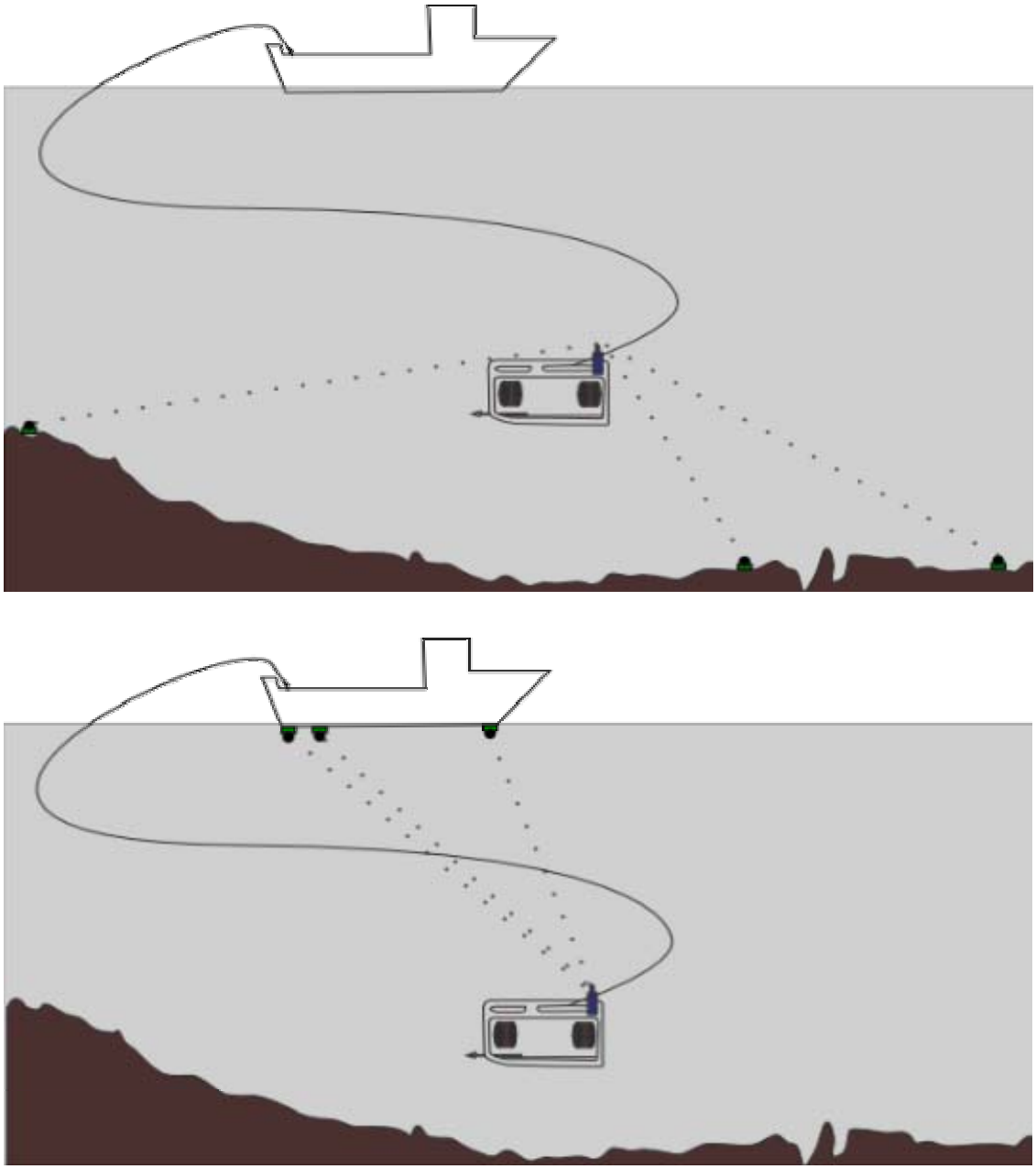

Figure 1-3. Acoustic Positioning Configurations. Top: LBL systems have reference stations set on the seafloor with large spacing and require re-calibration at each survey site. Bottom: SBL systems have reference stations mounted to the ship, making the system easy to move between sites, but reference station spacing is limited by ship size. USBL systems also have a reference station mounted to the ship.

Regardless of system configuration, acoustic positioning measurements are prone to errors in reference station locations, sound speed estimation, and multi-path signals.

Also, acoustic range measurements can contain considerable delay, due to the travel time between the reference station and target transducer.

1.3.2 Dead Reckoning and Inertial Navigation

The velocity and acceleration of ROVs can be measured with onboard sensors. With either of these measurements, the progression of ROV position can be calculated with kinematics.

The ROV velocity is most readily measured by an onboard sensor that provides speeds in the surge, sway, and heave directions of the vehicle. Flow sensing meters (such as paddle wheels and hotwires) measure velocity relative to the ambient water velocity. A Doppler Velocity Log (DVL) finds the over ground velocities by measuring the frequency shift of echoes off the seafloor.

Vehicle heading is commonly measured with flux gate magnetometers functioning as a compass. The three dimensional magnetic field is measured, and the projection on the horizontal plane reveals the angular offset from magnetic north. The horizontal plane can be resolved with a tilt sensor. Accelerometers used to resolve the direction of gravity can also provide the tilt of the vehicle. In addition to horizontal plane errors, local environmental magnetic anomalies and magnetic field disturbances from onboard equipment degrade the accuracy of the compass.

The compass's measurements of ROV orientation can be used to rotate the ROV velocity measurements made by the DVL in the body fixed coordinates to rates of change of the vehicle's position. Integration of these values with time produces the dead reckoning estimate of ROV position. The integration process provides high frequency

estimates and smoothes random measurement fluctuations, but accumulates systematic bias errors of the velocity and heading measurements

Similar to dead reckoning, self contained Inertial Navigation Systems (INS) integrate measurements of linear acceleration and rotational velocity measured by an Inertial Measurement Unit (IMU) to calculate ROV position and velocity. However, due to the double integration with time, INS position calculations are even more sensitive to measurement bias than dead reckoning estimates. Gravitational acceleration must be taken out of the IMU acceleration measurements, requiring accurate tracking of the ROV orientation. As such, INS systems require an IMU with high quality gyroscopes. Ring laser and fibre-optic gyroscopes are sufficiently accurate for this task, and can detect the earth's angular velocity to bound the error on the heading estimate calculated from integrated yaw rates. Complementary filtering of the ROV rotation rate measurements and the inertial acceleration measurements is used to estimate the ROV velocity and orientation. Dead reckoning can be applied to the INS estimates of ROV velocity and orientation to estimate ROV position. However, external position sensors are required to reset the error accumulation of the estimated position and translational velocity.

1.3.3 Extended Kalman Filtering

Slow and noisy acoustic positioning measurements can be combined with high frequency but error accumulating dead reckoning and INS measurements via complementary filtering to improve navigation estimates. Kalman filtering [12] is a commonly used complementary filter. Its blending criteria aim to minimize error variance in its estimate based on estimates of measurement and process uncertainties. The Kalman Filter (KF) includes a state transition matrix to evolve the filter's state with

time, and then corrects state errors with available measurements while keeping track of the state's uncertainty. For states with nonlinear dynamics, an Extended Kalman Filter [13] (EKF), can be used to calculate the varying state transition matrix.

1.4 Research Objectives

This work aims to improve the operating capabilities of inspection class ROVs working in coastal regions. The Falcon™ shown in Figure 1-2(b) is the ROV used in this work. Access to a Falcon™ was shared with Suboceanic Sciences Canada Ltd, which provides ROV services to BC's coast and around the world. The Falcon™ is small enough to be easily transported and launched while sufficiently powerful to perform light interaction with submerged objects. These ROVs are currently navigated by dead reckoning from a buoy line with the use of a compass and depth sensor. More sophisticated sensors, providing position, speed, and orientation will be fitted to the ROV. Navigation performance is enhanced to simplify mission planning, to provide position tracking, and to generate the feedback required by automatic ROV controllers. Also, a means to regulate the tether position and mitigate the tether disturbance is addressed to expand the ROV manoeuvrability and the range of allowable operating sea states. The technical objectives are as follows:

1. Identify the parameters of a Falcon™ ROV. These parameters are needed to conduct numerical simulations of the ROV dynamics. Simulations are necessary for developing, testing, and refining the other objectives. The navigation system will include a dynamics model that also requires some of these parameters. The parameters will be identified by piloting the Falcon™ ROV through a series of test

manoeuvres and recording velocity and acceleration data. This data will be used in a sequential parameter identification process.

2. Develop tether management schemes. Ship and winch activity which mitigates tether disturbance during both low speed transects and high speed transits will be developed through numerical simulation. The relationship between the ship position relative to the ROV and the steady-state tether disturbance will be mapped to find operating configurations with minimal tether disturbance. The benefit of using a depressor mass on the ROV's neutrally buoyant tether will be investigated.
3. Develop an EKF for sensor fusion. ROV navigation with low noise and high update rate will be achieved by blending the measurements of an acoustic positioning system, a DVL, a low cost IMU, a compass, and a depth sensor. A kinetic model of the ROV will be embedded within an EKF to further reduce navigation uncertainty. EKF performance will be demonstrated with experimental shallow water testing and simulation results of full scale deployments.
4. On-line identification of the tether disturbance forces. Tether disturbance will be included as an EKF state, and its evolution with time will be coarsely modeled within the ROV kinetic model embedded in the EKF. Since no load-cell is installed on the ROV to provide tether disturbance measurements, the EKF will refine its estimate using the mismatch between model dynamics and measured dynamics.
5. Experimental testing of the EKF navigation system on an inspection class ROV. The ROV will be fitted with an IMU, a DVL, a compass, and an SBL target transducer. A shallow water test facility will be setup to provide a protected environment in which to pilot the ROV through a series of test manoeuvres. An optical motion

measurement system will be used at this facility to accurately track the ROV position. The optical measurements will be used to evaluate the accuracy of the EKF's estimate of ROV position during the shallow water tests.

1.5 The ROV Simulation Platform

Given the depth constraints of the test facility being used for the experimental EKF development, a numerical simulation of the Falcon™ ROV system was used throughout this research whenever full scale, or deepwater, operation of the ROV was considered. The tether management scheme will be designed through simulation studies and the tether management scheme and navigation algorithm will be tested in deepwater conditions via simulations.

Perhaps the most difficult component of the ROV to simulate is the tether disturbance force, as it depends on the non-linear dynamics of a highly variable tether shape. In this research, the ProteusDS™ simulation package, created and maintained by Dynamic Systems Analysis Ltd., was used to simulate the ROV system during deepwater operations. In the ProteusDS™ simulations, the tether is modeled as a variable length cable using a finite cable element unique to the ProteusDS™ code [14, 15]. The ROV is modeled as a six Degree of Freedom (DOF) rigid body with the five thrusters modeled as equivalent point loads [16]. The ProteusDS™ simulation package handles the interaction between these objects and propagates the system through time with an adaptive 4^{th} order Runge-Kutta integration algorithm (RK45). The state of the surface ship and winch are specified as kinematic inputs.

Parameters of the Falcon™ system, such as tether stiffness and ROV hydrodynamic coefficients are measured during parameter estimation tests and passed to the

ProteusDS™ simulation as constants. Though much effort is necessary to accurately determine and numerically model the dynamics, once in place, they allow the simulation to predict the detailed behaviour of the ROV system over a large range of operating scenarios.

1.6 The Experimental ROV Platform

The Falcon™ ROV is an inspection class ROV manufactured by Saab Seaeye. The system consists of the subsurface vehicle, tether, and surface station as shown in Figure 1-4. Suboceanic Sciences Canada Ltd. typically uses the Falcon™ ROV for marine surveys and sunken object recoveries. Marine surveys include aquaculture impacts on nearby marine ecosystems, anchor line inspections, and bathymetry mapping for pipeline routing. Retrieved objects include sunken boats, nets, scientific instruments, and other ROVs.

Figure 1-4. Seaeye Falcon™ ROV System

The subsurface vehicle has a 300m depth rating, which allows it to access most coastal seafloors, even those far beyond the reach of commercial divers. The ROV has a mass of 50kg, making it easy to deploy with the help of a davit, or can even be hand launched from a low platform such as a swim grid. Four electric thrusters are vectored in the vehicle's horizontal plane, allowing responsive and powerful surge, sway, and yaw manoeuvres. A fifth electric thruster is oriented vertically near the middle of the vehicle to provide depth control of the typically neutrally buoyant vehicle. A single-function manipulator can retrieve small submerged objects or can attach a winch line to heavier

objects. A 5-function hydraulic manipulator arm is also part of the system, allowing more dexterous tasks. The onboard navigation pod houses a compass, a gyroscope, and a depth sensor. A passive sonar unit indicates the presence of nearby objects.

The ROV is connected to the ship via a tether containing power and telemetry lines. Typical Falcon™ tethers are 350m long with neutral buoyancy in salt water and sink slowly in fresh water. The supply voltage is boosted through the tether to mitigate line losses, while a Line Insulation Monitor closely tracks the current and quickly shuts the system down in the event of a fault. Falcon™ telemetry runs on an RS485 network, with the network signals distributed to each individual device. Each device receives all the network packets, but only responds to those specifically addressed to it. Standard Falcon™ tethers contain three sets of twisted pair wires for telemetry, sonar, and video signals, in addition to the power lines.

The surface station provides an interface for the human pilot onboard the surface vessel. A video screen displays the environment in front of the ROV. A hand controller contains a joystick for horizontal thrust control, dials for vertical thrust and camera tilt, along with other buttons for light intensity, manipulator control, and auto-heading and auto-depth activation. A sonar display reveals nearby objects and houses controls for range and refresh rate.

Typical of ROVs in its class, the Falcon™ does not have a position tracking system. The only navigation measurements available to the pilot are the onboard compass and depth sensor. Position estimation is made by following a sightline located with GPS from the surface to the seafloor. The pilot then follows a compass heading while

hovering close to the seafloor and visually estimates the ROV velocity to dead reckon ROV position.

In developing the navigation suite, a DVL, an IMU, and a compass are integrated with the Falcon™ vehicle. In addition, an acoustic transducer is attached to the vehicle. To support this research, additional data channels were added by upgrading the tether to a fibre-optic option and multiplexing the signals into a single fibre-optic line to send the additional sensor measurements to the surface. A Panasonic Toughbook™ tablet PC is added to the surface station to collect the sensor data, track the thruster commands, and run the navigation algorithm.

1.7 Literature Review

Previous works relevant to tether management and underwater navigation are discussed in this section. Tether management is closely related to positioning the deep end of a submerged cable with ship and winch activity, so works of this nature are also reviewed. Underwater position tracking and methods to improve its accuracy and update frequency are reviewed in Subsection 1.7.2.

1.7.1 Tether Management

The influence and control of ship position and tether payout on positioning the submerged end of a tensioned cable have been previously investigated through several approaches. Chauvier et al. [17] developed optimization routines to schedule ship motion and the winch payout that minimize the time taken for a towfish to pass through a predefined set of waypoints. Later, Williams [18] used inverse cable dynamics to generate the ship and winch activity necessary to produce the desired towed vehicle dynamics. However, the open-loop methods of [17] and [18] are not able to adjust for the

detrimental effects of unmodeled forcing such as ocean currents. Prabhakar [15] presented a Dahlin controller [19] that uses discrete acoustic positioning measurements to adjust ship motion and winch activity to keep a point on a negatively buoyant ROV tether at a desired location.

In [15], Prabhakar showed that controlling ship motion and winch activity such that the ROV end of the tether follows the ROV trajectory can mitigate the tether disturbance. However, the "water-pulley" effect discussed by Delmer et al. in [20] introduces delay in off-axial motion of the tether. This delay is prolonged in neutrally buoyant tethers, such as that of the Falcon™, to the point where positioning of the ROV end of the tether by ship and winch motion alone is impossible.

For work class ROVs with negatively buoyant cables, one means of reducing tension at the ROV is to induce an inverted catenary into the tether profile near the ROV. Prabhakar [15] used simulations to position small floats along the heavy ROV cable to create the catenary. Ship and winch activity was used to position the ship side of the catenary a fixed distance away from a station-keeping ROV subject to a current. Similar methods of mitigating tether disturbance on the Falcon™ and other inspection class ROVs with neutrally buoyant tethers can be achieved with the use of a depressor mass attached to the tether a short distance away from the ROV. This graduate research [21] has expanded upon Prabhakar's work in cable positioning by establishing a schedule for desirable depressor mass positions. This schedule is employed in transit manoeuvres.

1.7.2 Underwater Position Tracking

Underwater position tracking is complicated by the attenuation of electromagnetic waves including those used by GPS. Acoustic positioning has slow update rates and

exhibits significant measurement uncertainty. Typically a beacon's position has been trilaterated using range measurements to several reference stations based on acoustic wave travel-time [22]. Measurement noise has also been mitigated with the use of more sophisticated position calculations, such as using an EKF to blend the beacon position information contained in each of the range measurements [23]. However, with just range measurements, the EKF must assume a velocity progression in-between range measurements, causing infrequent position updates.

Many ROV operations require more accurate position tracking, as do automatic control and regulation schemes. Position tracking has been improved through incorporating the measurements of additional sensors into the position estimate [24]. Velocity measurements made by a DVL [25] or a flow meter [26] provide higher frequency measurements, and have been integrated over time to improve the position estimate. On work class ROVs, INS units comprised of three orthogonal accelerometers and three orthogonal rate gyroscopes have been used [27, 28] to provide velocity and position estimates based on integrated acceleration measurements (after removing the gravitational bias from the accelerometers). Bias in the acceleration and angular velocity measurements accumulates during the integration process and produces drift errors in the INS measurements. Drift errors in INS have been stabilized by aiding the INS measurements with direct position and velocity measurements [29, 30, 31, 32, 26, 33, 34]. In those works, the velocity measurements are made in the body fixed coordinates, and were rotated into an earth fixed coordinate system before integrating to complement position measurements.

A KF with a kinematic model is perhaps the most commonly used complementary filter for underwater navigation. A predominant assumption in existing KF kinematic models [35, 36] is that the vehicle exhibits constant velocity, and this gross approximation is used to smooth actual velocity measurements made by instruments onboard the vehicle. The navigation system on Hydro-Quebec's ROV [25] rotated DVL measurements into the earth-fixed frame so that the kinematic relationship between velocity and position was linear and a KF could be used. Other approaches have embedded EKFs with models that align body-fixed velocity measurements with the navigation frame and integrate them with respect to time to augment the position estimate [28, 30, 33, 35]. Due to nonlinearity of the rotation, employing those dynamics models has required an EKF or other nonlinear filter.

Kinetic models have also been used to improve the KF estimate with knowledge of the system's dynamics. Existing EKF implementations in [37] and [38] included the calculation of AUV surge speed from propeller RPM to stabilize the position tracking from a single acoustic range sensor. Also in the AUV paradigm, a kinetic model of the HUGIN 4500 AUV was used to estimate body fixed velocities for correcting INS drift in a KF framework [39]. The external nature of the kinetic model in this implementation allowed the KF model to be linear, but did not produce the full error variance minimization that would be provided by an embedded kinetic KF model.

For ROV navigation, Steinke [16] has presented the only kinetic model used to enhance position tracking. Steinke used simulations to compare the merits of a KF and several EKF models for tracking the position of the work class ROPOS ROV. ROPOS uses the OCTANS INS, which has sufficient accuracy to measure the earth's rotation,

resolve heading and integrate acceleration to provide low drift velocity estimates. In [16], the performance of OCTANS eclipsed any improvements available from using a kinetic model with DVL measurements, especially in the presence of tether disturbances unknown to that kinetic model. However, inspection class ROVs such as the Falcon™ considered in this work are not operated with the budget or designed with the space to install an INS, so it is anticipated that an EKF employing a kinetic model will provide improved position tracking over the simpler kinematic KF implementation.

Infinite input response filters, such as the KF, recursively consider the entire measurement history in their estimation strategy, and provide good smoothing characteristics, but suffer from slow rejection of estimates with large errors. In particular, the KF places little emphasis on an inaccurate measurement with a correspondingly large uncertainty estimate, but an outlier measurement will taint the KF estimate for an extended duration. The slow rejection of estimate errors has been eliminated with a Receding Horizon adaptation of the KF in [40], but at the price of additional computational load. Outlier rejection has also been performed by pre-processing the measurements. The navigation suite for the Hemire ROV [28] roughly estimated the ROV position based on a simplified hanging depressor model, and rejected measurements outside a watch circle around that position.

The KF has also been used to estimate quantities not directly measured by a sensor. Error state formulations [41, 26, 29, 42] of the KF have estimated sensor biases by calculating the steady offset of sensor measurements from estimated values. One navigation suite [30] that has blended GPS, IMU, compass, depth, and DVL measurements using a kinematics based EKF has also included an estimate of water layer

velocity to avoid errors in velocity estimation when the DVL losses bottom lock. A flow rate sensor has also been used instead of a DVL [26]. However, the flow rate sensor required estimation of water current to improve the AUV position dead reckoning.

1.8 Thesis Contributions

This work aims to improve the capabilities of the Falcon™ through innovative tether management and enhanced position tracking. Tether management schemes are developed through numerical simulations that investigate the influence of ship position and tether payout on the tether disturbance force. This research also expands Steinke's simulation based EKF navigation study [16] for a work class ROV to an inspection class ROV and contributes experimental EKF navigation results. The technical contributions include:

1. EKF Implementation on an inspection class ROV. The first presentation with all of an acoustic positioning system, a DVL, and an IMU being added to the Falcon™ ROV and identification of Falcon™ dynamics parameters. This thesis presents the first experimentally implemented EKF with an ROV kinetic process model.
2. Ship and winch activity schemes to reduce tether disturbance. In developing tether management schemes, the influence of ship position on tether disturbance is quantitatively derived. Schemes to actively position the ship and control the winch are developed and compared through simulation to the conventional operating schemes. This is the first presentation for regulating disturbance from a neutrally buoyant tether. Operation with a depressor mass attached to the tether is also considered.

3. Online tether disturbance estimation with a navigation filter. The EKF kinetic model includes the tether disturbance, which is not measured by force sensors. An approximate model of the temporal propagation of this disturbance is derived, and then corrected with the dynamics mismatch observed by navigation sensor measurements.
4. Experimental validation of EKF performance. In prior work, experimental results have checked KF performance against GPS data [30]. In this work, optical position measurements are used to provide a reference with much higher accuracy and temporal resolution.

1.9 Thesis Overview

Tether management and ROV position tracking are discussed in the following chapters. Both numerical simulation and experimental testing are employed to develop methods and verify their performance.

Chapter 2 discusses tether management of the Falcon™ ROV's neutrally buoyant tether. The relative position of the ship and ROV is found to be an important influence on the tether disturbance, as is the scope of tether between the ship and ROV. This chapter also summarizes the tether management scheme first presented by Zand et al. [21] which increases ROV transits speeds by using ship and winch activity to regulate depressor position. The enhanced tether management control schemes rely on ROV position and velocity feedback. ROV position and velocity tracking is the subject of the remaining chapters.

Chapter 3 describes the installation of sensors on the ROV and the EKF process that blends measurements from multiple sensors to produce accurate ROV position and

velocity estimates at a high update rate. It also discusses the layout of sensors on the ROV and the communication lines which send the measurements to the surface station. The classical KF is modified to produce an EKF embedded with an ROV dynamics model that handles the model's nonlinearities and asynchronous arrival of measurements.

Chapter 4 presents the identification of the constant parameters of the EKF and the ROV model. Measurement noise is quantified through measurements made during shallow water tests where positions could be more accurately measured with an optical tracking system. Thruster output, hydrodynamic drag, and added mass coefficients are also experimentally measured using shallow water tests. Moreover, the uncertainty in the ROV model is quantified.

Chapter 5 discusses the experimental validation of the EKF through shallow water test measurements. Over the 1300s test, the EKF's estimate at 10Hz has a lower Root Mean Square (RMS) error than the stand-alone SBL measurements updated at 0.5Hz. The DVL is shown to significantly increase the EKF position accuracy. Experimental data is used to prove the filter could be implemented on a physical system and highly accurate optical position measurements are used to quantify the error in the EKF position estimate.

Chapter 6 describes testing the EKF with a simulated full scale manoeuvre. Estimates of the ROV position and velocity are compared against simulated values and found to be reasonably accurate even though the full deepwater configuration significantly degrades acoustic positioning accuracy. The EKF's estimate of tether disturbance is also reasonable, even without providing force measurements to the EKF algorithm

Chapter 7 summarizes the main achievements and research findings and discusses topics needing further research.

Chapter 2. Tether Management

The aim of tether management is to mitigate the tether's negative impact on ROV manoeuvrability. Conventional tether management practice for inspection class ROVs uses observations made only at the surface to coordinate piloting of the surface ship and tending of the tether. In this chapter, numerical simulation is used to investigate tether management schemes that exploit knowledge of the ROV position.

Section 2.1 describes the model of the Falcon™ ROV system used in the numerical simulation and the ROV manoeuvres simulated to demonstrate the tether management schemes. Section 2.2 introduces the conventional tether management scheme. Section 2.3 derives optimal ship locations (relative to a known ROV location) that minimize tether disturbance for sustained transects and maximize sustainable transit speed. The optimal ship locations calculated in Section 2.3 form the basis for advanced tether management schemes applied to the demonstration manoeuvres in Section 2.4. Applying a depressor mass to the otherwise neutrally buoyant tether allows for even higher sustainable transit speeds. Tether management for operation with a depressor was presented in a journal article by Zand et al. [21]. Section 2.5 summarizes the ship and winch regulation scheme developed in that article and applies the scheme to the transit demonstration manoeuvre.

2.1 Numerical Simulation of the ROV System

In this chapter, typical inspection class ROV manoeuvres are analysed using the ProteusDS™ numerical simulation methodology described in Section 1.5. The simulation framework is based on parametric dynamics models that are applicable to a wide range of submerged equipment. For this research, the ProteusDS™ underwater vehicle and cable models are tailored to reflect the dynamics of the Falcon™ ROV through identification of the vehicle and cable dynamics parameters. The following subsections discuss the simulation of the tether and vehicle components of the ROV system and the manoeuvres selected to demonstrate the tether management schemes.

2.1.1 Tether Simulation

The simulation uses a lumped mass finite element tether model [14]. The model includes axial, torsional and bending stiffness particularly prevalent in the slack tethers often encountered during ROV deployments. Payout and retrieval of the tether during a manoeuvre is simulated with use of a variable length tether element at the connection to the surface vessel [15]. The surface end of the tether is kinematically controlled to mimic the ship activity prescribed for the selected tether management scheme.

The tether length, diameter, and density were directly measured. The estimated normal drag coefficient was also used by [43], [14] and [44], and is based on the measured steady-state inclination angles achieved by a towed a cable at several towing speeds during ocean scale tests [45]. The tether stiffness coefficients were measured with force-deflection tests. The raw measurements are listed in Appendix B, and the resulting mechanical properties are listed in Table 2-1.

Parameter	Symbol	Value
Density	ρ_c	1025 kg/m^3
Diameter	d_c	0.014 m
Normal drag coefficient	C_D	1.65
Axial stiffness	EA	4.3 x 10^4 N
Torsional stiffness	GJ	0.4 Nm^2
Bending stiffness	EI	0.5 Nm^2
Length	L_{Tot}	350 m

Table 2-1. Falcon™ Tether Properties.

2.1.2 ROV Simulation

The ROV is modeled as a six DOF rigid body acted upon by tether disturbance, hydrodynamic drag, buoyancy, and thruster propulsion [16]. The force and moments generated at the attachment point of the tether on the ROV are calculated and applied to the two objects. Hydrodynamic drag force is modeled as a quadratic function of velocity. The Falcon™ ROV is trimmed for neutral buoyancy, so the simulated buoyancy forcing is equal to the weight of the ROV. Propulsive forces of the four horizontal thrusters and the single vertical thruster on the Falcon™ are modeled as equivalent point loads on the rigid body.

The experimental parameter identification for the Falcon™ ROV was conducted in a shallow water test facility as discussed in Section 4.3. The measured surge and heave thrust saturation limits were 401N and 124N respectively. The identified hydrodynamic drag coefficients are listed in Table 4-11 and the ROV inertias with added mass are listed in Table 4-12.

2.1.3 Demonstration Manoeuvres

Two manoeuvres are considered for evaluating the tether management methodologies. Both manoeuvres start with the ROV 200m directly below the ship with a 20N tension in the tether. The ROV waits at the starting position for 10s before traveling to the next waypoint 600m ahead while maintaining the 200m depth. One manoeuvre is a transect. Transects are performed at low speed (0.2m/s) to provide the ROV pilot sufficient time to identify and assess the surrounding environment. The other manoeuvre is a transit, where the ROV is driven to reach the final waypoint as quickly as possible.

An ROV controller embedded in the ProteusDS™ simulation software schedules the thruster activity that produces the desired ROV manoeuvre. To simulate the transect manoeuvre, the ROV controller uses Proportional-Integral-Derivative (PID) control to set surge thrusts that make the ROV surge speed approach the desired 0.2m/s transect speed until the ROV reaches the destination. To simulate the transit manoeuvre, the ROV controller attempts to apply maximum surge thrust within the constraints of maintaining correct ROV depth and heading.

2.2 Analysis of the Conventional Tether Tending Method

Typically the tether is tended to maintain a low tension at the surface. It is released when the tension measured at the surface rises and it is retrieved when tension decreases. For low currents and short manoeuvres, this methodology produces a mild tether pull on the ROV, allowing high manoeuvrability without dragging the tether along the seafloor.

Piloting the surface vessel to stay near the ROV prolongs the occurrence of the entire tether being deployed during long transits. Once the entire tether is deployed, the low tension state at the surface can no longer be maintained, and the tether disturbance on the

ROV rises quickly. Conventional operations do not track the ROV position, so the ship pilot's best indicator of ROV position is the direction which the tether is leaving the vessel. Conventional operating practice is to drive the ship in the direction of the tether tangent, such that the near surface portion of the tether is vertical.

In the simulation studies of conventional tether management, the winch is used to maintain a constant low (20N) tension. The ship is driven only to maintain a near vertical orientation of the tether near the surface. This currently accepted practice does not rely on ROV position tracking, but as shown in the following subsections, produces large tether disturbances during long manoeuvres.

2.2.1 Conventional Tether Management during Transect Manoeuvres

A transect manoeuvre where the ROV waits at the starting position for 10s and then proceeds to the next waypoint 600m ahead at 0.2m/s is simulated in this subsection. The tether profiles, deployed tether scope, and tether disturbance occurring during the manoeuvre are shown in Figure 2-1.

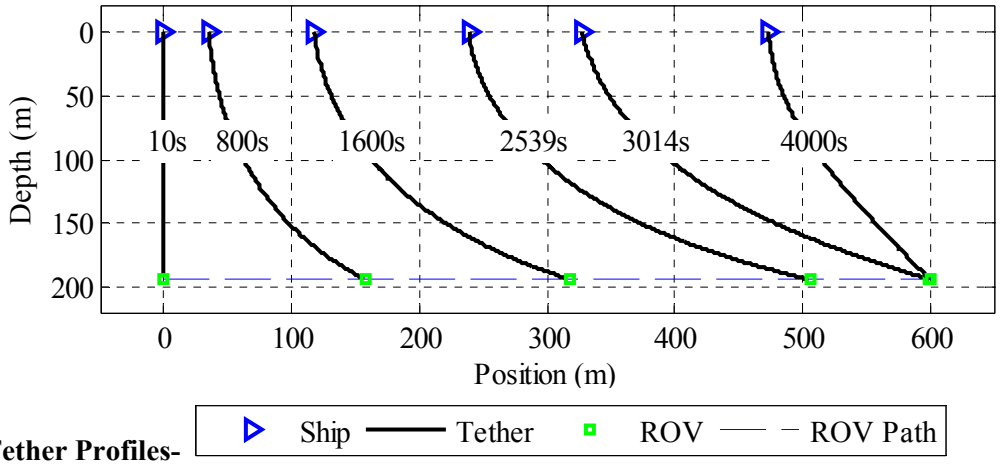

a) Tether Profiles-

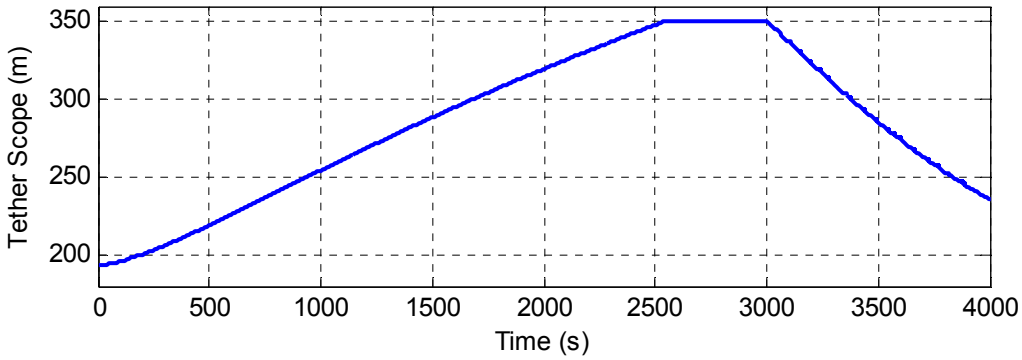

b) Tether Scope

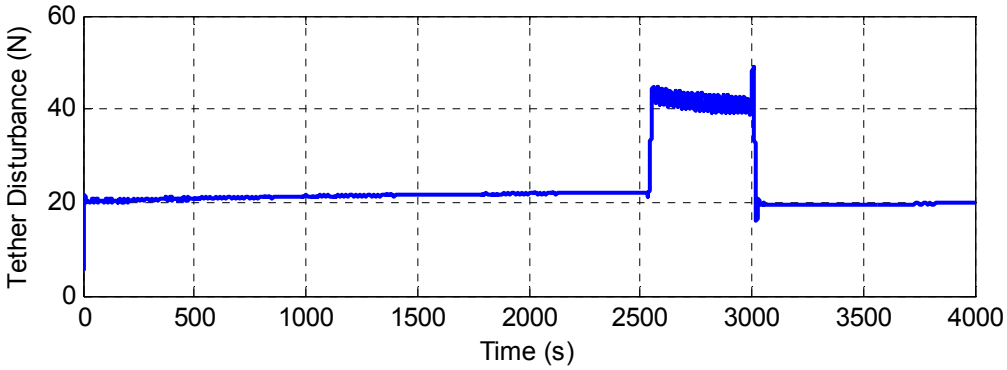

c) Tether Disturbance

Figure 2-1. Conventional Transect. The tether tension at the surface is regulated at 20N and the ship drives in the direction the tether is entering the water. 10s: The ROV starts from rest. 2539s: The tether length limit is reached. 3014s: The ROV stops at the waypoint. 4000s: The ship approaches overhead of the ROV and tether is retrieved.

Without disturbance, the ROV should reach the waypoint 3010s into the manoeuvre. However, the ROV leads the ship by such a distance that all 350m of the tether gets deployed 2539s into the manoeuvre, at which point the low tension state at the ship

cannot be maintained and the tether tension rises throughout the system. The tether disturbance increases to 43N, making it difficult for the pilot to keep a steady course.

2.2.2 Conventional Tether Management during Transit Manoeuvres

A manoeuvre where the ROV waits at the starting position for 10s before proceeding to the next waypoint 600m ahead is again simulated, but this time the pilot is requested to transit the ROV as fast as possible. Figure 2-2(a) shows the ROV, ship and tether motions that occur following the conventional tether management methodology. As the ROV surges forward, the tether is paid out as shown in Figure 2-2(b). Initially the tether tends to trail the ROV, but at 191s the tether length limit is reached and the ROV begins to draw the tether straight. At this point, tension regulation is impossible and the disturbance on the ROV rises dramatically as shown in Figure 2-2(c). The increased tether disturbance slows down the ROV. At 694s, the ROV is pulled off depth because the vertical thruster is saturated and the ROV controller reduces forward thrust to maintain depth. At the end of the manoeuvre, the ship approaches the ROV and retrieves the excess tether.

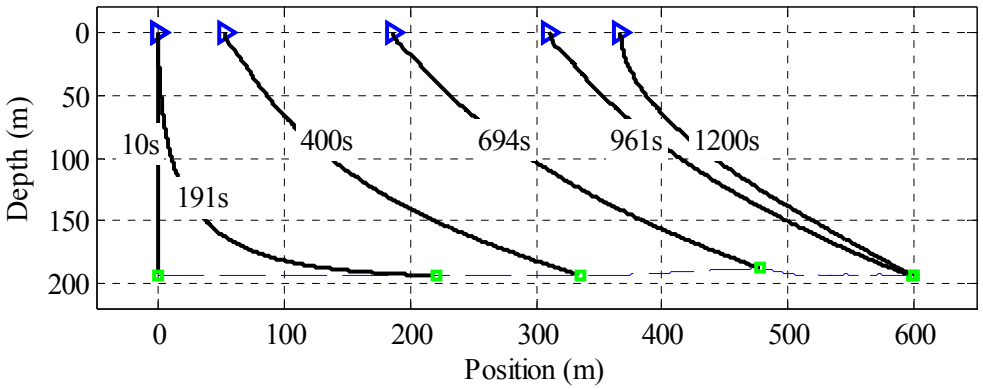

a) Tether Profiles -

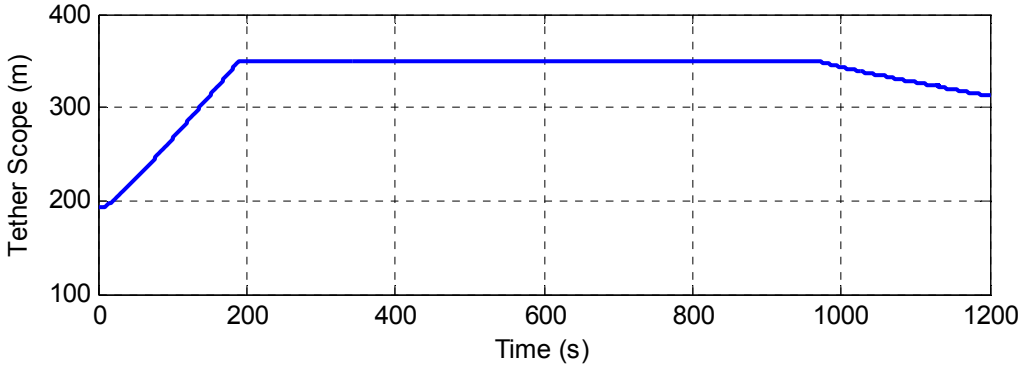

b) Tether Scope

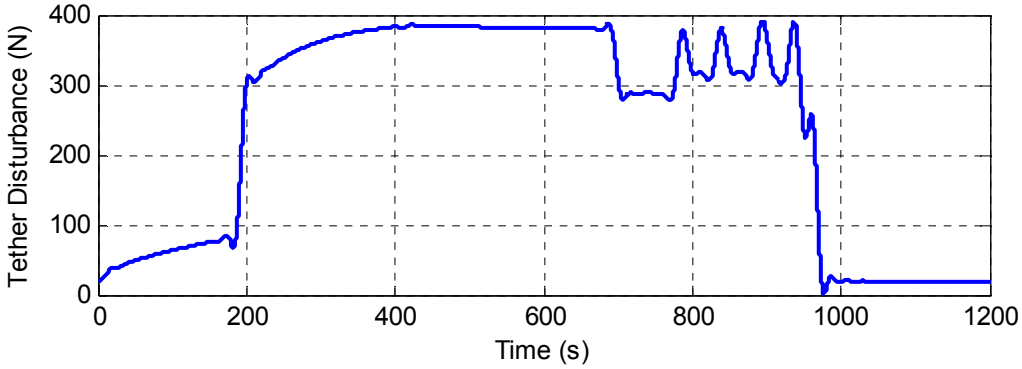

c) Tether Disturbance

Figure 2-2. Conventional Transit. The tether tension at the surface is regulated at 20N and the ship drives in the direction the tether is entering the water. 10s: The ROV starts from rest. 191s: The tether length limit is reached. 694s: The ROV vertical thruster is saturated; surge thrust is reduced to maintain depth. 961s: The ROV stops at the waypoint. 1200s: The ship approaches overhead of the ROV and tether is retrieved.

2.3 Analysis of the Tether Disturbance

In this section, investigative simulations and empirical models are utilized to develop more advanced tether management schemes with reduced tether disturbance. Ship position and tether scope are the two control variables that can be optimized to reduce tether disturbance.

So long as the ship to ROV distance is less than the deployed tether scope, hydrodynamic drag on the tether is the primary cause of tether disturbance. The tether is streamlined along its tangent, so normal drag which results from motion of the tether relative to the surrounding water normal to the tether tangent is often the only significant forcing. Deploying tether into the water to lengthen the scope reduces the tether disturbance caused by normal drag, but increases the likelihood of snagging the tether on the seafloor and reduces responsiveness to ROV direction changes. Also, control activity must comply with limits on ship response and tether length.

2.3.1 Tether Disturbance during Transect Manoeuvres

In this subsection, the ship position which minimizes tether disturbance during transect manoeuvres is sought by simulating the tether disturbance produced over the range of possible distances by which the ship could lead the ROV. The full 350m tether length is used since shorter tethers were found to produce more disturbances through increased tether tension. The configurations in which the ship leads or lags the ROV by more than 287m correspond to a ship to ROV slant ranges exceeding 350m, and would pull the tether tight and create immense tether disturbance. The tether disturbances for the feasible range of ship leads are mapped in Figure 2-3 and show that steady-state transects

of 0.2m/s can be maintained with a tether disturbance smaller than 10% of the ROV thrust capacity.

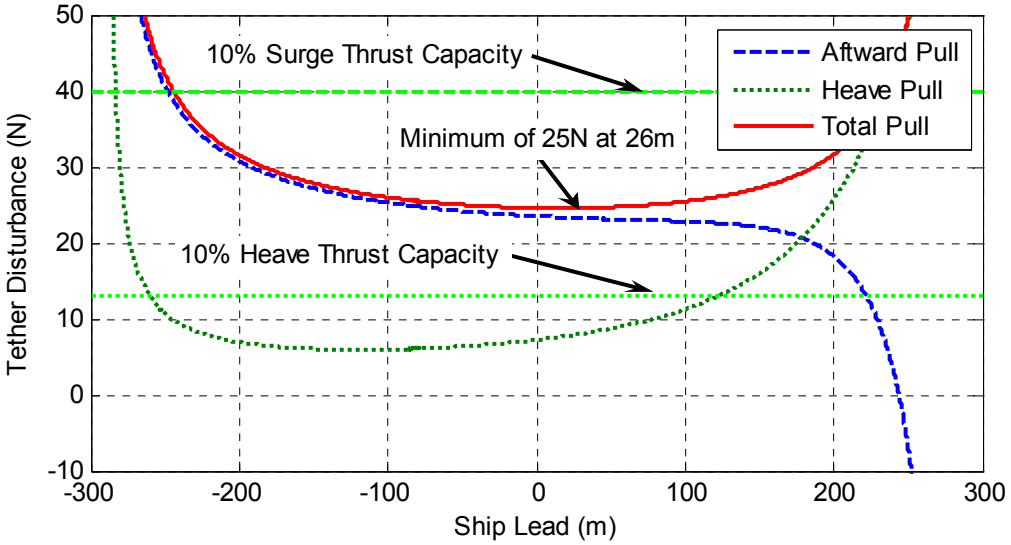

Figure 2-3. Tether Disturbance Mapped over Ship Lead for a 0.2m/s Transect.

As shown in Figure 2-3, the aftward pull due to tether disturbance decreases with increasing ship lead. However, the vertical pull due to tether disturbance increases with increasing ship lead.

The magnitude of the tether disturbance can be minimized to less than 25N if the ship leads the ROV by 26m. The next subsection extends this result to high speed transits.

2.3.2 Tether Disturbance during Transit Manoeuvres

The optimal ship lead derived in the previous subsection for transects can be extended to high speed transits. Apart from a small amount of axial stretch, steady-state tether profiles remain the same, regardless of transit speed. However, hydrodynamic drag increases quadratically with transit speed. The tether disturbance for a 1m/s transit speed (five times faster than the transect) is nearly twenty-five times greater than that of a

transect. Figure 2-4 shows the steady-state tether disturbance as a function of ship position for a 1m/s transit.

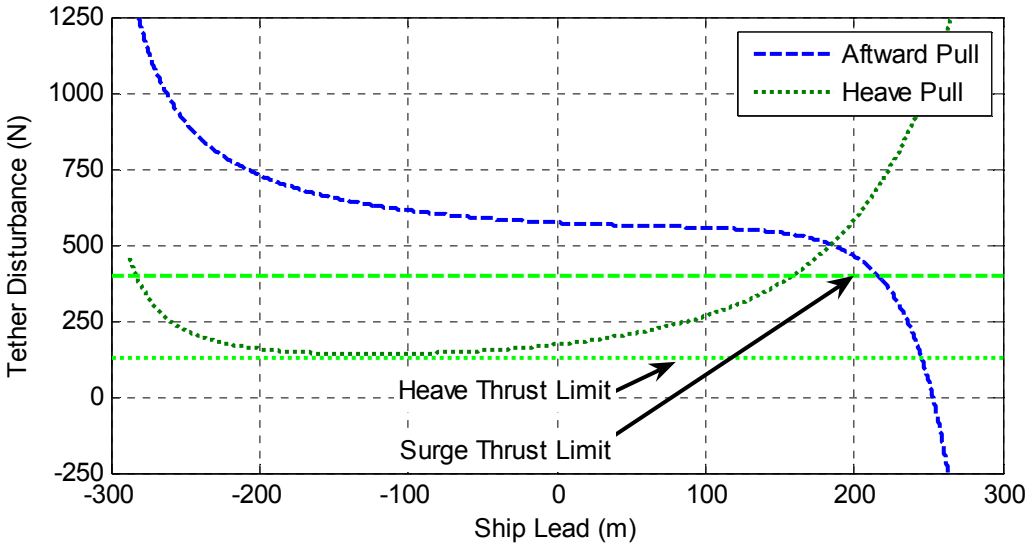

Figure 2-4. Tether Disturbance Mapped over Ship Lead for a 1 m/s Transit. Notice the shape similarity and change of tether disturbance scale compared to Figure 2-3.

Since no ship configuration produces a tether disturbance with heave and surge components both less than the Falcon™ ROV's corresponding thrust capacities, 1m/s transits with the Falcon™ ROV's neutrally buoyant tether cannot be continuously sustained. Also, vehicle hydrodynamic drag increases with transit speed, so the thrust capacity that can be allocated to overcome tether disturbance is reduced in the surge direction. Table 2-2 lists the tether and the hydrodynamic drag forces imparted on the ROV during a transect and several transit speeds.

Steady-state Speed	0.2 m/s	1.0 m/s	0.8 m/s	0.67 m/s
Tether Heave	8 N	188 N	120 N	84 N
Tether Surge	23 N	568 N	364 N	255 N
ROV Surge Drag	25 N	273 N	189 N	142 N
Total Surge Force	48 N	841 N	553 N	397 N

Table 2-2. Tether and Hydrodynamic Drag Forces Imparted on the ROV. Several steady-state surge speeds are considered with the ship leading the ROV by 26m and 350m of tether deployed. Tether disturbances at 0.2m/s and 1.0m/s surge speeds were measured with numerical simulation. Tether disturbances at 0.8m/s and 0.67m/s speeds were scaled based on the 1m/s tether disturbance. At 0.67m/s, the total surge force matches the thrust capacity, but the heave force is not at the thruster's 124N saturation limit.

The total surge force sustaining a 0.67m/s transit matches the surge thrust capacity, but the heave force is not at the heave thruster's 124N saturation limit. A small gain in the steady-state transit speed can be achieved by increasing the ship's lead on the ROV, thereby shifting tether disturbance in the surge direction to the heave direction where spare thrust capacity is available.

By increasing the ship's lead to 90m, the heave thruster is nearly saturated by the tether disturbance while the tether disturbance force in the surge direction is further reduced by 2%. This reduction in surge tether disturbance allows for a slightly faster steady transit speed. However, this speed increase is quite small, so all ship leads from 26m to 90m allow for nearly maximum steady-state transit speeds.

2.4 Advanced Tether Management

In this section, the optimal distances for the ship to lead the ROV derived in the previous section are applied to the demonstration manoeuvres introduced in Subsection 2.1.3. The conventional method of maintaining low tension in the tether as measured at the surface is retained.

2.4.1 Advanced Tether Management for Transect Manoeuvres

For the transect manoeuvre, the ship lead is selected to minimize the tether disturbance at the steady-state surge speed. As per Subsection 2.3.1, this ship lead is 26m for transects at 200m depth. For ROV surge speeds other than 0.2m/s, the optimal ship lead is still 26m, but the steady-state tether disturbance will differ from the 25N predicted for transects due to the change in magnitude of hydrodynamic forcing on the tether.

The advanced tether management scheme is demonstrated with the transect manoeuvre simulated over 4000s duration, and the ROV controller is given the same instructions as in the manoeuvre demonstrating conventional tether management. The ROV position is assumed to be known, and the ship leads the ROV by 26m. The resulting time evolution of the tether profile, tether scope, and tether disturbance are presented in Figure 2-5. This transect does not cause the entire tether to be deployed and the tether disturbance is low throughout the manoeuvre.

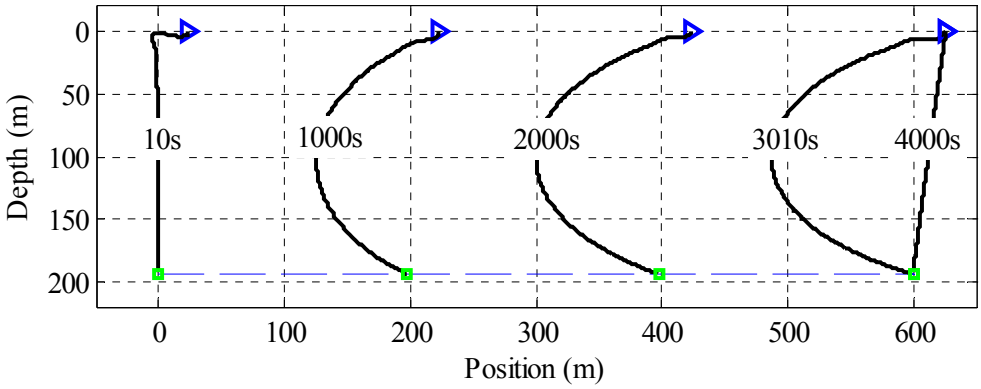

a) Tether profiles -

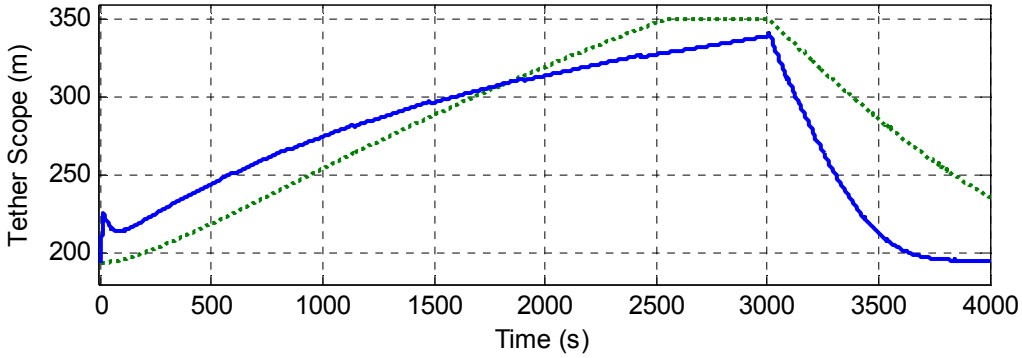

b) Tether scope with advanced (solid) and conventional (dotted) tether management

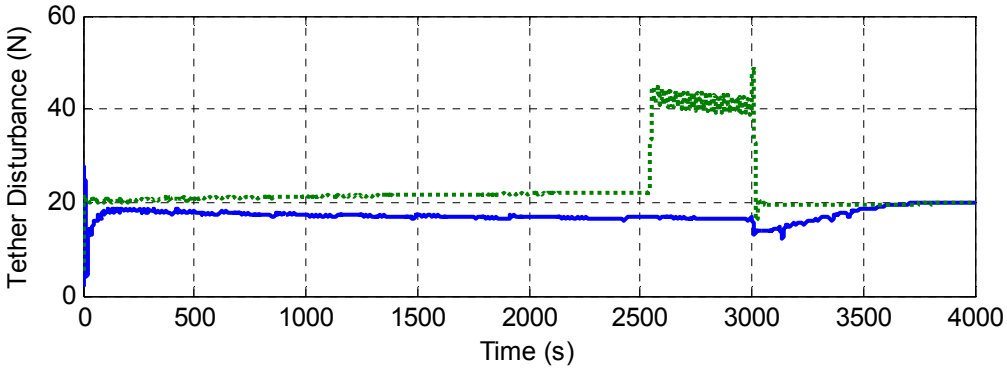

c) Tether disturbance with advanced (solid) and conventional (dotted) tether management

Figure 2-5. Transect with Advanced Tether Management. The tether tension at the surface is regulated at 20N and the ship leads the ROV by 26m. 10s: The ROV starts from rest. 3010s: The ROV stops at the waypoint. 4000s: The ship approaches overhead of the ROV position and tether is retrieved.

2.4.2 Advanced Tether Management for Transit Manoeuvres

For the transit manoeuvre, the ship is set to lead the ROV by 90m in an attempt to maximize surge speed. This ship lead was derived in Subsection 2.3.2 to distribute the tether disturbance in proportions that use the full thrust capacity of both the surge and sway thrusters at the maximum sustainable transit speed. Figure 2-6 shows the resulting time evolution of the tether profile, the tether scope, and the tether disturbance.

A transit with this advanced tether management scheme causes all 350m of tether to be deployed sooner than the conventional method because the ship starts the manoeuvre by driving ahead of the ROV. However, this configuration reduces the sustained tether disturbance to less than 280N, allowing the ROV to reach its destination in only 728s - 233s faster than when using the conventional tether management method.

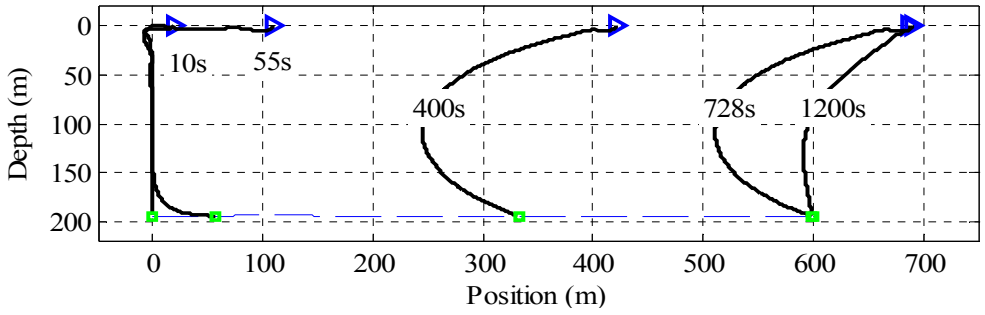

a) Tether profiles -

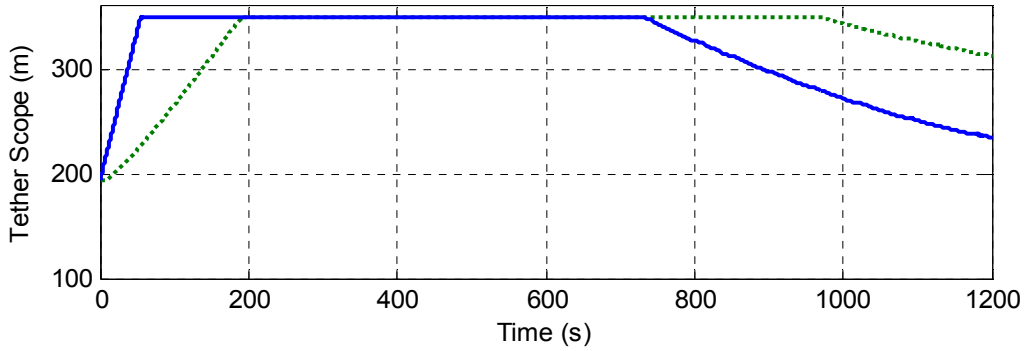

b) Tether scope with advanced (solid) and conventional (dotted) tether management

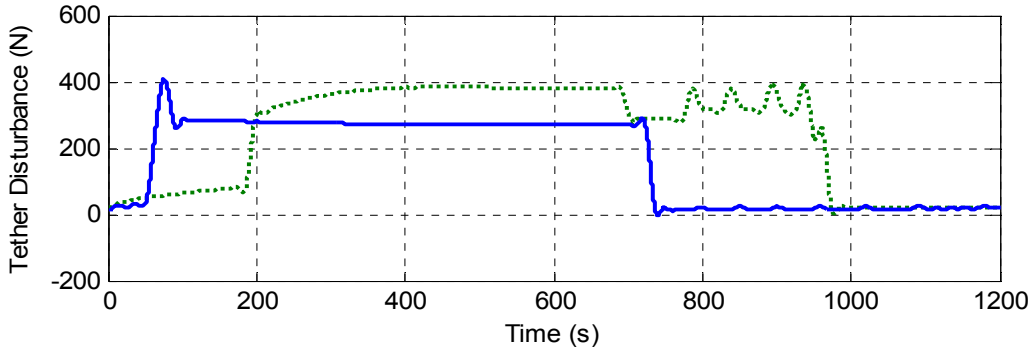

c) Tether disturbance with advanced (solid) and conventional (dotted) tether management

Figure 2-6. Transit with Advanced Tether Management. The tether tension at the surface is regulated at 20N and the ship leads the ROV by 90m. 10s: The ROV starts from rest. 55s: The tether length limit is reached 728s: The ROV stops at the waypoint. 1200s: The ship approaches overhead the ROV and tether is retrieved.

2.5 Depressor Effects

Further tether disturbance reductions and corresponding transit speed increases can be achieved with the use of a depressor mass. Adding a clump weight depressor to the tether a short distance away from the ROV ensures that the tether hangs almost vertically

from the ship, and allows ship motion to be used to position the depressor near the ROV. If the depressor is positioned correctly, the ROV is subjected only to the tether disturbance created by the hydrodynamic drag on the tether between the depressor and ROV. A tether management scheme was developed and presented by Zand et al. in [21] for Falcon™ manoeuvres with a depressor mass attached to the otherwise neutrally buoyant tether. The governing equations of this tether management scheme are presented in Subsection 2.5.1. Subsection 2.5.2 presents the application of the depressor tether management scheme to the transit demonstration manoeuvre defined in Subsection 2.1.3.

2.5.1 Depressor Tether Management

A depressor with the properties listed in Table 2-3 is added to the Falcon™ ROV's otherwise neutrally buoyant tether. The depressor is attached to the tether with 50m scope to the ROV. This amount of scope was found [21] to remain slack even during sudden ROV stopping manoeuvres.

Parameter	Value
Diameter	0.40 m
Mass	260 kg
Added Mass	17 kg
Scope to ROV	50 m

Table 2-3. Depressor Properties

Ship motion is scheduled to regulate the depressor's horizontal offset from the ROV, denoted Δ_x. Winch actuation regulates the depressor's vertical offset from the ROV, denoted Δ_z. In [21], desired offsets are calculated which mitigate tether disturbance on the ROV during transits and ensure the depressor does not collide with the ROV during operation. The shortest distances in which the depressor could be stopped using ship

motion were derived as a function of transit speed, u. In order to allow depressor overshoot to occur without tightening the tether leading to the ROV, the desired depressor horizontal offset was selected to be half of these stopping distances:

$$\Delta_x^* = -14.5|u|u - 2.25u \tag{2.1}$$

The superscript $(\cdot)^*$ denotes desired value. To avoid collision of the depressor with the ROV, the depressor depth was set as high as possible while allocating only 1% of heave thrust capacity to offset the vertical tether disturbance. The desired depressor depth offset is a function of the depressor's horizontal offset:

$$\Delta_Z^* = 0.0002|\Delta_X|^3 - 0.029|\Delta_X|^2 + 1.65|\Delta_X| - 31 \tag{2.2}$$

The water pulley effect [20] limits the horizontal acceleration of the depressor achievable through ship motion. Since abrupt changes to depressor position are not possible with ship and winch activity, the desired depressor offsets are low pass filtered according to:

$$\begin{aligned} \dot{\tilde{\Delta}}_X^* + 100 \cdot \tilde{\Delta}_X^* &= \Delta_X^* \\ \dot{\tilde{\Delta}}_Z^* + 10 \cdot \tilde{\Delta}_Z^* &= \Delta_Z^* \end{aligned} \tag{2.3}$$

The overhead tilde $(\tilde{\cdot})$ indicates a smoothed quantity and the overhead dot indicates a partial differential with respect to time. The time constants of the filters in Equation (2.3) were optimized through iterative simulation of the depressor system's response to control inputs.

Depressor depth is achieved by setting the winch payout rate, $\dot{s}$, as the sum of the error in depressor depth and the rate of increase of depressor vertical offset:

$$\dot{s} = \left(\tilde{\Delta}_z^* - \Delta_z\right) + \left(w - w_{DPR}\right) \tag{2.4}$$

In Equation (2.4), w denotes the ROV heave velocity and w_{DPR} denotes the depressor heave velocity.

Depressor horizontal positioning is achieved by determining a desired ship speed and enacting that ship speed with ship propulsion. The desired ship speed is a linear combination of ROV speed, the depressor horizontal position error, and the rate of increase of depressor horizontal offset:

$$u_S = u + 0.05\left(\tilde{\Delta}_X^* - \Delta_X\right) + 4.0\left(u - u_{DPR}\right) \tag{2.5}$$

The constant coefficients in Equation (2.5) were selected through iterative simulation to optimize depressor positioning response. Equations (2.1) through (2.5) govern the depressor tether management scheme presented by Zand et al. in [21].

2.5.2 Demonstration Manoeuvre with Depressor Tether Management

The depressor tether management scheme [21] was applied to the transit demonstration manoeuvre. Figure 2-7(a) shows the tether profiles at key times in the manoeuvre. During the first 10s of the manoeuvre, the ROV is stationary, and the ship hangs the depressor 31m above the ROV. As the ROV starts the transit and increases its velocity, the ship leads by over 150m to accelerate the depressor. Meanwhile, the winch releases tether to drop the depressor towards the ROV depth to streamline the tether between the depressor and the ROV. The ROV reaches the destination waypoint at 542s and the system settles to the stationary equilibrium position. Figure 2-7(b) compares the tether scope deployed using the depressor tether management scheme to the tether scope deployed using the tether management schemes with neutrally buoyant tethers. The depressor tether management scheme uses less tether scope and does not reach the tether length limit. Figure 2-7(c) shows the tether disturbance generated using the depressor

tether management scheme is significantly less than the tether disturbances generated by the tether management schemes with neutrally buoyant tethers.

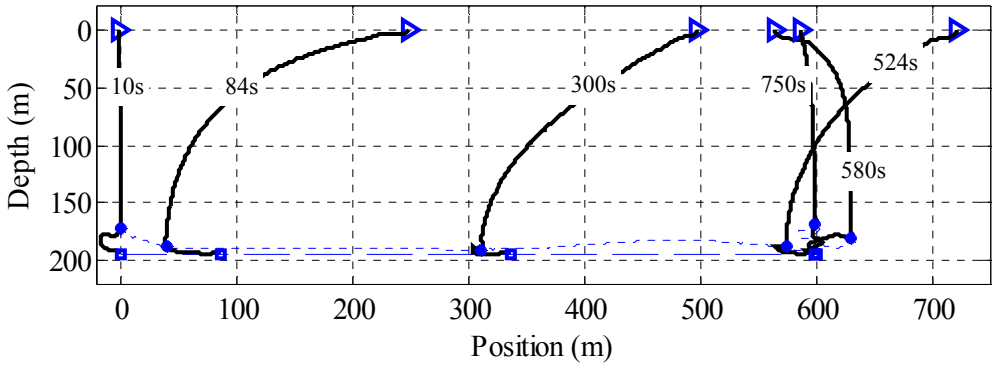

a) Tether profiles

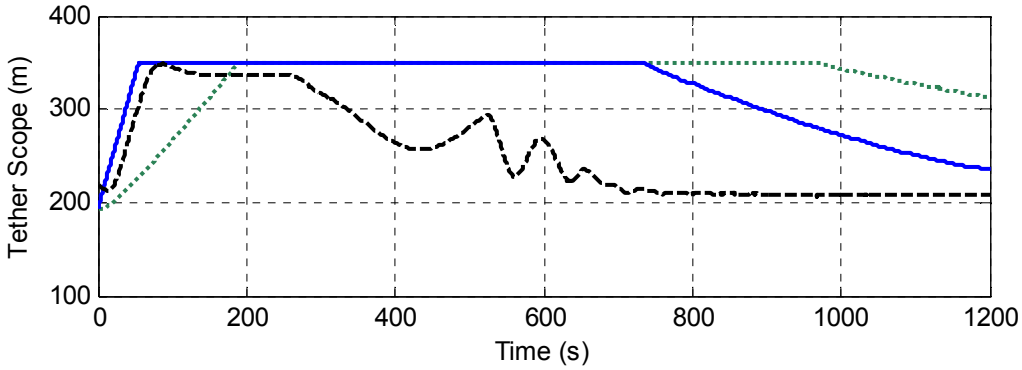

b) Tether scope with advanced (solid), conventional (dotted) and depressor (dashed) tether management

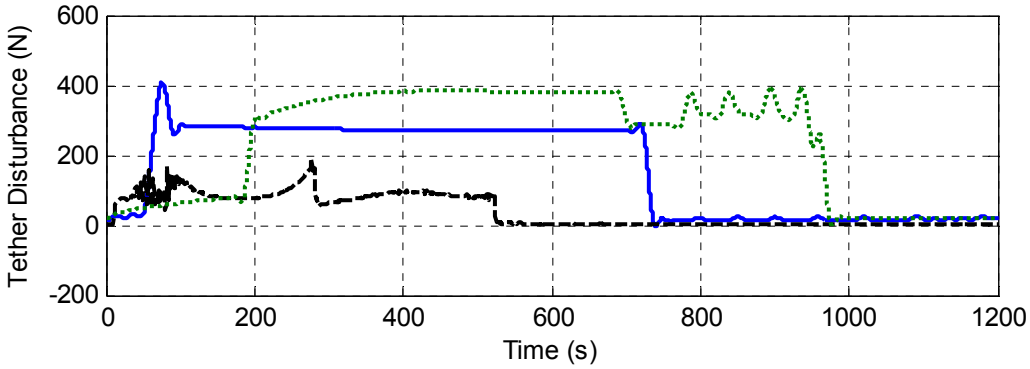

c) Tether disturbance with advanced (solid), conventional (dotted), and depressor (dashed) tether management

Figure 2-7. Transit with Depressor. Ship and winch activity was regulated according to the depressor tether management scheme summarized in Subsection 2.5.1. The demonstration manoeuvre proceeds as follows: 10s: The ROV starts from rest; the ship surges ahead, deploying tether in its wake. 84s: Depressor speed reaches ROV speed and tether retrieval begins. 524s: The ROV stops at the waypoint. 580s: The depressor comes to a stop. 750s: The system regains stationary equilibrium.

The tether disturbance reduction realized with the depressor tether management scheme allows the ROV to sustain a transit speed in excess of 1m/s.

2.6 Tether Management Remarks

Excessive tether disturbance often limits the ROV manoeuvre speed or length. The tether disturbance can be reduced by releasing more tether from the ship, but tether disturbance increases quickly when the entire length of tether is deployed. Transects with low tether disturbance and transits at moderate speeds can be achieved by having the ship lead the ROV by prescribed amounts. The ROV surge speeds for long transits can be further increased with the use of a depressor.

Tether position regulation schemes based on ship and winch activity have been introduced for small inspection class ROVs. Slow response of the tether in the normal direction requires the ship commands to react quickly in order to keep up with ROV course changes. The advanced tether management schemes and the depressor tether management scheme require tracking the ROV position. The depressor tether management scheme also requires tracking the ROV velocity. The accomplishment of this requirement is discussed in the following chapters, which present the implementation and testing of a position and velocity tracking system.

Chapter 3. Navigation Estimation

Towards the implementation of advanced tether management schemes, efficient seafloor surveys, and successful object recoveries discussed in previous chapters, the position and velocity of the ROV must be accurately tracked at a high update rate. As discussed in Section 1.3 all position, velocity and inertial motion sensors used on underwater vehicles have performance limitations. Acoustic positioning has high measurement noise and slow update rates; ROV positions dead reckoned from DVL body-fixed velocity measurements accumulate bias and truncation errors. Complementary filtering of the ROV position, velocity, attitude, and rotation rate measurements provided by an SBL acoustic positioning system, a DVL, a compass, and an IMU respectively, is anticipated to estimate the position of the ROV with the long term stability of acoustic positioning at the high update rate of dead reckoning.

This chapter describes the sensor suite, filtering algorithm, and dynamics model used in the ROV tracking solution. The sensor setup on the Falcon™ and the collection of measurement are described in Section 3.1. The principles of Kalman filtering are presented in Section 3.2, and are modified in Section 3.3 to produce an EKF which accounts for nonlinear ROV dynamics and asynchronous measurements. The ROV dynamics used to propagate the EKF estimate through time are introduced in Section 3.4.

3.1 Sensor Installation

ROV kinematic measurements are collected and processed to accomplish the objectives of this work. An SBL, a compass, a DVL, and an IMU are used in conjunction with the Falcon™ ROV's onboard compass and depth sensor. Instrumenting the Falcon™ requires enclosing the sensors in waterproof containers and routing the data stream to the surface computer. The compass and depth measurements standard for Seaeye vehicles are collected by monitoring the Falcon™ ROV's existing telemetry network, as described in detail in Subsection 3.1.3. The ROV mounted acoustic transducer, which is part of the SBL system, is self contained, battery powered, and communicates acoustically with the reference transducers at the surface. A waterproof housing was designed and built for the DVL and IMU. A Sparton™ compass manufactured by Sparton Corp. was also installed in the housing. Communication between these sensors and the surface computer is accomplished using additional digital communication channels available through a fibre-optic tether purchased for the project.

3.1.1 Subsea Sensor Pod

The subsea sensor pod shown in Figure 3-1 was designed for ease of machining. It consists of an aluminium casing with two end caps. The bottom cap is bored to hold the DVL transducer head. The aluminum housing is anodized to prevent corrosion. The caps are held together with two stainless steel threaded rods which also guard the DVL transducer. When submerged, water pressure helps to hold the assembled pod together. A single radial o-ring seals each cap-casing interface.

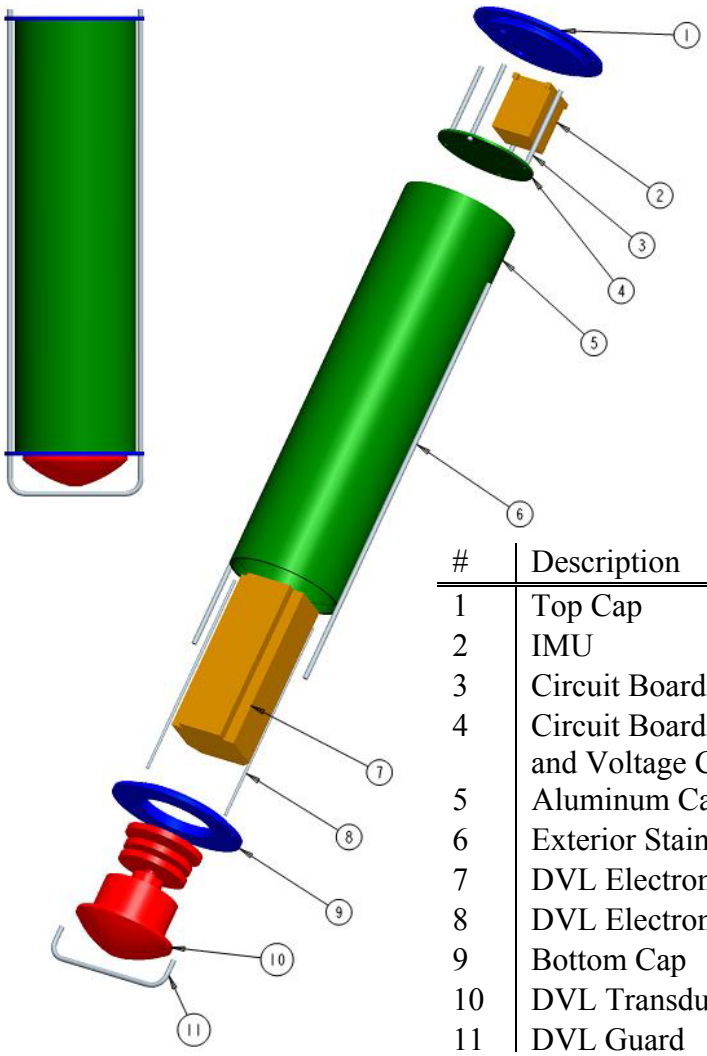

#	Description
1	Top Cap
2	IMU
3	Circuit Board Standoffs
4	Circuit Board – Base for Sparton Compass and Voltage Converters
5	Aluminum Casing
6	Exterior Stainless Steel Rods
7	DVL Electronics
8	DVL Electronics Standoffs
9	Bottom Cap
10	DVL Transducer Head
11	DVL Guard

(a) Assembly Drawing of the Sensor Pod

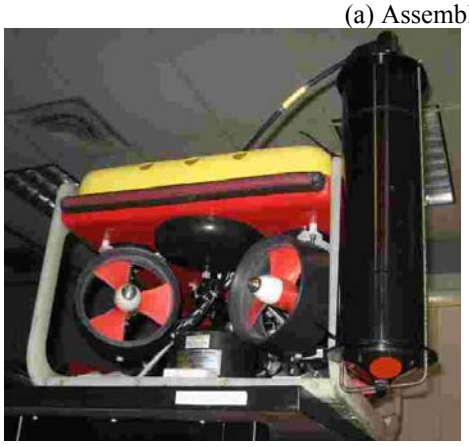

(b) Rear View

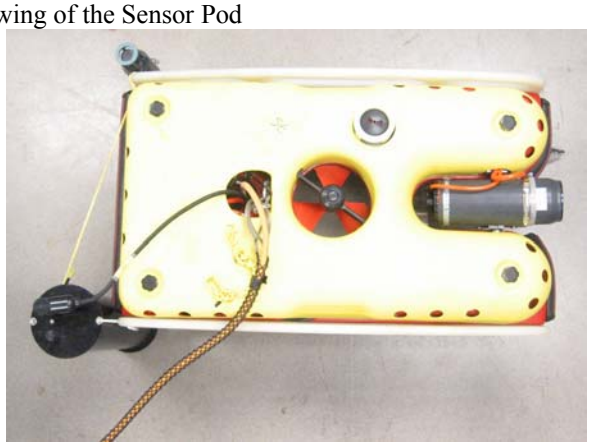

(c) Plan View

Figure 3-1. Sensor Pod. The sensor pod contains the Explorer™ DVL, Sparton™ compass, and MMQ50™ IMU. Also shown is the SBL target transducer on the port rear corner.

During deployment, the pod's impact on ROV buoyancy is reduced by ballasting the pod for neutral buoyancy. With the DVL, compass, and IMU installed, the pod exhibits slightly positive buoyancy. A 600g lead block attached to one of the stainless steel rods makes the pod neutrally buoyant in fresh water. An additional 230g lead block is attached to one of the stainless steel rods for saltwater operation. As more sensors are added to the pod, the ballasting weights can be reduced to preserve neutral buoyancy.

Radial o-rings were selected for ease of assembly. Radial o-rings are easier to install than face o-rings, as they do not fall out of their groove when disassembled. A vent plug was installed, but found to be unnecessary due to the open (compressible) volume in the pod being much larger than the volume displaced during cap installation.

A Subconn® underwater cable with twelve wires penetrates the top cap and links with a wet-mateable connector on the Falcon™ junction box. Two wires supply the sensor pod with 48V DC power, and nine others connect the three RS232 channels to the fibre-optic multiplexer in the ROV junction box. Two DC to DC voltage converters supply the +12V and –12V power requirements of the DVL, IMU, and Sparton™ Compass.

3.1.2 Instrument Placement

The standard Falcon™ instruments are located within the ROV's open frame. A cowling mounted above the syntactic foam protects the onboard cables and instruments. The imaging sonar transducer protrudes through the top of the cowling to provide a clear path for the sonar signals, whereas the rest of the unit is protected within the cowling. The water column below the top-center mounted vertical thruster is kept clear to avoid hindering the thruster wash. Protecting instrumentation from exterior impacts and

maintaining sleekness to avoid subsea entanglement are major design considerations for selecting locations for additional instrumentation.

Another important consideration during instrument placement is the function of the instrument. The compass needs to be placed far away from transient magnetic field sources, such as the electric thrusters. The DVL transducers require a clear view of the seafloor. The SBL target transducer must have unobstructed paths to the surface mounted reference stations.

Instrument placement is important for the dynamics model as well. The ROV coordinates (shown in Figure 3-2) were defined with an origin at the vehicle's center of mass and the x, y, and z coordinates representing surge, sway, and heave directions respectively. Offsetting the SBL and DVL from the origin of the ROV coordinate frame leads to differences between the sensor measurements and the corresponding state measurements at the ROV mass centre. Since the DVL cannot be placed at the origin of the ROV coordinate frame, the ROV rotation rates must be tracked and combined with the DVL measurements to calculate the ROV velocity. The tether's attachment point to the ROV dictates where the disturbance force is applied. Since this point is not at the origin of the ROV, a torque is induced by the tether disturbance. Table 3-1 lists the positions of the important instruments in ROV coordinates.

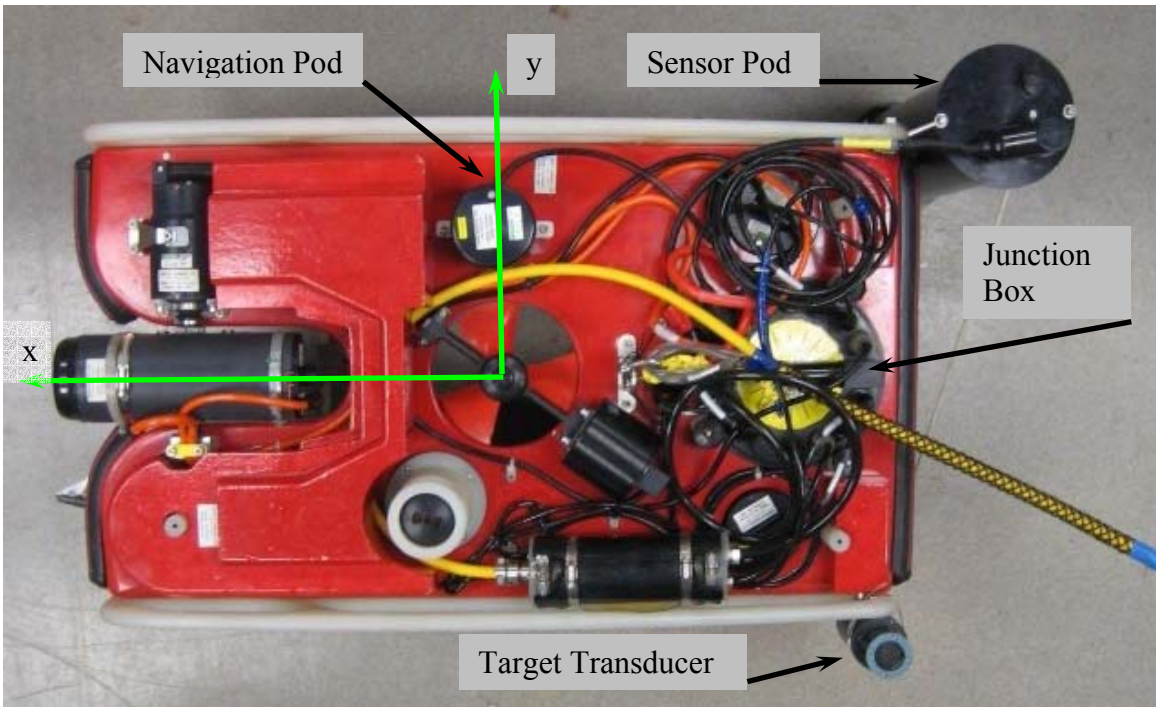

a) Falcon™ Top View

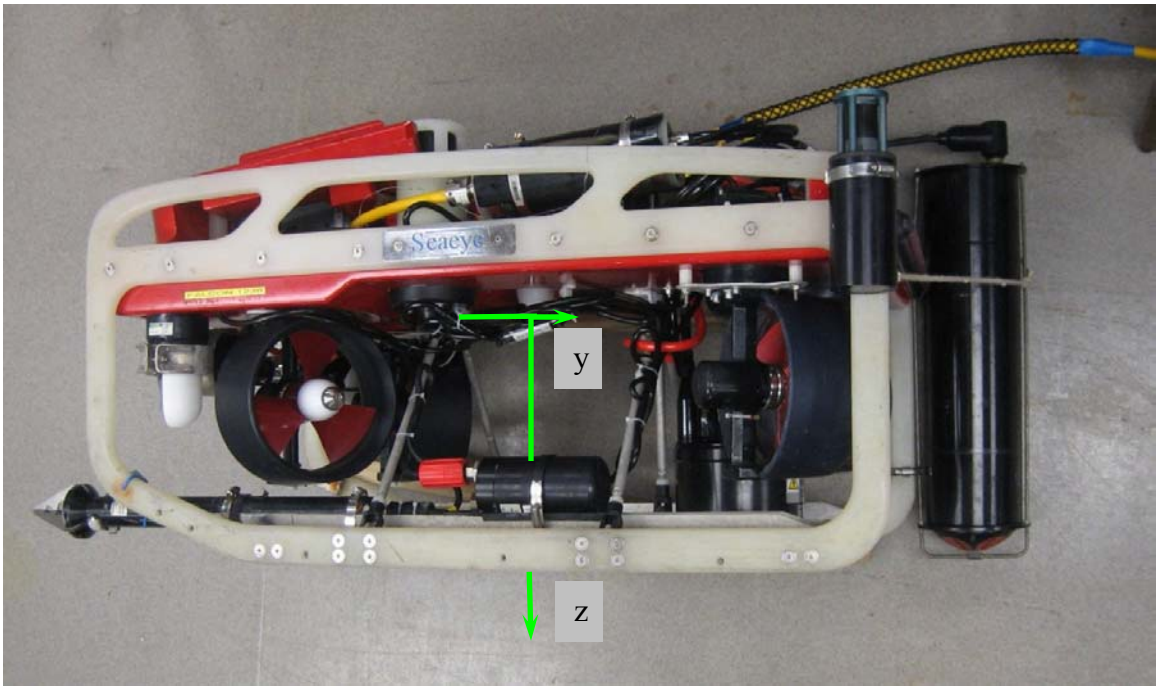

b) Falcon™ Side View

Figure 3-2. Falcon™ Instrument Layout. The ROV coordinate frame's origin is located at the mass centre, just below the vertical thruster. The SBL target transducer and the sensor pod containing a DVL, a compass, and an IMU are fastened to the rear corners of the vehicle. The navigation pod containing a compass, a depth sensor, and a gyroscope is located under the vehicle cowling (removed) to starboard of the vertical thruster.

Instrument	Parameter	Value (m)
DVL	x_{DVL}	-0.59m
	y_{DVL}	0.30m
	z_{DVL}	0.35m
SBL Target Transducer	x_{TARGET}	-0.45m
	y_{TARGET}	-0.34m
	z_{TARGET}	-0.15m
Tether Shackle	$x_{SHACKLE}$	0.14m
	$y_{SHACKLE}$	0.00m
	$z_{SHACKLE}$	-0.22m
IMU	x_{IMU}	-0.58m
	y_{IMU}	0.30m
	z_{IMU}	-0.17m
Sparton™ Compass	$x_{SPARTON}$	-0.59m
	$y_{SPARTON}$	0.30m
	$z_{SPARTON}$	-0.07m
Seaeye Navigation Pod	x_{NAVPOD}	0.00m
	y_{NAVPOD}	0.18m
	z_{NAVPOD}	-0.16m

Table 3-1. Instrument Locations. The values are measured in ROV coordinates.

3.1.3 Sensor Telemetry

Measurements are transmitted from the instruments onboard the ROV to the navigation laptop through three paths: (1) the standard Falcon™ sensors in the navigation pod send their measurements through the tether using the Falcon™ ROV's telemetry channel; (2) the instruments in the sensor pod have dedicated RS232 channels also sent through the tether; (3) the SBL acoustic position tracking system is independent of the Falcon™ hardware and sends data through the water using acoustic communication. Each measurement stream is collected by its respective monitoring thread within the Kalman software. These monitoring threads parse the data into measurements, apply scaling and alignment, and add each measurement to the measurement buffer for subsequent

processing by the EKF algorithm. Figure 3-3 shows a schematic of the measurement collection process.

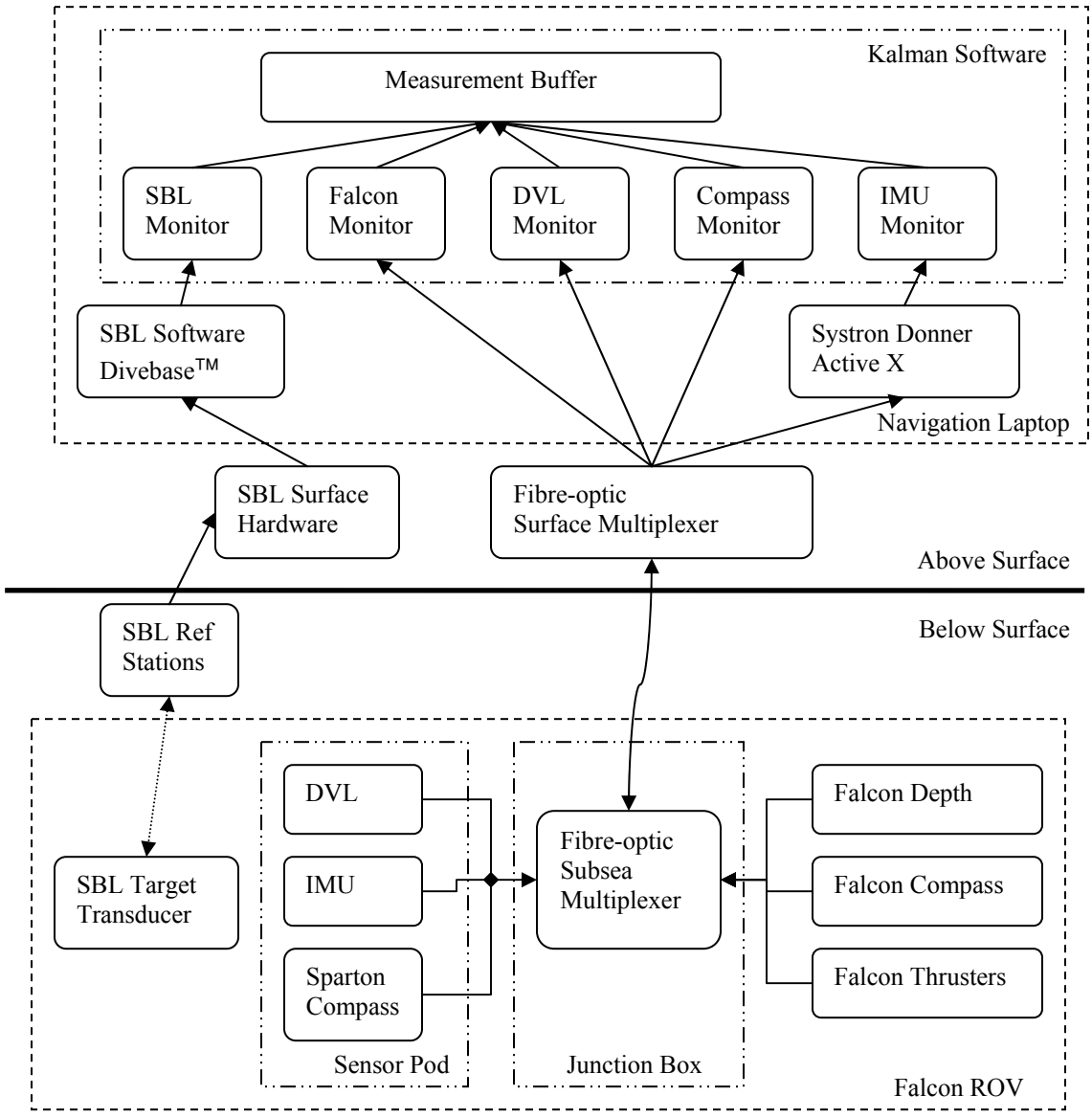

Figure 3-3. The Sensor Data Flow used by the EKF. The Falcon™ sensor and thruster commands are read into the navigation laptop through the RS485 telemetry network sent through the tether. The sensor pod instruments are linked to the navigation laptop through the tether on individual RS232 channels. The SBL target transducer communicates with the SBL reference stations with in-water acoustic signals, and its signal is processed by the SBL equipment before being presented to the navigation laptop. The Kalman software processes the signals and stores them in a measurement buffer.

The standard Falcon™ sensors, specifically the compass and depth sensor, are located in the Seaeye navigation pod mounted beneath the top cowling, on the starboard side of the vehicle (see Figure 3-2(a)). Each sensor connects to the Falcon™ telemetry via its dedicated RS485 node within the navigation pod. The RS485 network connects through the Falcon™ junction box, where it is distributed to the onboard actuators including thrusters, lights, manipulator, and others. This network is also connected to the surface hardware by multiplexing it along with a second RS485 channel used for the sonar, four RS232 channels used with the instruments in the sensor pod, and the video channels. The multiplexed channels are sent up the tether through a fibre-optic line and separated into their original channels inside the Seaeye cabin junction box. The Falcon™ telemetry, back in its RS485 form, connects to the master node within the surface station. This node sends, requests, and receives data based on the ROV pilot's control inputs. Within the cabin junction box, the Falcon™ RS485 telemetry is yoked and the second line is converted to a RS232 channel with only the receive line, allowing the Falcon™ telemetry to be read but not changed. This channel is connected to the navigation laptop, where it is read with the Falcon™ Monitor. The Falcon™ Monitor is a thread within the navigation software which reads every character of the Falcon™ telemetry, parses the compass and depth measurements, converts the thruster commands into thruster forces, and discards the rest. The measurements and thruster commands are time-stamped and stored in the measurement buffer.

The sensor pod instruments, namely the Sparton™ compass, MMQ50™ IMU, and Explorer™ DVL, output measurements on individual RS232 channels. These signals are

transmitted to the Falcon™ junction box through a twelve wire Subconn® cable with a wet-mateable connector. The channels are multiplexed along side the Falcon™ RS485 telemetry within the junction box, are transmitted through the tether via a fibre-optic line, and then are demultiplexed at the surface. Once back into their individual RS232 channels, the three sensor channels are connected to the navigation laptop. Each sensor channel is monitored by a dedicated thread within the Kalman software. The Compass Monitor removes measurement bias caused by misalignment between the Sparton™ compass coordinates and the ROV coordinates and provides a final heading result between 0deg and 360deg. The DVL Monitor aligns the velocity measurements to the ROV coordinates, removes bad measurements caused by loss of bottom lock, and converts the measurement units to m/s. Systron Donner's ActiveX controller converts raw MMQ50™ IMU data to calibrated measurements in m/s^2 and deg/s and provides them to the IMU Monitor. The IMU Monitor aligns the gyroscope measurements to the ROV axes, and submits the corrected spatial rotational velocity to the measurement buffer. The IMU's acceleration measurements are not used.

Acoustic position tracking is done using Desert Star System's PILOT™ SBL system. This system operates independently of the Falcon™ ROV equipment and bypasses the tether by using acoustic communications between the target transducer on the ROV and the reference stations. The range between the target transducer and each reference station is measured by tracking the time it takes an acoustic signal to travel between the two transducers. The measurement process starts with a reference station transmitting an acoustic pulse into the water. When this signal is received by the target transducer, the target transducer replies with a similarly identifiable signal, and also includes a signal

indicating the depth of the target transducer measured by a pressure sensor. The reference stations not only transmit the interrogation signal, but also listen for replies from the target transducer. The PILOT™ SBL's STM-10™ surface station analyzes the acoustic signals, already converted to a voltage by each reference transducer. The surface station connects to the navigation laptop with a serial connection and interfaces with Desert Star System's Divebase™ acoustic positioning software. The reference station locations are entered into Divebase™ and used to calculate the target transducer's position. Divebase™ exports the range measurements and if available, a position measurement, to a communications socket. This socket is monitored by the SBL Monitor, which ensures that the range measurements are valid and enters them in the measurement buffer along with a time-stamp and the location of the associated reference station.

The measurement buffer stores the measurements until the filtering algorithm uses them. All measurements in the buffer are time-stamped and indexed according to the instrument they were made by.

3.2 Kalman Filter Fundamentals

Kalman Filters [12] are widely used complementary filters that draw on a process model and assistive sensor measurements to propagate a system state estimate through time. At each time-step, t_k, the vector of sensor measurements, z_k, and the predicted state estimate, $\hat{x}_k^-$, are combined through weights called the Kalman gains. These gains are based on the relative estimated uncertainties of the state estimate and of the measurements. The Kalman gains minimize the variance of the error of the state estimate subject to the following constraints [46]:

- Linear process model dynamics:

$$x_k = \Phi \cdot x_{k-1} + w_k \tag{3.1}$$

- Gaussian process model errors, *w*, with zero-mean and variance *Q*:

$$Q_k = E[w_k w_k^T] \tag{3.2}$$

- Gaussian measurement errors, *v*, with zero-mean and variance *R*:

$$\begin{aligned} z_k &= H \cdot x_k + v_k \\ R_k &= E[v_k v_k^T] \end{aligned} \tag{3.3}$$

- Measurement error independent of process error:

$$E[w_k v_k^T] = 0 \tag{3.4}$$

The notation used in the KF is as follows: x is the KF state, Φ is the KF process state transition matrix, w is the KF process error, Q is the KF process error covariance matrix, z is the KF measurement vector, H is the KF measurement matrix, v is the measurement error, R is the measurement error covariance matrix, a k subscript represents the value at the time t_k, an overhead hat (^) represents an estimated value, the superscript $(\cdot)^T$ represents transpose, and the superscripts $(\cdot)^-$ and $(\cdot)^+$ represent the value before and after the state estimate is corrected with measurements, respectively.

During each time-step t_k of the discrete KF, an initial state estimate is calculated by applying the state transition matrix, Φ, to the optimal estimate of the state made at the previous time-step:

$$\hat{x}_k^- = \Phi \cdot \hat{x}_{k-1}^+ \tag{3.5}$$

The state estimate error covariance matrix, denoted $\hat{P}_k^-$, is calculated by manipulating the error covariance estimate at the previous time-step, $\hat{P}_{k-1}^+$, to account for state changes and by adding the process uncertainty to the result:

$$\hat{P}_k^- = \Phi \hat{P}_{k-1}^+ \Phi^T + Q_k \tag{3.6}$$

The measurements received at the current time-step are listed in the measurement vector, z_k, and dictate the assembly of the measurement matrix H_k and the measurement covariance matrix R_k. The innovation vector, e_k, is the difference between the measurement values and the KF's expectations for the measured values.

$$e_k = z_k - H_k \hat{x}_k^- \tag{3.7}$$

The optimal Kalman gain, K_k, is calculated based on the measurements available, the uncertainty of those measurements, and the uncertainty of the initial state estimate:

$$K_k = \hat{P}_k^- H_k^T \left[H_k \hat{P}_k^- H_k^T + R_k \right]^{-1} \tag{3.8}$$

A refined estimate, $\hat{x}_k^+$, is then computed by adjusting the initial estimate with the measurement innovations:

$$\hat{x}_k^+ = \hat{x}_k^- + K_k e_k \tag{3.9}$$

The estimated error covariance of the initial state estimate is used to calculate the error covariance, $\hat{P}_k^+$, of the refined state estimate:

$$\hat{P}_k^+ = [I - K_k H_k] \hat{P}_k^- \tag{3.10}$$

The state estimate at the next step can then be calculated by repeating equations (3.5) through (3.10). Figure 3-4 shows the steps of the recursive KF process.

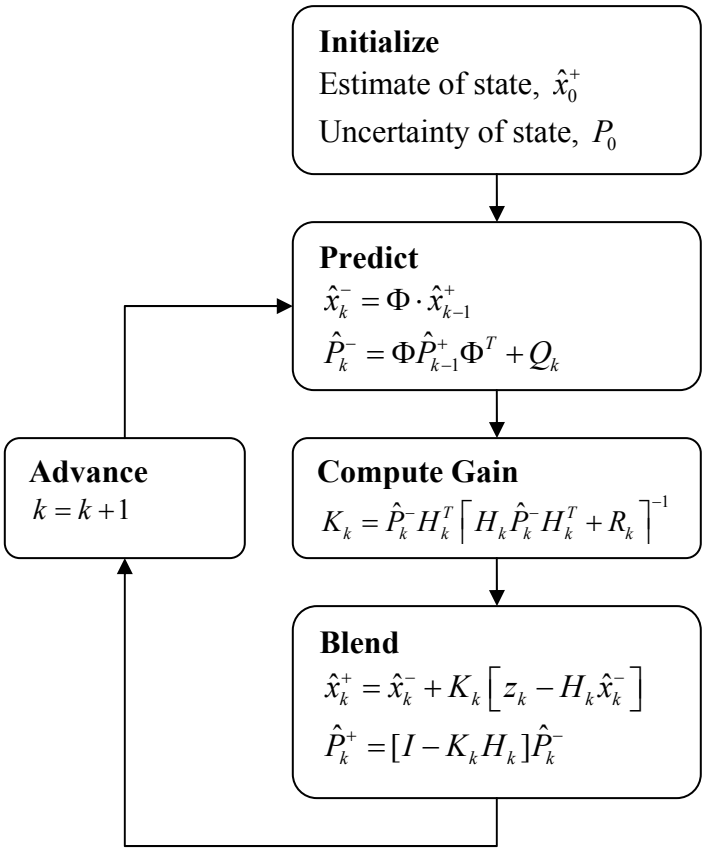

Figure 3-4. The Standard KF Process.

Both direct state and error state formulations of the KF are prevalent in practice. Direct state formulations, such as those presented in [25] and [37], and the one used in this work, employ state dynamics to propagate the state. Error state formulations propagate an estimate of the measurement error using a model of the measurement error in the KF. Error state formulations correct for measurement error by subtracting the estimated error from the measurement values [26, 29, 42]. Direct state formulations work best for applications using a wide range of measured quantities with sophisticated system models because they provide the framework to relate the measurements from the various sensors, and account for uncertainty in the relationships. Error state formulations are better suited

to model instrument behaviour, such as time varying gyroscope biases, because they provide the framework to model the progression of measurement error.

3.3 The Extended Kalman Filter

The basic KF works well for linear systems. Consider an acoustic tracking system being aided by DVL measurements and highly accurate orientation measurements. The orientation measurements could be used to transform the body-fixed DVL measurements into earth frame coordinates. A linear state transition matrix could then be formulated for the kinematics relating ROV position to ROV velocity and a KF could be used to find the optimal ROV position and velocity given the measurements provided. However, if accurate ROV orientation tracking is not available, a more accurate filter would include the ROV Euler angles as states and transform the DVL velocity to earth coordinates within the KF framework. Unfortunately, transforming the velocity to earth coordinates is a nonlinear calculation, and including it in the KF state transition matrix would violate the constraint defined by Equation (3.1).

The KF principles can be applied to filter non-linear systems by using an EKF, which linearizes the state dynamics and measurement functions about the state estimate at each time-step. The nonlinear state dynamics and measurement functions violate the Gaussian noise requirement for Kalman optimality, so the EKF estimate is not guaranteed to be the minimum error variance estimate. However, proper estimation of the process uncertainty ensures near optimality for smoothly varying systems. Alterations or approximations must also be made to account for asynchronous measurements and for measurement delays.

3.3.1 Linearization about the Current State Estimate

Applying the KF methodology to linearized state relationships produces an EKF [13]. An EKF uses the following state and measurement functions.

$$\begin{aligned} \dot{x} &= f(x,t) \\ \hat{z} &= h(x,t) \\ F_k &= \left.\frac{\partial f(x,t_k)}{\partial x}^T\right|_{x=\hat{x}_k^-} \\ H_k &= \left.\frac{\partial h(x,t_k)}{\partial x}^T\right|_{x=\hat{x}_k^-} \end{aligned} \tag{3.11}$$

In Equation (3.11), the system dynamics are embedded in the set of nonlinear functions denoted by *f*, which model the time rate of change of the state. The Jacobian of the dynamics of *f* is denoted by *F*. The measurements collected by an EKF can be nonlinear functions of the state, with the relationships modeled by the Kalman measurement functions $h(x)$. The EKF prediction equations become:

$$\begin{aligned} \hat{x}_k^- &= \hat{x}_{k-1}^+ + \int_{t_{k-1}}^{t_k} f(\hat{x},t)d\tau \\ \hat{P}_k^- &= \hat{P}_{k-1}^+ + \int_{t_{k-1}}^{t_k} (FP + PF^T + \dot{Q})d\tau \end{aligned} \tag{3.12}$$

For small time-steps, $\triangle t$, forward Euler integration is found to suffice, and the prediction equations simplify to a discrete form:

$$\begin{aligned} \hat{x}_k^- &= \hat{x}_{k-1}^+ + f(\hat{x},t)\cdot\triangle t \\ \hat{P}_k^- &= (I + F\cdot\triangle t)\cdot\hat{P}_{k-1}^+\cdot(I + F\cdot\triangle t)^T + \dot{Q}\triangle t \\ \triangle t &= t_k - t_{k-1} \end{aligned} \tag{3.13}$$

The linearization process alters neither the Kalman gain nor the blending equations. However, the assembly of the *H* and *R* matrices needs to be generalized to account for the asynchronous nature of the measurements provided by the digital sensors.

3.3.2 Measurement Innovation Collection

Measurements close the state estimation propagation loop, providing feedback that keeps the estimate accurate even in the presence of model inaccuracies. The measurements arrive in the measurement buffer asynchronously and at different rates, as described in Section 3.1, and those arriving since the last time-step are processed at the current time-step.

The innovation of a single measurement, denoted by ${}^{m}e_k$ where the superscript ${}^{m}(\cdot)$ denotes the m^{th} measurement received since the last time-step, is the difference between the measurement and the estimate of the measurement. The scalar measurement function, ${}^{m}h$, uses the state estimate to calculate the estimate of the measurement.

$$ {}^{m}e_k = {}^{m}z_k - {}^{m}h(\hat{x}_k^-) \tag{3.14} $$

Unlike the linear KF, which calculates the innovation vector, e_k, from the measurement vector using Equation (3.7), the EKF assembles the innovation vector from the innovation of individual measurements.

$$ e_k\{m\} = {}^{m}e_k \tag{3.15} $$

In Equation (3.15), $\{m\}$ represents the m^{th} entry of the vector. The innovations of the other measurements received at time-step *k* are the remaining entries in e_k.

The measurements arrive in the measurement buffer with delay. For most sensors, the delay is small, and the error caused by ignoring it is negligible compared to the measurement uncertainty. However, the delay is significant for sensors with low update rates, most notably the acoustic positioning sensor. To account for the delay, the state estimate, ${}^{m}\hat{x}^-$, at the measurement time, ${}^{m}t$, is calculated by propagating the current state

estimate back to the measurement time using state dynamics linearized about the current state estimate:

$$ {}^{m}\hat{x}^{-} = \hat{x}_k^{-} - f(t_k, \hat{x}_k^{-}, u_k) \cdot (t_k - {}^{m}t) \tag{3.16} $$

The measurement innovation is then calculated with Equation (3.14) augmented to use the state estimate at the measurement time:

$$ {}^{m}e_k = {}^{m}z_k - {}^{m}h({}^{m}\hat{x}^{-}) \tag{3.17} $$

Other methods of estimating the state at the measurement time, such as keeping a short history of the state estimates as done in [23] and [25], would avoid linearization errors, but would add computational burden and may cause instability in cases with large errors in the estimate history.

3.3.3 Assembly of Measurement Matrices

The measurement sources dictate the assembly of the measurement matrix, *H*, and measurement covariance matrix, *R*. The measurements are discrete and typically not synchronised. For example, the DVL outputs translational velocity at 2Hz, while the IMU reports angular velocity at 20Hz. As a result, multiple combinations of measurements are possible. Time-steps at 0.1s intervals will contain several IMU measurements, and many will not have a DVL measurement at all. Thus, the number of measurements in *z* and the entries in *e*, *H* and *R* can vary.

For each measurement's innovation, ${}^{m}e_k$, a corresponding row in H_k, denoted ${}^{m}H_k$, represents the local gradient of the associated measurement function:

$$ {}^{m}H_k = \left. \frac{\partial({}^{m}h(x, {}^{m}t))^{T}}{\partial x} \right|_{x={}^{m}x} \tag{3.18} $$

For a measurement that is a linear combination of the state variables, ${}^{m}H_k$ is constant and can be pre-calculated. However, for a measurement that is a non-linear combination of the state variables, ${}^{m}H_k$ is state dependent and must be calculated as the measurement is received. Once calculated, ${}^{m}H_k$ is added to the measurement matrix:

$$H_k\{m,1:n\} = {}^{m}H_k \tag{3.19}$$

In Equation (3.19), notation is as follows: {i,j} represents the matrix cells in the ith row(s) and jth column(s); i:j represents a list of integers starting at i and ending at j; n is the number of states in the EKF.

Each measurement also has an associated uncertainty, quantified as an error variance, ${}^{m}\sigma_k^2$. For a single independent measurement, a row and a column are added to the measurement covariance matrix, R_k. The entries of the row and column are zero except the last entry which lies on the diagonal of R_k and is the estimated error variance of the measurement.

$$\begin{aligned} R_k\{1:m-1,m\} &= 0_{m-1,1} \\ R_k\{m,1:m-1\} &= 0_{1,m-1} \\ R_k\{m,m\} &= {}^{m}\sigma_k^2 \end{aligned} \tag{3.20}$$

In Equation (3.20), $0_{i,j}$ represents a matrix of zeros with *i* rows and *j* columns.

The zeros signify that there is no correlation between this measurement and those from other entries in the measurement buffer. This is a reasonable assumption since the measurement buffer entries are either made at different times or by different instruments with independent bias and noise properties. In the case of several values being measured

by the same instrument, a square matrix containing the expected values of the outer product of the measurement errors, w_{meas}, is added to R_k in block diagonal form.

$$\begin{aligned} R_k\{1:m-1, m:p\} &= 0_{m-1,p} \\ R_k\{m:p, 1:m-1\} &= 0_{p,m-1} \\ R_k\{m:p, m:p\} &= E[{}^{m:p}w_k \cdot {}^{m:p}w_k^T] \end{aligned} \tag{3.21}$$

In Equation (3.21), p represents the number of measurements being added as a set. This method of assembling R_k adjusts for the variability of the measurement combinations.

3.4 The EKF for ROV Navigation

The EKF developed in this work uses a suite of sensors tracking a variety of states to accurately estimate ROV position and velocity. Tether disturbance is also estimated with the EKF, even though no force sensors are used. Velocity and tether disturbance states are observed in the ROV reference frame attached to the ROV at the mass centre, and position states are observed in the inertial reference frame. The two frames are related by the Euler angles which are also included in the EKF states. The EKF state vector includes the velocity (u, v, w, p, q, r) in ROV coordinates, position (X, Y, Z) in earth coordinates, Euler angles (ϕ, θ, ψ), and 3 tether disturbance parameters.

$$x \equiv \begin{bmatrix} u & v & w & p & q & r & X & Y & Z & \phi & \theta & \psi & T & \alpha & \beta \end{bmatrix}^T \tag{3.22}$$

Of the three tether disturbance parameters, T represents tether tension, where as α and β represent the bearing and inclination angles of the tether at the attachment point on the ROV. The state variables and coordinate systems are shown graphically in Figure 3-5.

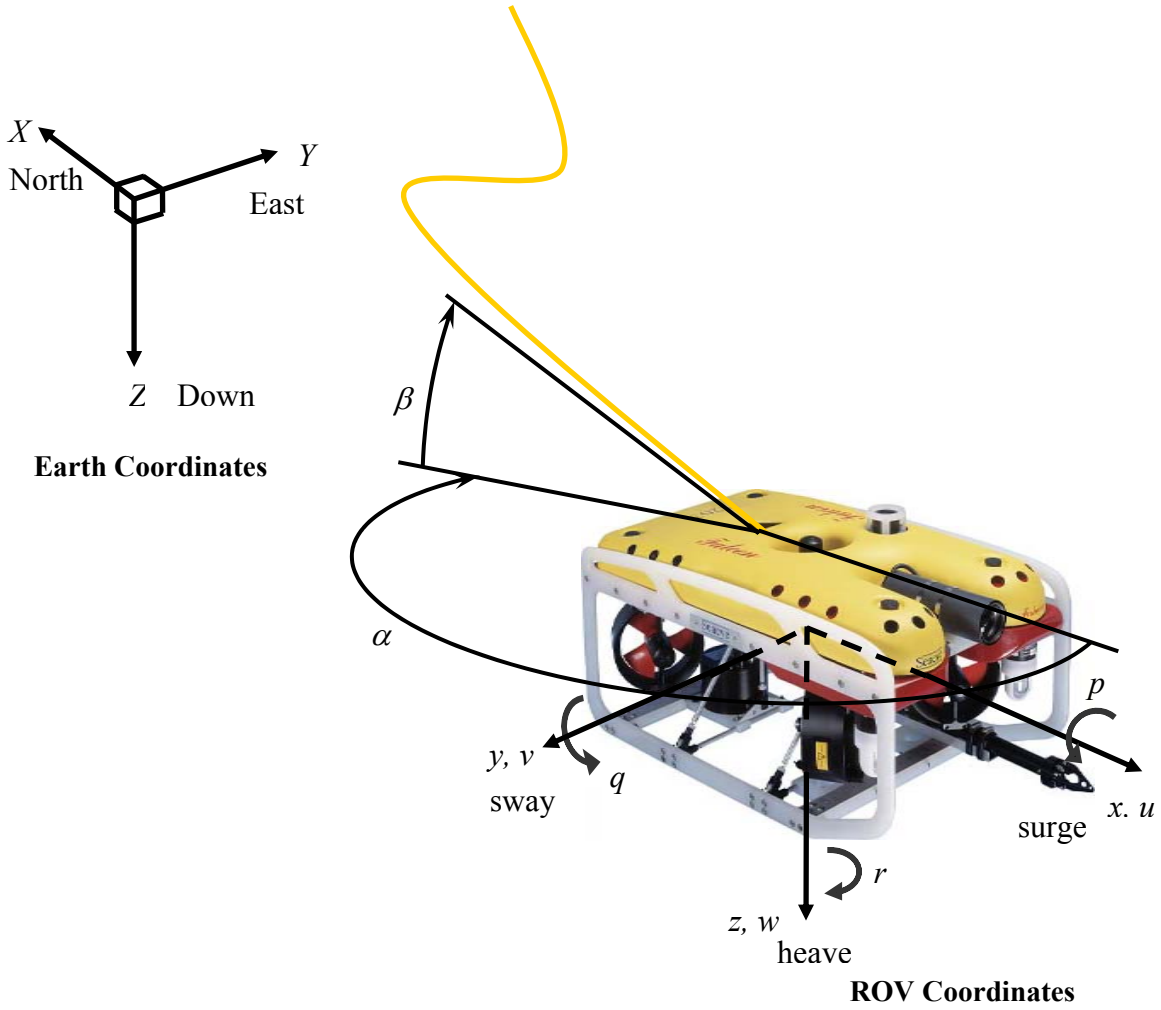

Figure 3-5. ROV Nomenclature Diagram

The ROV dynamics are embedded in the KF to propagate the state through time. The kinetic dynamics that propagate the translational velocity are discussed in Subsection 3.4.1. The kinematic dynamics governing the remaining states are discussed in Subsection 3.4.2.

3.4.1 ROV Kinetics

The time rates of change of the velocities are the accelerations in ROV coordinates, estimated through a kinetic model. An ROV model similar to [16] is selected that

calculates ROV acceleration in ROV coordinates accounting for Coriolis accelerations, thrust forces, tether disturbance, hydrodynamic drag, and added mass.

$$\begin{aligned}\dot{u} &= (v \cdot r - w \cdot q) + (F_{Thrustu} + T\cos(\alpha)\cos(\beta) - F_{Du}) / m_{\dot{u}} \\ \dot{v} &= (w \cdot p - u \cdot r) + (F_{Thrustv} + T\sin(\alpha)\cos(\beta) - F_{Dv}) / m_{\dot{v}} \\ \dot{w} &= (u \cdot q - v \cdot p) + (F_{Thrustw} + T\sin(\beta) - F_{Dw}) / m_{\dot{w}}\end{aligned} \tag{3.23}$$

In Equation (3.23), notation is as follows: $F_{Thrustu}$, $F_{Thrustv}$, and $F_{Thrustw}$ are the applied thruster forces in the surge, sway, and heave directions respectively; F_{Du}, F_{Dv}, and F_{Dw} are the drag forces in the surge, sway, and heave directions respectively; $m_{\dot{u}}$, $m_{\dot{v}}$, and $m_{\dot{w}}$ are the total inertia of the ROV with added mass.

The applied thruster forces, $F_{Thrustu}$, $F_{Thrustv}$, and $F_{Thrustw}$, are tracked with the Falcon™ Monitor and directly influence the EKF process model of the velocity states. The proportion of the applied thrust each thruster exerts in the forward, lateral, and vertical directions are determined by the thruster installation coefficients: η, κ and λ.

$$\begin{aligned}F_{Thrustu} &= \eta F_{Thrust} \\ F_{Thrustv} &= \kappa F_{Thrust} \\ F_{Thrustw} &= \lambda F_{Thrust}\end{aligned} \tag{3.24}$$

The thrust reported by the Falcon™ Monitor is the total thrust in the surge, sway, and heave directions, i.e., a linear combination of the thrusts produced by each thruster:

$$\begin{bmatrix} F_{Thrustu} \\ F_{Thrustv} \\ F_{Thrustw} \end{bmatrix} = \begin{bmatrix} \eta_{PF} & \eta_{SR} & \eta_{SF} & \eta_{PR} & \eta_{V} \\ \kappa_{PF} & \kappa_{SR} & \kappa_{SF} & \kappa_{PR} & \kappa_{V} \\ \lambda_{PF} & \lambda_{SR} & \lambda_{SF} & \lambda_{PR} & \lambda_{V} \end{bmatrix} \begin{bmatrix} F_{ThrustPF} \\ F_{ThrustSR} \\ F_{ThrustSF} \\ F_{ThrustPR} \\ F_{ThrustV} \end{bmatrix} \tag{3.25}$$

The hydrodynamic drag forces, F_{Du}, F_{Dv}, and F_{Dw}, are modeled as quadratic functions of the ROV speed:

$$
\begin{aligned}
F_{Du} &= D_u u + D_{uu} u|u| \\
F_{Dv} &= D_v v + D_{vv} v|v| \\
F_{Dw} &= D_w u + D_{ww} w|w|
\end{aligned}
\tag{3.26}
$$

This model does not account for ocean currents, which lead to differences between the ROV's speed relative to the water and its absolute over-ground speed. The dynamics of the unmodeled phenomena are similar to the tether disturbance dynamics, so significant ocean currents will taint the EKF's estimate of the tether disturbance.

The total inertias of the ROV, $m_{\dot{u}}$, $m_{\dot{v}}$, and $m_{\dot{w}}$, are the sum of the mass of the ROV and the added mass due to the pressure force of water surrounding the ROV during acceleration.

3.4.2 ROV Kinematics

Kinematic models govern the remaining EKF state variables, namely the rotational rates, the position, the Euler angles, and the tether disturbance.

A constant rotation rate model is used, which relies on measurements to introduce any rotational acceleration into the EKF's estimate:

$$
\begin{aligned}
\dot{p} &= 0 \\
\dot{q} &= 0 \\
\dot{r} &= 0
\end{aligned}
\tag{3.27}
$$

The constant angular velocity approximation is acceptable because the IMU's rate gyroscopes provide high frequency measurements. A more sophisticated rotation rate model, which calculates rotational accelerations based on net torques on the ROV, would make the EKF more robust to IMU measurement dropout and improve tether disturbance force estimation. However, a kinetic rotation rate model would require identification of

rotational inertias, thruster force lines of action, and hydrodynamic centers of pressure on the ROV projected faces.

The coordinate transformation matrices T_1 and T_2 map values from ROV coordinates to the earth coordinates [16]:

$$T_1 = \begin{bmatrix} \cos\psi\cos\theta & \cos\psi\sin\theta\sin\phi - \sin\psi\cos\phi & \cos\psi\sin\theta\cos\phi + \sin\psi\sin\phi \\ \sin\psi\cos\theta & \sin\psi\sin\theta\sin\phi + \cos\psi\cos\phi & \sin\psi\sin\theta\cos\phi + \cos\psi\sin\phi \\ -\sin\theta & \cos\theta\sin\phi & \cos\theta\cos\phi \end{bmatrix} \tag{3.28}$$

$$T_2 = \begin{bmatrix} 1 & \sin(\phi)\tan(\theta) & \cos(\phi)\tan(\theta) \\ 0 & \cos(\phi) & -\sin(\phi) \\ 0 & \sin(\phi)/\cos(\theta) & \cos(\phi)/\cos(\theta) \end{bmatrix} \tag{3.29}$$

The time rates of change of the position are calculated by using T_1 to map the translational velocity into earth coordinates:

$$\begin{bmatrix} \dot{X} \\ \dot{Y} \\ \dot{Z} \end{bmatrix} = T_1 \begin{bmatrix} u \\ v \\ w \end{bmatrix} \tag{3.30}$$

The time rates of change of the Euler angles are calculated by using T_2 to map the rotational rates into earth coordinates:

$$\begin{bmatrix} \dot{\phi} \\ \dot{\theta} \\ \dot{\psi} \end{bmatrix} = T_2 \begin{bmatrix} p \\ q \\ r \end{bmatrix} \tag{3.31}$$

As demonstrated in Chapter 2, tether disturbance forces can significantly influence the ROV dynamics. These forces are difficult to model accurately, as they depend on the often contorted profiles formed by the flexible neutrally buoyant tether. Given the modelling difficulties, a sophisticated tether model is not anticipated to provide

significant additional information over the rudimentary model used in this work, which simply describes how this force is likely to vary. Within the EKF process model, the magnitude of the tether tension is assumed to remain constant:

$$\dot{T} = 0 \tag{3.32}$$

The tether direction is separated into bearing and inclination represented by α and β (see Figure 3-5). The tether tangent at the vehicle connection is assumed to rotate much more slowly than the vehicle, and thus, is approximated as stationary in the earth-fixed frame. Then the rate of change of α and β are equal to the reverse of the ROV angular velocity:

$$\begin{aligned} \dot{\alpha} &= -r \\ \dot{\beta} &= -p\sin\alpha - q\cos\alpha \end{aligned} \tag{3.33}$$

Low confidence in the accuracy of the tether disturbance model is relayed to the EKF by setting the corresponding entry in the Q matrix appropriately high. This weighting attributes most of the mismatch between the model-propagated state and the measurement corrections to the tether disturbance states. For example, a sustained ocean current will bias the expected vehicle forcing in much the same way as a tether disturbance, and this bias will appear in the tether disturbance estimate.

3.4.3 Measurement Collection

The Falcon™ ROV's standard navigation pod contains a compass and a depth sensor, which directly measure ψ and Z respectively. The addition of an IMU and a Sparton™ compass provides direct measurements for the six orientation states. The DVL and SBL measure combinations of EKF states.

The rows of H corresponding to measurements directly correlated to the state have a single unity element in the column of the corresponding state, and zeros in the other columns:

$$^{Depth}H_k = \begin{bmatrix} 0_{1,3} & 0_{1,3} & \begin{bmatrix} 0 & 0 & 1 \end{bmatrix} & 0_{1,3} & 0_{1,3} \end{bmatrix} \tag{3.34}$$

$$^{IMU}H_k = \begin{bmatrix} 0_{3,3} & I_{3,3} & 0_{3,3} & 0_{3,3} & 0_{3,3} \end{bmatrix} \tag{3.35}$$

$$^{Sparton}H_k = \begin{bmatrix} 0_{3,3} & 0_{3,3} & 0_{3,3} & I_{3,3} & 0_{3,3} \end{bmatrix} \tag{3.36}$$

In Equations (3.34) to (3.36): $I_{i,i}$ represents an identity matrix of size i; $^{Depth}H_k$, $^{IMU}H_k$, and $^{Sparton}H_k$ represent the measurement matrix entries, $^{m}H_k$, for the Depth sensor, IMU, and Sparton™ compass measurements respectively.

The IMU gyroscopes measure rotation rates in the inertial reference frame, so their measurements include the earth's rotation. The earth's rotation rate is approximately $4x10^{-3}$ deg/s and the bias it causes in the gyroscope measurements is distributed between the pitch, roll, and yaw axes and depends on the IMU's latitude and heading. The bias in yaw rotation was removed through calibration. The influence on pitch and roll rate measurements is neglected because the components of earth's rotation in these directions are less than the measurement noise quantified and presented later in Table 4-9.

The DVL measures its velocity relative to the earth when the instrument is within 100m of the seafloor. The DVL Monitor aligns this measurement with the ROV coordinates, but ROV translation and rotation both contribute to the instrument's measurement.

$$u_{DVL} = \begin{bmatrix} u \\ v \\ w \end{bmatrix} + \begin{bmatrix} 0 & -r & q \\ r & 0 & -p \\ -q & p & 0 \end{bmatrix} \begin{bmatrix} x_{DVL} \\ y_{DVL} \\ z_{DVL} \end{bmatrix} \tag{3.37}$$

Thus, DVL velocity is a linear combination of the rotation rates and the translational velocities. The DVL's measurement matrix entries (${}^{DVL}H_k$), are a function of the DVL position (x_{DVL} , y_{DVL} , z_{DVL}), in ROV coordinates:

$$ {}^{DVL}H_k = \begin{bmatrix} I_{3,3} & \begin{bmatrix} 0 & z_{DVL} & -y_{DVL} \\ -z_{DVL} & 0 & x_{DVL} \\ y_{DVL} & -x_{DVL} & 0 \end{bmatrix} & 0_{3,3} & 0_{3,3} & 0_{3,3} \end{bmatrix} \tag{3.38} $$

The measurement function for the acoustic ranges, h_{SBL} , is a non-linear combination of the ROV position and orientation. The earth-fixed location of the target transducer, r_{TARGET} , is found using the ROV position, orientation, and offset to the target transducer (x_{TARGET} , y_{TARGET} , z_{TARGET}):

$$ r_{TARGET} = \begin{bmatrix} X & Y & Z \end{bmatrix}^T + T_1 \cdot \begin{bmatrix} x_{TARGET} & y_{TARGET} & z_{TARGET} \end{bmatrix}^T \tag{3.39} $$

The distance from the target transducer to each reference station location, r_{REF} , is measured, and the measurement function calculates the expected value:

$$ h_{SBL} = \left| r_{REF} - r_{TARGET} \right| \tag{3.40} $$

Lastly, ${}^{SBL}H_k$ is the local gradient of this range over the state-space:

$$ {}^{SBL}H_k = \left. \frac{\partial h_{SBL}(x, {}^{SBL}t)}{\partial x}^T \right|_{x = {}^{SBL}\hat{x}_k^-} \tag{3.41} $$

However, the dependence of h_{SBL} on the Euler angles is neglected in calculation of ${}^{SBL}H_k$ because the gradient is algebraically complex and the effect is negligible since the target transducer offset is much smaller than the distance between the target and reference transducers.

$$ {}^{SBL}H_k = \begin{bmatrix} 0_{1,3} & 0_{1,3} & 0_{1,3} & \dfrac{r_{TARGET} - r_{REF}}{\left| r_{TARGET} - r_{REF} \right|} & 0_{1,3} \end{bmatrix} \tag{3.42} $$

Unlike the entries of the *H* matrix for the other sensors, ${}^{SBL}H_k$ is not constant.

3.5 The ROV EKF Algorithm

The ROV EKF algorithm is schematically depicted in Figure 3-6. The algorithm starts with an initial rough estimate of the state, $\hat{x}_0$, used instead of the refined estimate of the last time-step, $\hat{x}_{k-1}^+$, and correspondingly high estimated error variances on the diagonal of the state error covariance matrix *P*. This setting makes the EKF rely on initial measurements for early state estimates.

At each step, measurements are collected in the measurement buffer for one time-step while the state estimate is advanced using the dynamics described in Subsection 3.4.1 and Subsection 3.4.2 to form an initial estimate, $\hat{x}_k^-$. The measurements are then processed sequentially with the difference between measured and estimated values filling in the innovation vector, e_k. The *H* and *R* matrices for this time-step are assembled at this time based on the measurement types received. The Kalman gain is calculated, and the refined estimate, $\hat{x}_k^+$, is calculated by adjusting the initial estimate with the innovation vector.

The current time-step's refined state estimate is integrated forward to become the initial estimate of the next time-step. The process then repeats itself recursively.

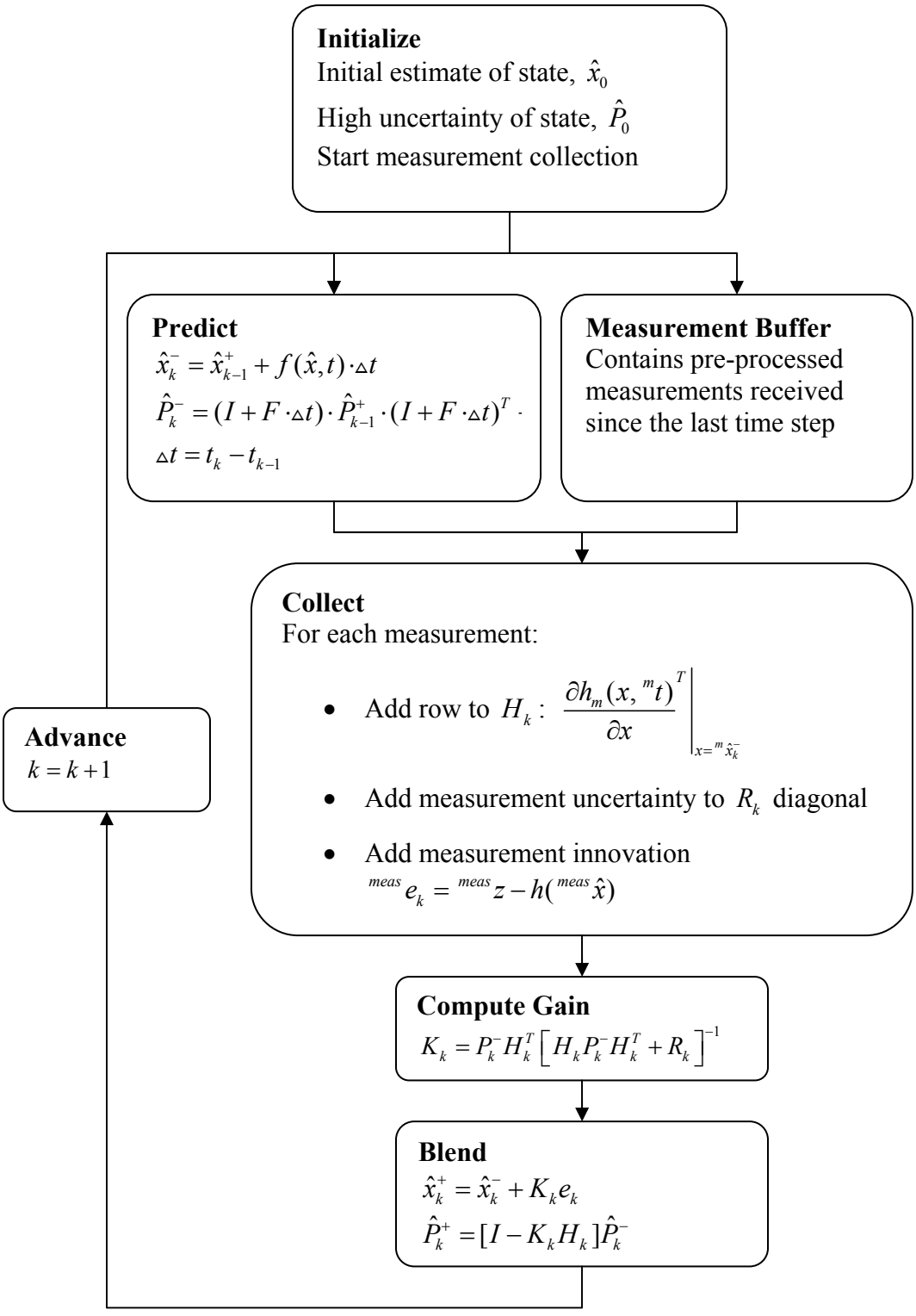

Figure 3-6. The Kalman Flowchart for ROV Navigation

Chapter 4. System Identification

A series of shallow water tests were performed to identify the constants specific to the Falcon™ ROV in the EKF developed in Chapter 3. This chapter presents the test conditions and identifies the parameters. The accuracy of each sensor is estimated in Section 4.2 by comparing measurements with more accurate values. Accurate values on which to evaluate measurement noise are not available during regular deepwater operations. The shallow water tests were conducted in a controlled setting and an optical motion measurement system was used to provide a reference position signal against which the individual sensors, and the EKF as a whole, could be judged. The parameters of the ROV dynamics model are identified in Section 4.3 by analysing measurements made by the onboard sensors during identification manoeuvres in the shallow water test facility. Model errors are characterized in Section 4.4 by scrutinizing the EKF's estimate.

4.1 The Shallow Water Test Facility

Shallow water testing was performed in a 12m long by 5.5m wide boathouse at a saltwater marina. The boathouse provided an enclosed test range with a controlled climate, still water and a surrounding deck that provided room to set-up the ROV and the optical motion measurement system. The SBL reference stations were fixed to the

boathouse enclosure. Thus, acoustic position measurements were obtained in earth coordinates rather than in coordinates moving with a surface vessel. When submerged below the 0.3m depth of the boathouse floats, the vehicle operated in a wide expanse of water. As a result, the acoustic reverberation challenges encountered with pool testing were avoided. Furthermore, covering the boat access and skylights eliminated most ambient light and improved the performance of the optical motion measurement system in daylight hours.

4.1.1 Testing Field

The Falcon™ ROV and its surface equipment were mobilized in the boathouse along side the optical motion measurement system. The water depth was 3m at low tide and 5m at high tide. A walkway lined the edge of the boathouse, leaving a 4.2m wide by 11m long water surface. The earth fixed coordinate system was aligned with the walkways. The SBL positions and compass headings were transformed by their respective monitoring algorithms to be in the X-Y coordinate frame shown in Figure 4-1.

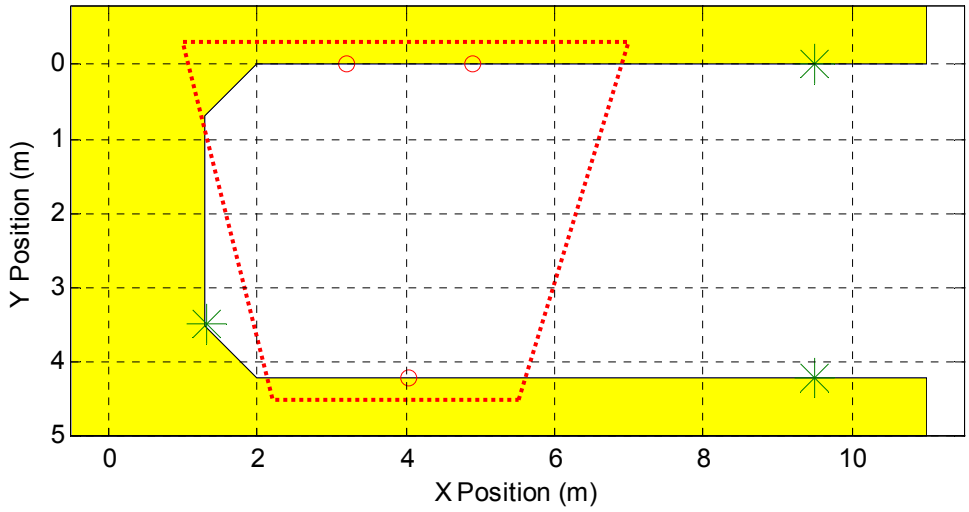

Figure 4-1. Boathouse Layout showing the coordinate system (dashed grid), the dock edges (solid), the optical measurement system's field of view (dotted trapezoid), the optical coordinate markers (circles) and the SBL reference stations (stars). Boat access is from the right side of the figure.

4.1.2 Optical Motion Measurement System Setup

The VZ3000 Visualeyez^{TM} tracking system by Phoenix Technologies Inc. was used to accurately track the ROV position to provide a reference for raw acoustic position measurements and for the EKF estimate. This tracking system measures the position of markers (LED light sources) by viewing them on three cameras at calibrated positions. For the system to determine a marker's location, other light sources must be dimmed below the detection threshold, and line of site must be maintained between the marker and all three cameras. The camera unit was mounted high up the boathouse wall, and faced downward to minimize the influence of ambient light.

As the optical motion measurement system is based on light transmission, the system only works above the water surface. A mast (shown in Figure 4-2) was constructed of thin aluminium tubing and attached to the ROV at the tether attachment point. The mast held the optical markers at fixed locations above the ROV. The mast was stiffened with

guy wires running from the base of the cross on the mast to the forward rails on the ROV. Additional guy wires running aft may have further strengthened the mast but would have occasionally contacted the ROV tether, jolting the mast off location. The mast base was anchored to the ROV's syntactic foam and the tether attachment bracket counteracted the forward pull of the guy wires.

One forward facing and one rear facing marker were placed at each of the three above surface extremities of the mast. The markers were aimed 30deg above horizontal to reduce reflections off the water surface.

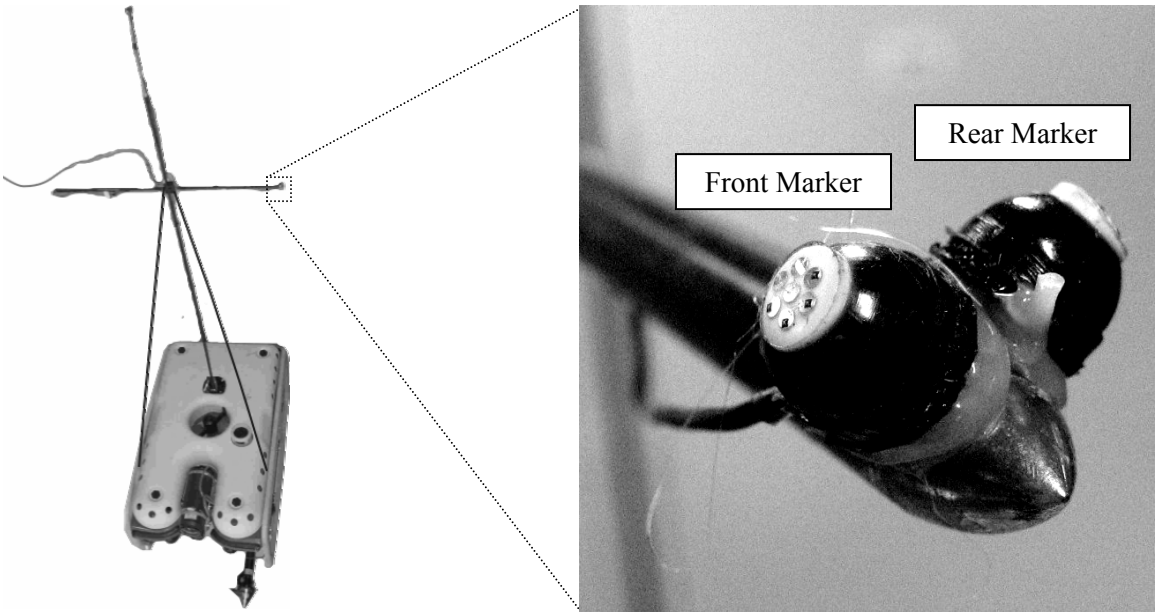

a) Mast to Hold the Markers b) Port Side Markers

Figure 4-2. Optical Markers Mounted to the ROV. The optical markers were attached to an aluminum mast which held the markers above the water throughout the tests.

Stationary markers were fixed to the boathouse walkway to align the optical motion measurements with the boathouse reference frame shown in Figure 4-1. Table 4-1 lists the marker locations; the X-axis was marked with two markers, and the XY plane was marked by a third marker located on the far side of the boathouse.

Marker Reference	X Location (m)	Y Location (m)	Height –Z (m)
Offset Origin	3.194	0	0.65
X axis Direction	4.905	0	0.65
XY Plane	4.045	4.2	0.65

Table 4-1. Visualeyez™ Stationary Marker Locations.

4.1.3 Processing Optical Motion Measurements

The ROV position was extracted from the marker position measurements of the optical motion system using several ROV-fixed reference frames. First a pair of mast-fixed coordinate systems were defined, one based on the front markers, and another in terms of the rear markers. The origins were at the centres of the triangles formed by the top, port, and starboard markers of each side. The x-axis pointed to the top marker, and the y-axis lay in the plane of the triangle. A matrix was defined that transformed the mast-fixed coordinates the ROV coordinates.

The relative orientations and offsets of the mast coordinates to the ROV coordinates were defined through a set of optical motion measurements of the ROV when stationary and above water. During the stationary test, the optical measurement cameras could view the markers on the mast simultaneously with temporary markers placed on the ROV. The temporary markers were placed on the ROV at the locations listed in Table 4-2.

Marker Location	x Location (m)	y Location (m)	Height -z (m)
Vertical Thruster Top Center	0	0	0.18
Wide Angle Camera Top Center	0.48	0	0.18
Target Transducer Top Center	-0.45	0.34	0.15
Sensor Pod Top Center	-0.59	-0.30	0.19

Table 4-2. Temporary ROV Marker Locations (in ROV coordinates) used in the transformations that map the two mast coordinate systems to the ROV coordinates.

The transformation matrices were found by rotating and offsetting the mast coordinate systems until they lined up with the temporary markers on the ROV. This procedure eliminated any misalignment of the markers on the mast and any imperfections in the mast's equilibrium profile. So long as the markers on the mast remained stationary relative to the ROV, the derived transformation matrix calculated the submerged ROV coordinate system location based on the visible mast markers. The calculated ROV positions were not as accurate as the individual marker measurements because the calculation not only relied on mast marker positions, but also on the mast coordinate system orientation, which was poorly conditioned due to limited spacing of the mast markers.

An additional coordinate system with origin at the SBL target transducer was tracked using coordinate transformation matrices calculated in the same way as the ROV coordinate system. This coordinate system was used to evaluate the SBL measurement accuracy.

To resolve each marker's location, all three optical measurement cameras needed to simultaneously view the marker. This limited the optical system's field of view to

roughly a 4m by 4m square. The ROV mounted sensors functioned correctly outside of this area, but optical motion measurements were not available to verify accuracy.

Reflections off the water surface and the aluminum boathouse walls caused occasional inaccurate marker position measurements. Inaccurate position measurements were eliminated with a Matlab™ script that removed measurements made at times when calculated distances between the mast markers deviated in excess of 0.01m from the actual distance between the markers. When one or more markers defining the ROV position was not found, the Visualeyez™ software assumed the ROV had not moved. At these times, the marker measurements were tagged as a 'bad' position measurement, and the associated motion measurements were also rejected by the Matlab™ script. A sample of acceptable and rejected measurements of ROV position using both the forward and rear facing markers are shown in Figure 4-3.

Usually, either all forward facing markers or all rear facing markers faced the cameras and could be tracked, providing frequent ROV position fixes while the ROV mast was within the three cameras' field of view. The filtered optical motion measurements provided highly accurate ROV position fixes at 100Hz. These position fixes were later used as an accurate reference against which to compare the SBL measurements and the EKF estimates.

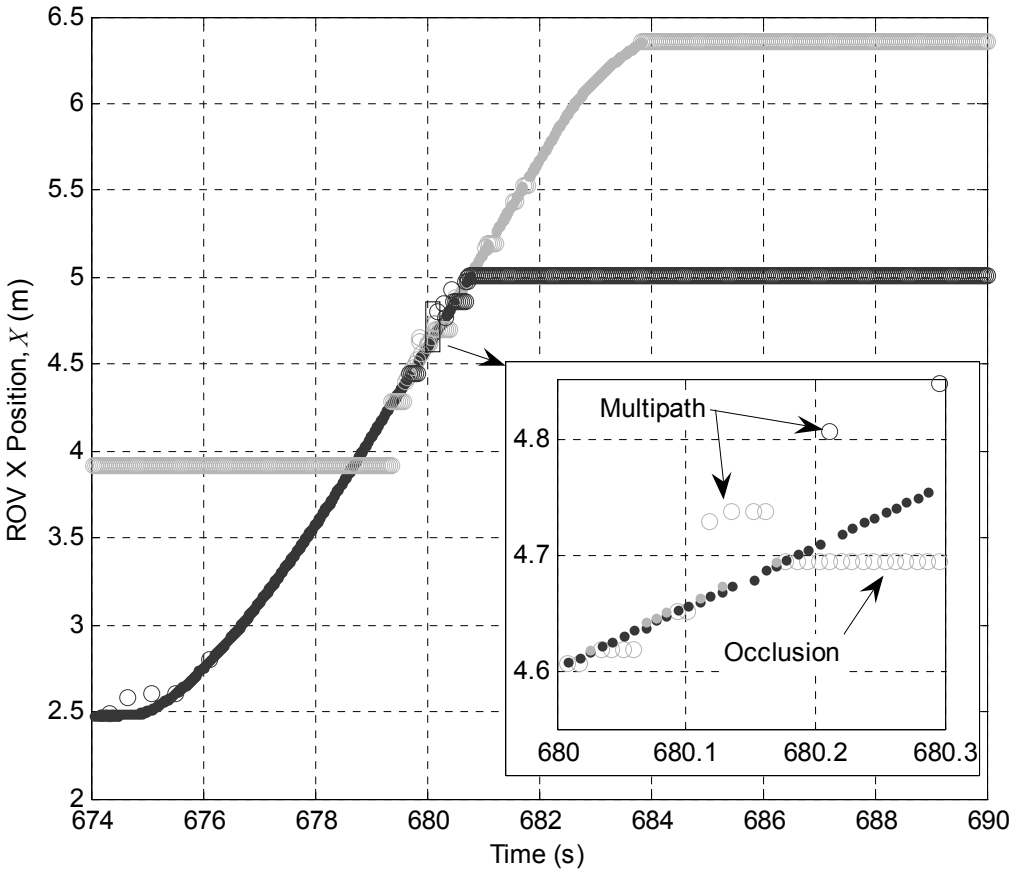

Figure 4-3. Optical Motion Measurements of ROV using forward (dark) and rear (light) facing markers. Good data are shown as dots; rejected data are shown as circles. Up to 679s, the ROV faced the cameras, so only the forward facing markers were correctly tracked. From 679s to 681s the ROV was broadside the cameras, so both sets of markers were visible, but many multipath reflections occurred as the light signal was weak. After 681s the ROV faced away from the cameras, so only the rear markers were correctly tracked. After 684s the ROV moved beyond the field of view of the cameras and no optical position fixes were available.

4.2 Measurement Modeling

The EKF needs to know how much confidence to put into measurements when computing the Kalman gain. This confidence is quantified as the measurement error variance and is specified in the measurement covariance matrix R in Equation (3.21).

Measurement error cannot be identified without knowing the exact value of the quantity being measured. Even in the controlled environment of the boathouse, random errors, time varying biases, and unidentified sensor misalignment caused measurement inaccuracies. Even the optical motion measurements, which provided highly accurate and high frequency ROV positions, were not well suited for tracking other quantities, such as body fixed velocities. Numerical differentiation of the optical position measurement to produce velocities in earth coordinates amplified noise and was also sensitive to errors in the measurement time-stamps. The rotation to ROV coordinates relied on Euler angles, which were also difficult to accurately measure.

To mitigate measurement error, it is important to match the sensing method to the sought after quantity. Measurements of the ROV position, orientation, and velocity provided feedback for the EKF. The estimation of the accuracy of the instruments sensing each of these quantities is explained in the following subsections. These estimated accuracies were used in computing the Kalman gains. The data collected from a 1562s identification manoeuvre where the ROV was piloted throughout the shallow water test facility were used to calculate measurement error properties and identify the system dynamics parameters.

4.2.1 Acoustic Ranging

The PILOT^{TM} SBL tracking system tracked the position of an ROV mounted target transducer (TLT-1) through acoustic interrogation. The ranges between the target transducer and three reference transducers at known locations were measured by time of travel of an acoustic pulse emitted from a reference station, repeated by the target transducer, and received by each reference station.

The SBL system provided measurements at a slower rate than the other sensors. This was because the interrogating transducer required a delay to switch from transmit to receive in order to avoid false readings when beginning to listen for the response signal. Also, the SBL system operated on a dedicated ping frequency, so only one ping was intended to be propagating through the water at any time. Thus the system had to wait for each ping to travel between transducers, and dissipate sufficiently before sending the next ping. The system was configured for transducer ranges on the order of 100s of meters, where round trip travel times could take nearly 1s at a nominal in-water sound speed of 1500m/s. The average update rate was 0.42Hz during the shallow water tests.

During the shallow water tests, the reference stations were hung from the boathouse walkway, at the corners of the boathouse. The reference stations were located at the coordinates listed in Table 4-3.

Reference Station #	X Location (m)	Y Location (m)	Depth (m)
1	9.50 m	4.21 m	0.52 m
2	1.32 m	3.49 m	0.36 m
3	9.51 m	0 m	0.65 m

Table 4-3. SBL Reference Station Locations. Reference stations were hung at surveyed corners of the boathouse.

Stationary tests were performed to check the acoustic positioning system measurements against directly measured target transducer positions. During these tests, the target transducer was held for several minutes at each of several accurately measured locations while the SBL measured the transducer's range to the each of the three reference stations and calculated its location. Figure 4-4 compares the range measurements made by one of

the reference stations to the true range, and shows a bias. Table 4-4 presents the errors of the ranges measured by each reference transducer for all four static tests.

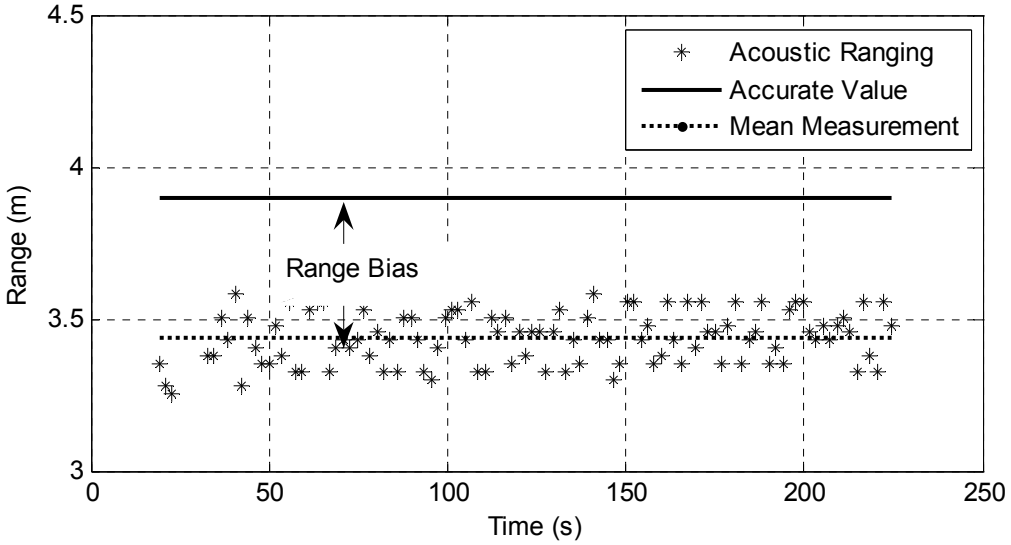

Figure 4-4. Range Measurement Bias Observed during Stationary Testing.

Target Transducer Position			Reference Station 1			Reference Station 2			Reference Station 3		
X	Y	Z	True	Meas	Diff	True	Meas	Diff	True	Meas	Diff
3	0	0.82	7.75	7.31	0.44	3.90	3.44	0.46	6.51	6.09	0.42
8	0	0.82	4.48	4.03	0.45	7.55	7.16	0.39	1.51	0.94	0.57
3	0	0.82	7.75	7.44	0.31	3.90	3.44	0.46	6.51	6.15	0.36
8	-4.2	0.82	1.53	1.02	0.51	6.73	6.28	0.45	4.46	3.98	0.48
Mean Bias					0.43			0.44			0.46

Table 4-4. Range Measurement Bias Observed with Stationary Tests. All values in meters.

All range measurements were shorter than the actual ranges by approximately 0.4m. This constant error was removed during the pre-processing step in the SBL Monitor.

The SBL ranges were also compared against optical motion measurements to observe the effect of motion on the range measurements. The SBL measurements were observed to lag the optical motion measurements by 0.7s, so this delay was subtracted from the

SBL time-stamp before comparing the two measurement series. Figure 4-5 shows the SBL range measurements from each reference transducer, and the more accurate ranges calculated from the optical motion measurements. The variance of the range error was computed by interpolating the optical motion measurements corresponding to the SBL ranges within 0.1s of valid optical motion measurements.

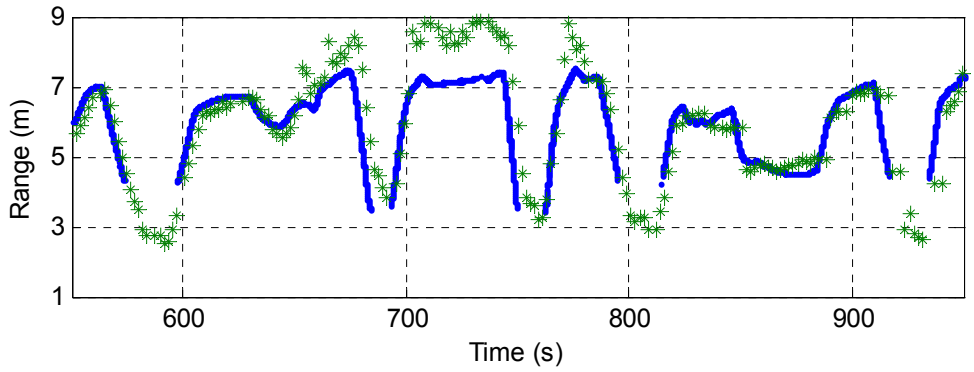

a) Reference Station 1

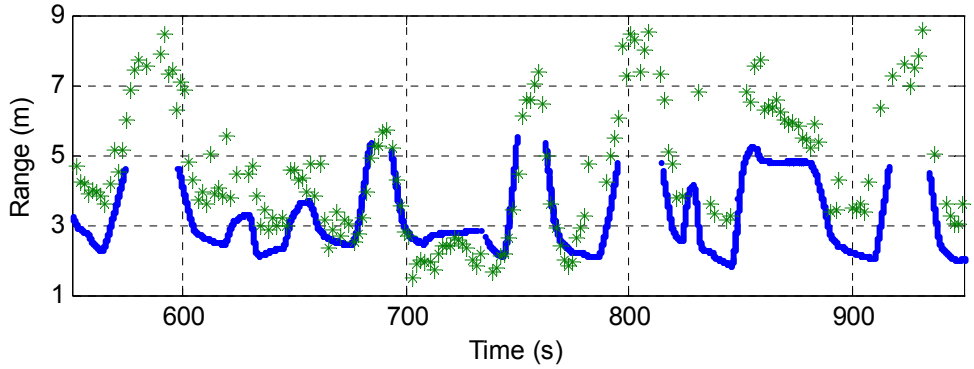

b) Reference Station 2

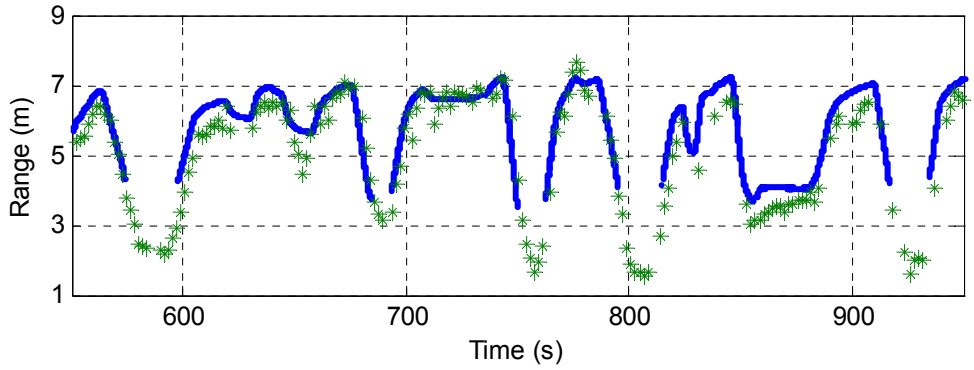

c) Reference Station 3

Figure 4-5. Dynamic Test of SBL Range Accuracy. SBL ranges (star) were compared with ranges calculated from the optical data (broken line). Ranges could only be calculated from the optical data when the ROV optical markers were tracked, so the resulting series appear as broken lines. The range measurements are shown for each reference station.

During the 1562 second identification manoeuvre, 1956 valid range measurements were made by the SBL system. Of these, 1432 range measurements were made when valid optical data were available to use as a reference in calculating the measurement error. The other SBL range measurements were made when neither set of optical markers on the ROV mast was sufficiently visible to make an accurate optical position measurement. Table 4-5 lists the errors in SBL measurements observed during the shallow water identification manoeuvre.

Reference Station #	# of comparable measurements	Range Bias (m)	Range Error Variance (m^2)
1	500	0.33m	$0.64m^2$
2	470	0.34m	$1.01m^2$
3	462	0.09m	$0.58m^2$

Table 4-5. SBL Acoustic Ranging Errors

Even though the range measurement bias observed during the stationary test was removed, a bias was observed in the shallow water identification manoeuvre. The bias may be caused by velocity dependence of the measurement delay or measurement errors in surveying the reference station locations.

Fluctuating measurement errors were quantified as error variance. The range error variances measured in the shallow water test became the entries in the Kalman measurement covariance matrix, R, associated with each reference station range measurement.

The Divebase™ software processed the SBL ranges as they were measured and computed a position measurement when all three reference stations received enough information to calculate their range to the target transducer. The measurements of the

depth sensor on the target transducer were also included in the position measurement computation. However, theses position measurements were recalculated to remove error caused by the constant bias observed in Table 4-4. The SBL position measurements were considered as a benchmark on which to compare the EKF performance.

4.2.2 Depth Sensors

The SBL depth sensor was located in the target transducer and the ROV depth sensor was located in the Seaeye navigation pod. Both sensors measured the ambient water pressure to determine depth. The SBL depth sensor measurements were acoustically transmitted to reference stations, collected by the Divebase™ software, and used in the SBL position calculation. The ROV depth sensor measurements were transmitted to the surface station using the ROV's telemetry, which allowed higher update rates, better resolution, and more robust measurements than the SBL depth measurements. The optical motion measurement system also tracked ROV depth at a rate and accuracy far exceeding the measurements of the two depth sensors. ROV depth measurements made during the shallow water identification manoeuvre are compared in Figure 4-6.

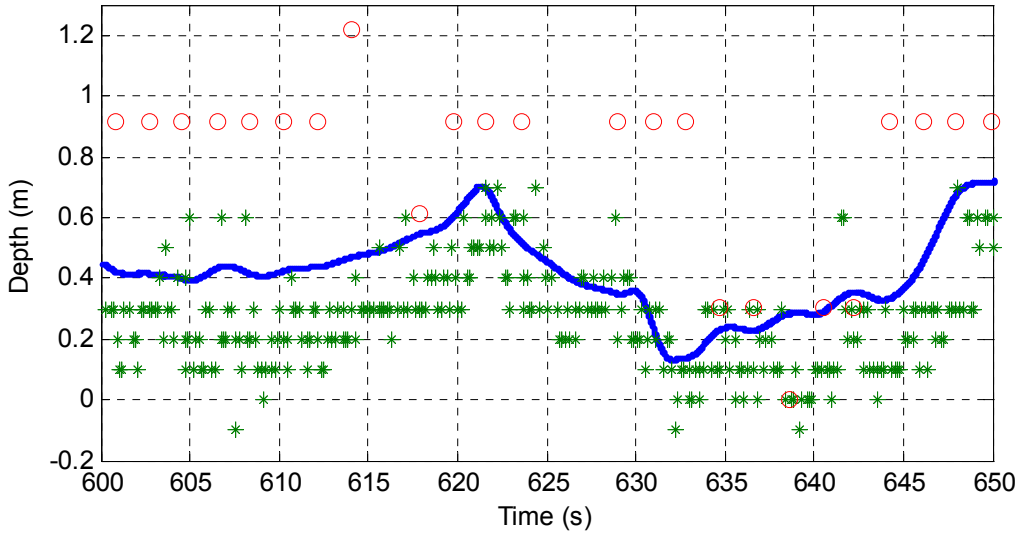

Figure 4-6. Depth Sensor Test. ROV depth measurements made by the depth sensor in the Seaeye navigation pod (stars) and by the SBL depth sensor (circles) were compared with the more accurate optical motion measurements (dark line).

The errors in both the ROV depth sensor measurements and the SBL depth sensor measurements were calculated by using the optically measured ROV depth as the reference values. As with the range errors presented in Subsection 4.2.1, the optically measured depths were interpolated to synchronise with the ROV depth sensor and SBL depth sensor. Table 4-6 lists the measurement rates and the error variances observed for both depth sensors during the 1562s test.

Sensor	Measurement Rate	Error Variance
ROV Depth	10 Hz	0.036 m^2
SBL Depth	0.5 Hz	0.2 m^2

Table 4-6. ROV Depth Measurement Properties.

The measurement rate and accuracy of the ROV depth sensor were far superior to the SBL depth measurements. The error variances presented in Table 4-6 became the entries of the EKF measurement covariance matrix, *R,* associated with the depth measurements.

4.2.3 Doppler Velocity Log

The DVL measured its velocity by transmitting acoustic pulses, and analyzing echoes off the sea floor. By measuring the frequency shift between the transmitted pulse and the received echo, the DVL calculated its speed along the direction of the acoustic beam. The DVL utilized several beams to resolve its velocity into vehicle fixed coordinates. Each of the four circles shown in Figure 4-7 is a transducer that measures the vehicle's speed normal to the transducer's face.

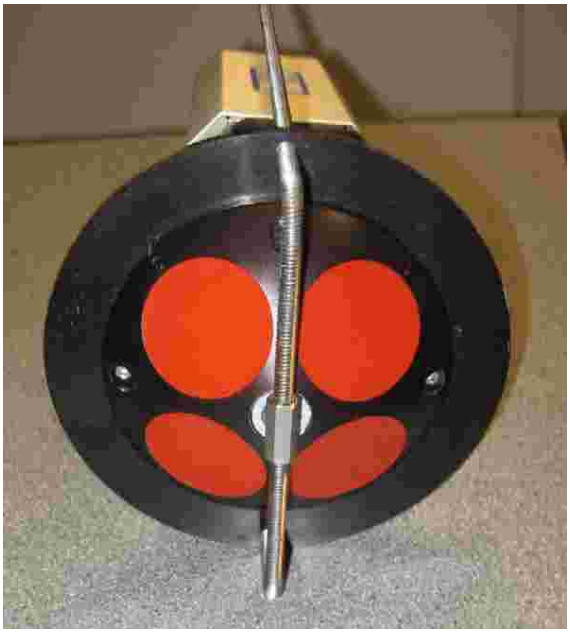

Figure 4-7. Doppler Velocity Log Transducer Head.

The uncertainty of the DVL measurements was estimated by holding the unit stationary and recording the measurements. The resulting characteristics of the measurement series for the zero velocity condition are given in Table 4-7 and were assumed to apply for the non-stationary case as well. A 0.4s measurement delay of the DVL was observed during the shallow water identification manoeuvre, as shown later in Figure 4-11.

Measurement	Quoted Accuracy $(m/s)^2$	Stationary Variance $(m/s)^2$	Bias (m/s)
Surge, *u*	$1.44x10^{-4}$	4×10^{-5}	1.5×10^{-4}
Sway, *v*	$1.44x10^{-4}$	8×10^{-5}	0.7×10^{-4}
Heave, *w*	$1.44x10^{-4}$	1×10^{-5}	0.5×10^{-4}

Table 4-7. DVL Measurement Error

The DVL was configured to ping as fast as possible, and create an ensemble containing the instrument-fixed velocity with every complete set of echoes received. This configuration produced DVL measurements at a rate of 2Hz. Measurement error variance could be reduced by averaging multiple sets of pings into an ensemble, but response to velocity changes would be reduced by the averaging procedure.

4.2.4 Magnetic Compasses

Electronic compasses employ magnetometers to sense the magnetic field as a voltage signal. The magnetic field in the horizontal plane indicates north. Most electronic compasses, including the ones used in this work, use a three axis magnetometer to measure the complete magnetic field and an accelerometer to determine the vertical direction. Typically the magnetometer is in the form of a flux gate, which is a magnetically permeable material wrapped with several coils of wire. An oscillating voltage applied to one coil induces a fluctuating magnetic field in the material, which is sensed by the other coils. The superposition of the applied field to the ambient magnetic field causes the coils aligned with the north-south direction to saturate sooner than those out of alignment.

The Sparton™ compass in the navigation pod output pitch and roll determined with a set of accelerometers, and heading determined from a three axis magnetometer. The Falcon™ onboard compass operated in a similar way, but the pitch and roll

measurements were not entered into the measurement buffer. Measurements from both instruments were reported to their respective monitoring threads at 10Hz.

When either compass was stationary, its measurements had low variance. In this regime, pitch and roll were measured accurately because the only acceleration is gravity. Accurate measurement of compass orientation improved the calculation of heading which required projecting the three dimensional magnetic field onto the horizontal plane. Also, constant magnetic anomalies could cause a bias, but would not add to the variance of the compass measurements when stationary.

The Sparton™ compass was rated to have a $1 \times 10^{-4} rad^2$ ($0.5^2 deg^2$) error variance for stationary heading measurements. When held stationary, its 10Hz measurements had an $8.5 \times 10^{-5} rad^2$ heading variance, which agreed with the specification. The manufacturer of the Falcon™ compass was unknown, so accuracy ratings could not be found. However, a stationary test produced measurements with $5.4 \times 10^{-5} rad^2$ heading variance, suggesting the Falcon™ compass was slightly more accurate than the Sparton™ compass.

Dynamic compass measurements were subjected to higher noise. The pitch and roll finding accelerometers could not distinguish between body acceleration and gravitational acceleration, creating uncertainty in the pitch and roll measurements. Unmodeled magnetic anomalies, which merely cause a bias in the stationary test, would become dynamic errors if the anomalies were not constant through space.

The optical motion measurements, which worked well as a reference for the positioning system, were poorly conditioned for orientation measurements because the mast markers were close together. Consequently, headings calculated from the optical

measurements were not noticeably more accurate than the compass measurements. Instead, the measurements of the Sparton™ and Falcon™ compasses were compared against each other to estimate the measurement error variances of each sensor.

The measurement errors of the Sparton™ compass were assumed to be independent of the Falcon compass' measurement errors, so a differencing approach could be used to calculate the error variance. Subtracting the Falcon™ compass measurements from the Sparton™ compass measurements removed the dynamic true heading, and only the difference of the two measurement sets' errors remained. The variance of the difference of two uncorrelated random variable sets is the sum of each set's variance. This result was manipulated to express the Sparton™ compass' heading measurement error variance, $\sigma^2_{Spar_\psi}$, in terms of the calculable variance of the difference, $\sigma^2_{Spar_\psi - Fal_\psi}$, and the Falcon™ compass' error variance, $\sigma^2_{Fal_\psi}$.

$$\sigma^2_{Spar_\psi} = \sigma^2_{Spar_\psi - Fal_\psi} - \sigma^2_{Fal_\psi} \tag{4.1}$$

The dynamic response of both sensors was assumed to be sufficiently similar that the ratio of the two sensors' variances calculable for the stationary case remained the same for the moving compass:

$$\frac{\sigma^2_{Spar_\psi}}{\sigma^2_{Fal_\psi}} = \frac{8.4\times10^{-5}}{5.4\times10^{-5}} \tag{4.2}$$

This relationship between the error variances of the two compasses allowed Equation (4.1) to be solved for both error variances. Table 4-8 presents the measured and estimated error variances of both compasses.

Measurement	Symbol	Quoted	Stationary	Dynamic
Sparton Heading	$\sigma^2_{Spar_\psi}$	8 x 10^{-5} rad^2 Static	8.4 x 10^{-5} rad^2	3.3 x 10^{-2} rad^2
Sparton Pitch and Roll	$\sigma^2_{Spar_\phi}, \sigma^2_{Spar_\theta}$	1 x 10^{-5} rad^2 Static	6.1 x 10^{-6} rad^2	--
Falcon™ Heading	$\sigma^2_{Fal_\psi}$	-	5.4 x 10^{-5} rad^2	2.2 x 10^{-2} rad^2
Sparton minus Falcon™ Heading	$\sigma^2_{Spar_\psi - Fal_\psi}$	-	1.0 x 10^{-4} rad^2	5.5 x 10^{-2} rad^2

Table 4-8. Compass Measurement Error. Stationary error variances and the dynamic variance of the difference of the two instruments were directly measured. Dynamic error variances of the individual instruments were inferred from the ratio of the static variances and the differenced variance.

4.2.5 Inertial Measurement Unit

The MMQ50™ IMU contained an accelerometer and a rate gyroscope on three orthogonal axes. Only the rate gyroscopes were used for this work. Low cost IMUs are made of micro-machined piezoelectric quartz elements that measure rotational rates and linear acceleration. Angular velocity alters the natural frequency of these piezoelectric elements, whose vibration is digitally measured. Like the DVL, the IMU noise was measured by holding the unit stationary and calculating the variance of the measurements. Table 4-9 lists the error variance and bias of each gyroscope.

Measurement	Quoted	Stationary Test Variance	Stationary Test Bias
X-axis Gyroscope Error	0.003(°/s)^2	0.005 (°/s)^2	-0.026 °/s
Y-axis Gyroscope Error	0.003(°/s)^2	0.010 (°/s)^2	0.025 °/s
Z-axis Gyroscope Error	0.003(°/s)^2	0.008 (°/s)^2	0.080 °/s

Table 4-9. IMU Measurement Error

IMU measurements were received by the IMU Monitor thread at 20Hz. The high measurement rate of this sensor made it particularly useful in creating a low variance estimate of the Euler angles.

4.3 System Identification

The parameters that match the behaviour of the dynamics model given in Subsection 3.4.1 to the Falcon™ ROV were identified through a series of repetitive tests performed in the shallow water test facility referred to in this work as the shallow water identification manoeuvre. System behaviour was observed with the onboard sensors, and the only additional instrument is a strain gauge for thrust measurement.

4.3.1 Thruster Parameters

The total force exerted by the ROV thrusters as a function of the ROV pilot's thrust commands was needed to include thrust forces in the ROV dynamics model. This function was found by identifying each thruster's installation coefficients and the relationship between pilot command and individual thruster forcing.

The thruster installation coefficients described by equation (3.25) were identified by considering the geometry of the thrusters. Figure 4-8 shows the centreline vectors of the ROV's four horizontal thrusters and Table 4-10 lists the vector angles. These thrusters were assumed to be interchangeable with no effect on the system dynamics because they were the same model and used the same cowling. The vertical thruster was also the same model, but its cowling was shorter and built into the syntactic foam.

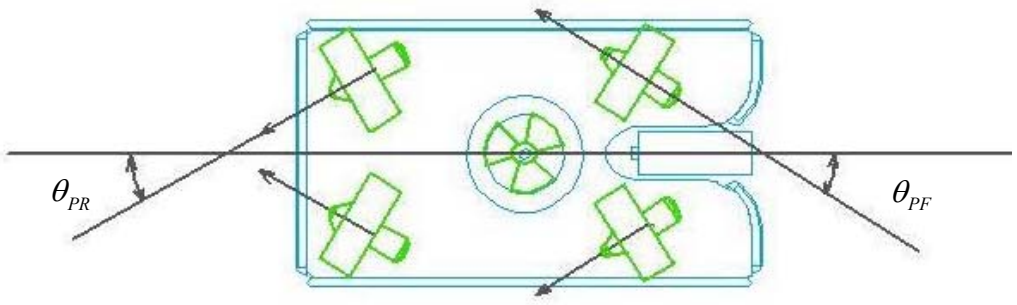

Figure 4-8. The Falcon™ Thruster Arrangement. Four thrusters provided horizontal motion actuation. A vertical thruster provided depth control. All thrusters were the same model.

Thruster Location	Symbol	Value (deg)
Port Forward	θ_{PF}	36°
Port Rear	θ_{PR}	-36°
Starboard Forward	θ_{SF}	-36°
Starboard Rear	θ_{SR}	36°

Table 4-10. Falcon™ Horizontal Thruster Angles

As with most thrusters, those on the Falcon™ ROV exhibit radial symmetry, so each thruster's force was assumed to act along its rotation axis. By considering the magnitude of force exerted by each thruster to be that realized in the installed configuration, the entries of equation (3.25) that convert the individual forcing of the ROV thrusters to net force in the surge, sway, and heave directions were reduced to vector additions:

$$\begin{aligned} \eta_* &= \cos(\theta_*) \\ \kappa_* &= \sin(\theta_*) \\ \lambda_* &= 0 \\ \eta_V &= 0 \\ \kappa_V &= 0 \\ \lambda_V &= 1 \end{aligned} \tag{4.3}$$

In Equation (4.3), the subscript $(\cdot)_*$ denotes each of the horizontal thrusters.

The other thrusters and the ROV hull can divert water flow and cause the thruster installation assumption to be violated. However, the bollard pull tests presented next showed the net force of all the thrusters satisfied the assumption of each thruster's force aligning with its rotation axis.

The relationship between the ROV pilot's thrust commands and the force exerted by each of the thrusters was examined with a set of bollard pull tests performed in the shallow water test facility. For these tests, an axial load-cell was anchored to the dock with a strap. The free end of the load-cell was attached to the ROV with a 10m rope. The rope was attached to the rear of the ROV for the forward surge tests. It was also attached to the front, port side, and starboard side for measuring thrusts in the reverse surge, positive sway, and negative sway directions. Both positive and negative heave thrusts were measured by adding steel weights to make the ROV 14kg negatively buoyant, setting the load-cell in a vertical configuration and attaching the rope to the top of the ROV.

For each thrust direction configuration, the load-cell signal was recorded with a time-stamp synchronised with the thrust commands read off the Falcon™ ROV telemetry. Both the thrust commands for each thruster and the load-cell voltage were recorded at rates of 10Hz. The ROV was piloted away from the load-cell, but restrained in that direction with the rope connecting the two.

Thrust commands were made as step inputs at multiple levels. Each level was sustained for approximately 10s. Figure 4-9 shows the measured thrusts resulting from several commanded thrust step inputs. Figure 4-10 plots all measured surge thrusts over the domain of commanded thrusts. A steep ramp in the force exerted for the upper end of

the commanded thrust required finer thrust steps at this range to resolve the quadratic nature of the relationship and the saturation point of the thrusters.

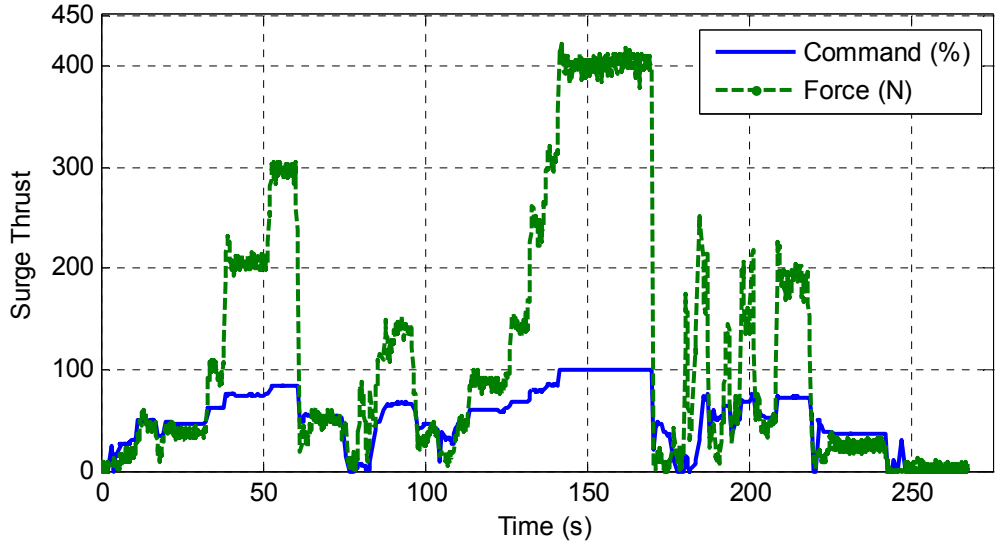

Figure 4-9. Time-series of Commanded and Realized Thrust Forces

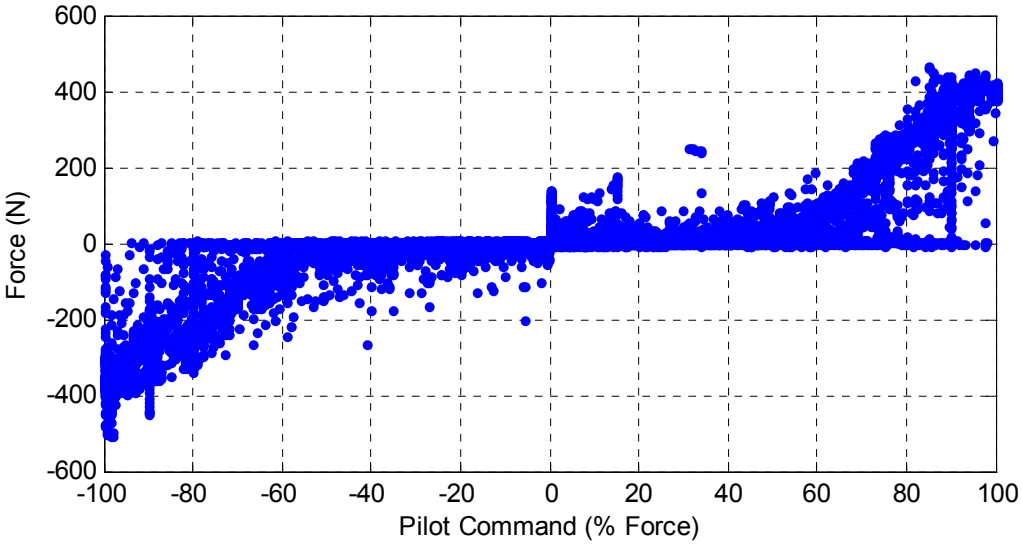

Figure 4-10. Scatter plot of Realized Thrust over the Range of Thrust Commands.

Step inputs in thrust commands were utilized to verify the synchronisation of the commands and the load-cell, highlight the rapid response of the thrusters, and isolate the transient effects of the thrusters. The transient data due to the steps were removed from

the analysis, leaving only the sustained thrust times for use in characterizing the thruster relationship. This steady-state data exhibited a more deterministic relationship shown in Figure 4-11.

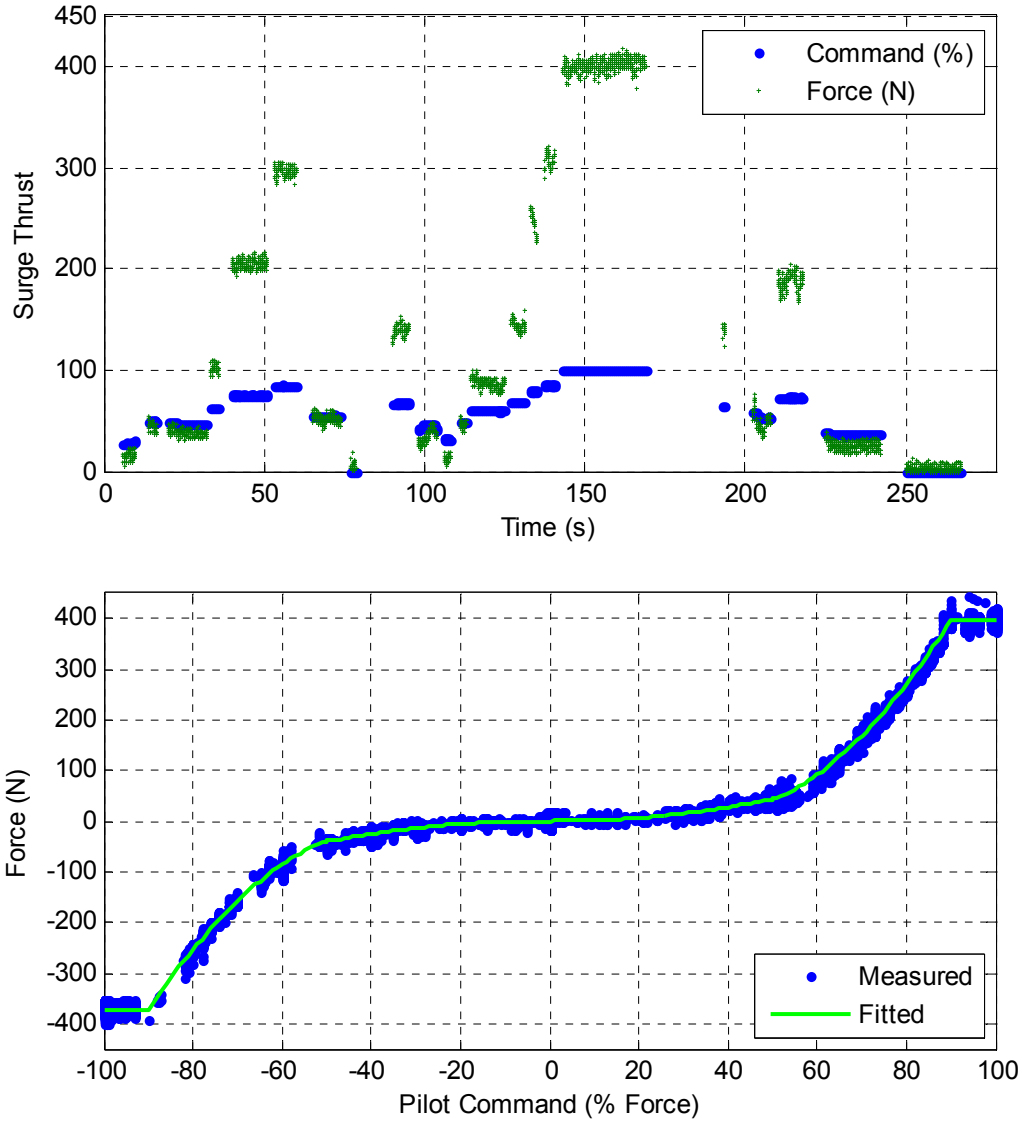

Figure 4-11. Steady-state Surge Thrust Force Response to Thrust Commands. A piecewise quadratic equation was fitted to this data to convert thrust commands into force estimates.

The surge force response had the highest signal to noise ratio, so it was used to determine the output of a single thruster. The sway forces were 70% of the surge forces

realized for the same command magnitude, confirming the assumption that each thruster's forcing direction was along its rotation axis.

The thrusters exhibited a quick response and saturation at 90% thrust. A piecewise quadratic curve was fitted with a least squares approach to relate the pilot's commands to realized thrust force. The magnitudes of reverse thrusts were found to be 94% of the corresponding forward thrust. The Falcon™ Monitor received the thrust commands, F_{cmd} from the ROV telemetry, and provided thruster forces, F_{Thrust}, to the measurement buffer using:

$$\begin{aligned} F_{Thrust} &= 0.0059F_{cmd}^2 - 0.022F_{cmd} \\ F_{Thrust} &= 0.040F_{cmd}^2 - 2.8F_{cmd} + 53.65 \\ F_{Thrust} &= 124 \\ F_{Thrust} &= -0.94F_{Thrust}(-F_{cmd}) \end{aligned} \quad \left\{ \begin{aligned} &0\% \leq F_{cmd} \leq 50\% \\ &50\% \leq F_{cmd} \leq 90\% \\ &90\% \leq F_{cmd} \leq 100\% \\ &F_{cmd} \leq 0\% \end{aligned} \right\} \tag{4.4}$$

4.3.2 Hydrodynamic Drag Estimation

The hydrodynamic drag model defined in Equation (3.26) was parameterized by linear and quadratic coefficients in each of the surge, sway, and heave directions. These drag coefficients were found by piloting the ROV in straight lines with constant force commands and analysing the steady-state applied thrust and velocity. The DVL was used to measure the steady-state velocity. The Falcon™ thrust commands were converted into applied thrusts using Equation (4.4).

Figure 4-12 depicts the ROV accelerating from rest to steady-state velocity as a result of a 19N surge thrust step input. 10s after the thrust increase, The ROV approached a steady-state velocity of 0.24m/s. Therefore, the hydrodynamic drag on the ROV was 19N for a surge speed of 0.24m/s.

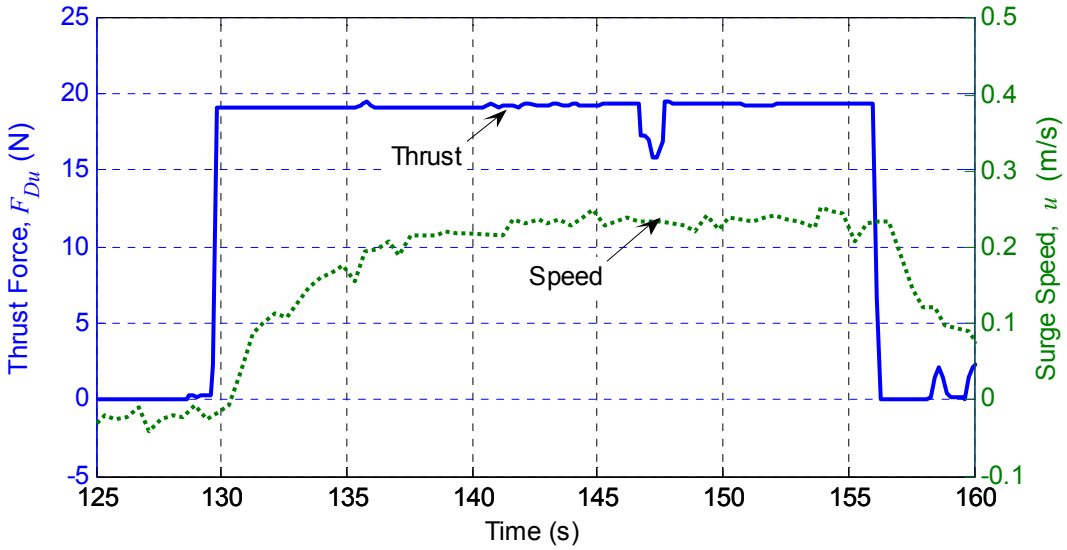

Figure 4-12. ROV Velocity Response to a Thrust Force Step Input. The ROV surge speed (dotted) resulting from a step input of applied thrust (solid) was measured by the DVL. The 19N thrust resulted in a 0.24m/s steady-state speed. The 0.4s delay between thrust step and velocity change was characteristic of the DVL measurements.

The velocity change measured by the DVL lagged the thrust input by 0.4s. There was no significant delay in the thruster response, so the entire delay was attributed to the DVL measurements.

At constant force steady-state, the hydrodynamic drag is the only force opposing the applied thrust. The steady force acceleration up to steady speed manoeuvre was repeated for various applied forces. Figure 4-13 shows steady-state speed achieved for each applied thrust in the surge direction. Similar manoeuvres were performed for each of the surge, sway, and heave directions.

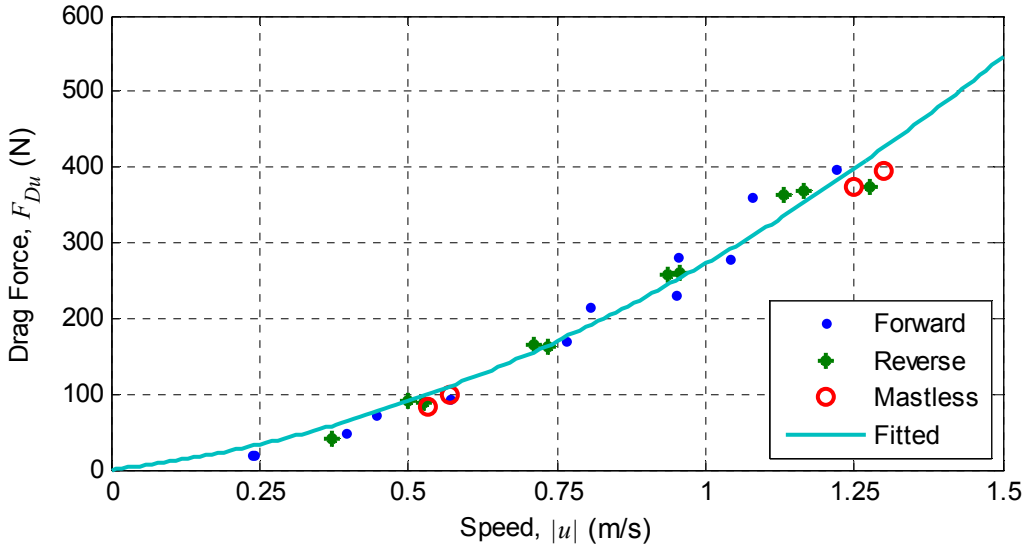

Figure 4-13. Drag Force as a Function of Speed. An origin intersecting quadratic polynomial was fitted to the data using a least squares method. The relationship for the surge direction is shown. Note that the drag force was only slightly reduced by removing the optical marker mast. Drag forces were considered symmetric about the forward and reverse motions.

The hydrodynamic drag coefficients for surge, sway, and heave motions were found by fitting Equation (3.26) to the Falcon™ ROV drag data collected from the shallow water identification maneuver. Table 4-11 lists these drag coefficients and their associated uncertainty.

Direction	R^2	Coefficient	Value	Variance
Surge	0.98	D_u	88.9 N/(m/s)	412 $(N/(m/s))^2$
		D_{uu}	183.7 N/(m/s)^2	373 $(N/(m/s)^2)^2$
Sway	0.98	D_v	86.5 N/(m/s)	1397 $(N/(m/s))^2$
		D_{vv}	541.9 N/(m/s)^2	3920 $(N/(m/s)^2)^2$
Heave	0.96	D_w	173.2 N/(m/s)	2773 $(N/(m/s))^2$
		D_{ww}	230.2 N/(m/s)^2	16877 $(N/(m/s)^2)^2$

Table 4-11. Falcon™ Hydrodynamic Drag Coefficients.

4.3.3 Fluid Inertia Estimation

The inertia of water surrounding the ROV increased the effective inertia of the ROV. The ROV dynamics modeled this phenomenon with the total inertia coefficients: $m_{\dot{u}}, m_{\dot{v}}, m_{\dot{w}}$. The total inertias of the system for surge, sway, and heave accelerations were calculated by analyzing the accelerations resulting from the estimated net forces. The DVL velocity signal was linearly interpolated to synchronise with the Falcon™ thrust signal. The net force on the ROV was calculated as the total thrust force less the drag force. The linear acceleration was found by differentiating the velocity signal. A least squares fit was made to determine the total inertia corresponding to the actuated DOF. The resulting total inertia coefficients and their estimated uncertainty are listed in Table 4-12. This method was sensitive to synchronisation between DVL velocity measurements and thruster commands, and to errors in the hydrodynamic drag modeling.

Direction	Symbol	Value	R^2	Variance
Surge	$m_{\dot{u}}$	281 kg	0.97	109.5 kg^2
Sway	$m_{\dot{v}}$	224 kg	0.81	493.6 kg^2
Heave	$m_{\dot{w}}$	509 kg	0.75	400.5 kg^2

Table 4-12. Falcon™ Inertia – includes the dry mass and the added mass due to the inertia of surrounding water.

4.4 Model Uncertainty Characterization

The last parameters in the EKF that needed to be identified were those that estimated the confidence in the filter's process model to accurately propagate the state. Those parameters formed the entries in the Kalman model error covariance matrix Q. In general, the entries of Q can be nonlinear time varying functions. The entry corresponding to the tether tension estimate, $Q\{13,13\}$, was found to be dependant on ROV acceleration. The remaining entries of Q were constants.

As in prior work [43, 47], Q was assumed to be diagonal. In other words, the error accumulated in the propagation of one state was assumed to be independent of the errors accumulated for all other states. This assumption does not imply that the error in one state is independent of the other states. In Equation (3.13), off diagonal terms in the state Jacobian matrix F apply the appropriate state uncertainty to the covariance matrix P including off diagonal entries in P that capture dependence between any two states. However, a modeling error in one state's propagation function was assumed to have negligible effect on the modeling error of another state's propagation function.

Unlike the simulation based studies in [16], state values were not exactly known in this experimentally implemented work. Earlier works [47, 48] suggested the use of a sophisticated "truth" model to provide reference state values for estimating the Q entries of an EKF whose process model needed to be simplified to run in real-time on primitive computers. However, the ROV model presented in Section 3.4 was deemed to capture the majority of the actual ROV dynamics, so a more sophisticated "truth" model was not available to provide reference state values. Instead, the "truth" reference was produced using the EKF aided by the complete set of instrument measurements.

The shallow water identification manoeuvre was used to estimate the values of Q corresponding to the navigation states. A reference EKF, whose Q entries were overestimated, produced "truth" estimates that relied heavily on the measurements. The accuracy of the EKF process model was identified in stages by hiding select measurements to create an unaided EKF that relied heavily on the EKF process model. The accuracy of the unaided EKF estimate was drastically worse than the "truth" estimate of the fully aided reference EKF. The difference between the estimates of the unaided EKF and the reference EKF was taken to be the error in the EKF process model. The following subsections describe the establishment of the "truth" estimate and unaided EKF for each EKF state.

4.4.1 Constant Rotation Rate Model Uncertainty

First the error variance of the constant rotation rate model was estimated to set the $Q\{4,4\}$, $Q\{5,5\}$, and $Q\{6,6\}$ entries. Underestimating these values would smooth out the estimated rotation rates, but would also reduce the response of the EKF to changes in ROV rotation rate. Without rotation rate measurements, the unaided EKF assumed the rotation rate remained the same as the rotation rate at the last time-step. A change in rotation rate from one time-step to the next was an error in the constant rotation rate model. This error is depicted in Figure 4-14. The variance of this error formed the corresponding entry on the diagonal of the Q matrix.

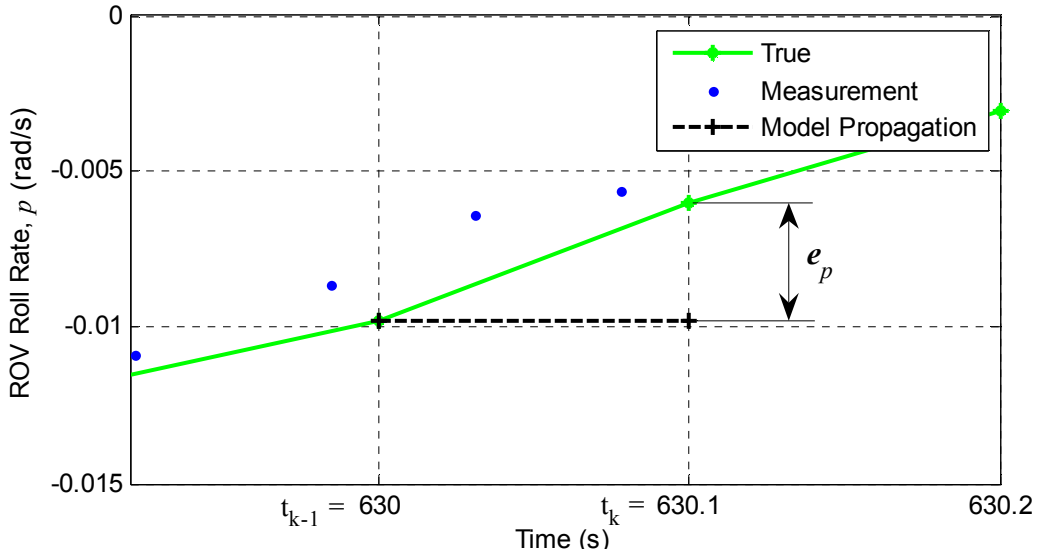

Figure 4-14. Error in Constant Rotation Model. The EKF process model assumed rotation rates remained constant, so a change in rotation rate from time-step to time-step was an error. The variances of these errors for yaw, pitch, and roll formed the corresponding entries in *Q*

The Q diagonal values of the reference EKF were initially all set to 1 x 10^{+2} to heavily weight the measurements. For the rotation rates *p, q, r*, this translates to an average 10rad/s change in rotation rate during each 0.1s time-step – much more than anticipated. The statistics of the variance in rotation rate between each time-step for the test data were calculated with results shown in Table 4-13.

Axis	Mean error	Variance
Roll, *p*	1.7x10^{-7} rad/s	$Q\{4,4\} = 2.4\text{x}10^{-4}$ (rad/s)^2
Pitch, *q*	8.2x10^{-8} rad/s	$Q\{5,5\} = 1.8\text{x}10^{-4}$ (rad/s)^2
Yaw, *r*	1.1x10^{-6} rad/s	$Q\{6,6\} = 5.6\text{x}10^{-4}$ (rad/s)^2

Table 4-13. Constant Rotation Rate Model Errors.

The initial variance settings (1 x 10^{+2}(rad/s)^2) in the Q matrix of the reference EKF were suitably conservative, so the reference EKF estimate was heavily influenced by the measurements. The accuracy of the gyroscope measurements (Table 4-9) , and therefore

of the reference EKF estimate, was one-hundred times better than the rotation model error variance the reference EKF was used to calculate. Therefore, much confidence can be put in the rotation rate model error variance estimate. The $Q\{4,4\}$, $Q\{5,5\}$, and $Q\{6,6\}$ entries were updated to reflect the identified rotation rate model error variance before the reference EKF was used to identify the errors in the Euler angle model.

4.4.2 Euler Angle Model Uncertainty

Next, the uncertainty in the calculation of the Euler angles from the ROV rotation rates p, q and r was examined to set the *Q(10,10), Q(11,11),* and *Q(12,12)* entries. This uncertainty was due to integration truncation, biases in the rotation rates, and errors in the Euler angles (contributing to the T_2 rotation matrix). Unlike the errors in the rotation rate model, these errors could not be clearly observed at each time-step because the compass measurements contained high frequency noise. These errors were observed by filtering the shallow water identification manoeuvre measurements and hiding the compass measurements to form the unaided EKF. The drift error incurred due to loss of compass measurements indicated the uncertainty in the Euler angle propagation model, but only when the drift error far exceeded the accuracy of the reference EKF's orientation estimate. The reference EKF's orientation estimate relied heavily on compass measurements.

Figure 4-15 shows a portion of the test used to identify the errors in the heading propagation model. The compass measurements were removed from the unaided EKF, causing the unaided EKF estimate to accumulate error. After a 1s evaluation interval, the unaided EKF heading estimate was significantly less accurate than the reference EKF's estimate of heading. The difference between the estimates of the unaided EKF and the

reference EKF was attributed to error in the heading propagation model. The unaided EKF estimate of Euler angles was reset to the compass measurements on 1s evaluation intervals, so a large number of drift errors could be observed.

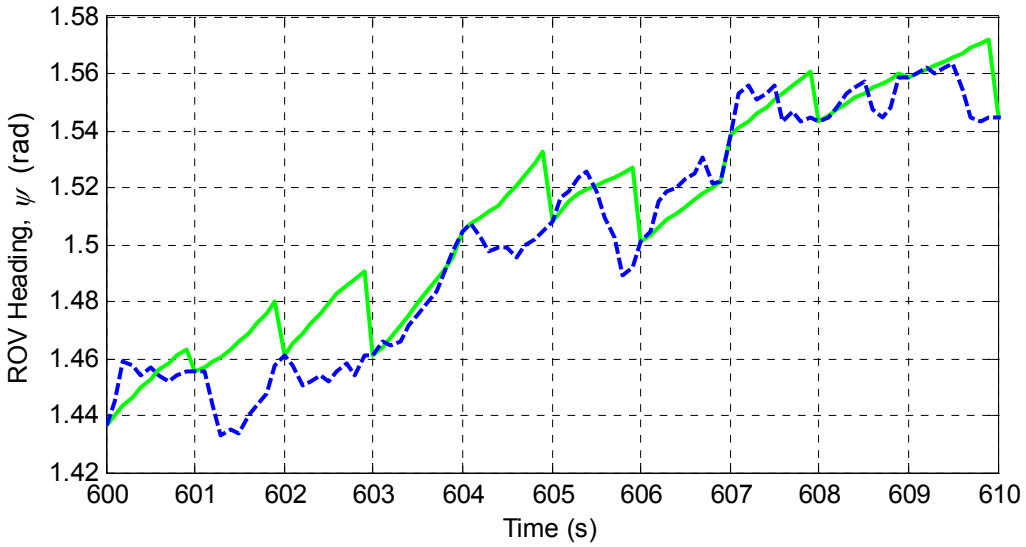

Figure 4-15. Error Accumulation of Model Propagated ROV Heading. The unaided EKF heading estimate (solid) diverged from the reference EKF estimate (dashed). The unaided EKF estimate was reset on 1s evaluation intervals with the reference EKF estimate.

The drift errors resulting from excluding the compass measurements from the EKF were observed on 1s and 10s evaluation intervals over the test data. The variances of these errors are shown in Table 4-14. The EKF Q formulation assumed that process error variances increased at a constant rate with time. The results verified this assumption, as the error variance calculated using 1s evaluation intervals was observed to be approximately ten times less than the error variance calculated using 10s evaluation intervals. Thus the Euler angle model error variance used with the 0.1s time-step EKF was expected to be ten times less than the error variance calculated using 1s evaluation intervals, and one-hundred times less than that using 10s evaluation intervals.

Axis	Error Variance after 1s Evaluation Intervals	Error Variance after 10s Evaluation Intervals	Estimated Model Error Variance
Roll, ϕ	$4.2\text{x}10^{-3}$ rad^2	$1.3\text{x}10^{-2}$ rad^2	$Q\{10,10\} = 2\text{x}10^{-4}$ rad^2
Pitch, θ	$3.7\text{x}10^{-3}$ rad^2	$1.4\text{x}10^{-2}$ rad^2	$Q\{11,11\} = 2\text{x}10^{-4}$ rad^2
Yaw, ψ	$3.1\text{x}10^{-3}$ rad^2	$3.0\text{x}10^{-2}$ rad^2	$Q\{12,12\} = 3\text{x}10^{-4}$ rad^2

Table 4-14. Euler Angle Model Errors. As expected, the error variance after 10s evaluation intervals was approximately ten times that of the 1s evaluation intervals. The EKF increments in 0.1s time-steps, so its error variance was estimated to be one-hundredth the error variance of the 10s evaluation intervals. Notice also that the error variances of each axis were approximately equal since they used the same type of process and measurements.

The *Q(10,10), Q(11,11),* and *Q(12,12)* entries were updated to reflect the identified Euler angle model error variances before the reference EKF was used to identify the errors in the velocity model.

4.4.3 Velocity Model Uncertainty

Next, the process noise in the translational velocity model was examined. The model error was observed by removing the DVL and SBL measurements, so the resulting unaided EKF velocity estimates were based solely on the model's processing of applied thrust, hydrodynamic drag, and tether disturbance. The resulting velocity estimates accumulated error with time. The velocity estimates were reset to the reference EKF velocity estimate on 10s evaluation intervals. Figure 4-16 compares the surge velocity estimates of the unaided EKF to those of the reference EKF.

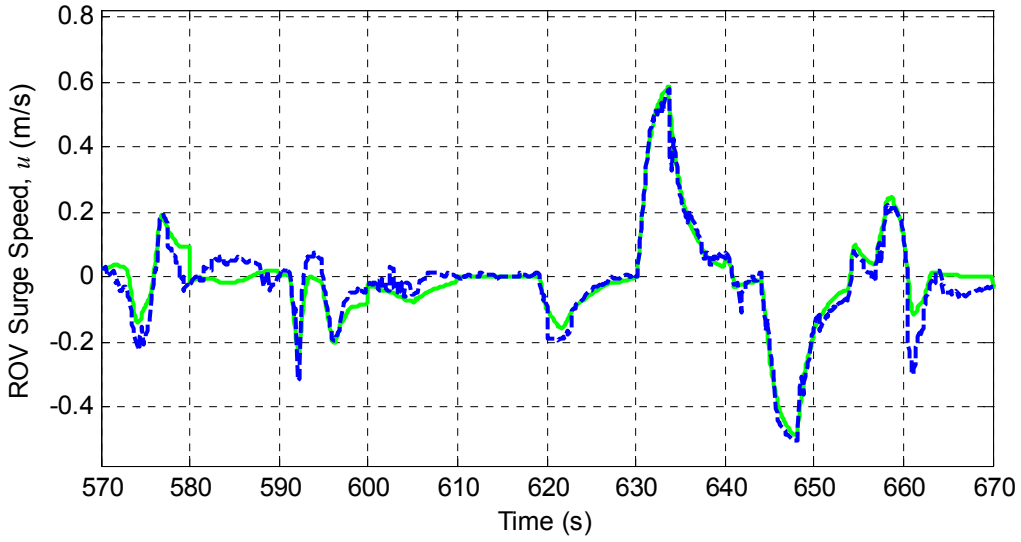

Figure 4-16. Body Fixed Velocity Model Errors. Without DVL or SBL measurements, the unaided EKF estimate (solid) diverged from the reference EKF estimate (dashed). The unaided EKF estimate was reset to the reference EKF estimate on 10s evaluation intervals. However, unlike the Euler angle case, damping in the velocity model stopped the error from growing unbounded.

Since the DVL innovation variance was much larger than the estimated DVL measurement error variance (Table 4-7), the innovation variance was assumed to be due to model error. The velocity model error variances, $Q\{1,1\}$, $Q\{2,2\}$, and $Q\{3,3\}$, which represent the model error accumulation at 10Hz, were set to one-fifth of the innovation variance which was measured at 2Hz. Whereas the calculation of the Euler angle model variance required relatively long times to distinguish the model induced error, the velocity model error variance could be characterized on a short time scale due to accurate DVL measurements. Also, errors in the model predicted velocity did not accumulate at constant rates beyond a 2 second evaluation period because extreme estimates in velocity were damped with hydrodynamic drag. Table 4-15 lists the measurements of model

propagated velocity error variances and states the selected model error variance estimates.

Axis	Innovation Variance (2Hz)	Error Variance at 10s Evaluation Intervals	Estimated Model Error Variance
Surge, *u*	$3.5\text{x}10^{-3}$ $(\text{m/s})^2$	$1.6\text{x}10^{-1}$ $(\text{m/s})^2$	$Q\{1,1\} = 7\text{x}10^{-4}$ $(\text{m/s})^2$
Sway, *v*	$4.8\text{x}10^{-3}$ $(\text{m/s})^2$	$1.1\text{x}10^{-1}$ $(\text{m/s})^2$	$Q\{2,2\} = 9.6\text{x}10^{-4}$ $(\text{m/s})^2$
Heave, *w*	$1.8\text{x}10^{-3}$ $(\text{m/s})^2$	$9.0\text{x}10^{-1}$ $(\text{m/s})^2$	$Q\{3,3\} = 4\text{x}10^{-4}$ $(\text{m/s})^2$

Table 4-15. Body Fixed Velocity Model Errors.

4.4.4 Position Model Uncertainty

The process noise of the ROV position states was determined with an EKF unaided by the SBL and depth measurements. ROV position tracked by the optical motion measurement system was used instead of the reference EKF to calculate the position error. After each evaluation period, the difference between the unaided EKF estimate of position and the optical motion measurement was taken to be the accumulated model error. The unaided EKF estimate was then reset to the optical motion measurement and allowed to progress for the next evaluation period. The process was then repeated for the duration of the shallow water identification manoeuvre. Figure 4-17 shows the resulting error accumulated in X position after each 10s evaluation interval.

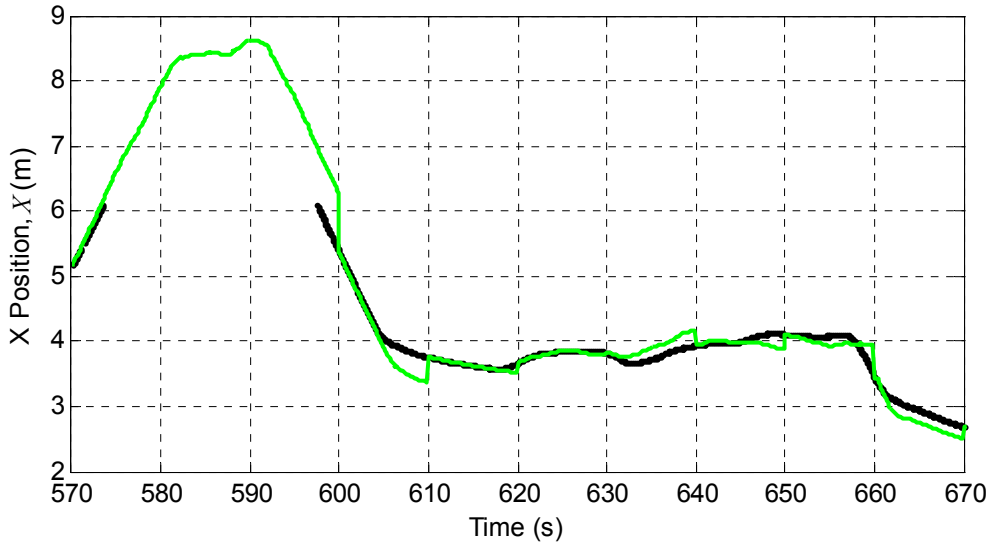

Figure 4-17. Test of Position Model Uncertainty. Accumulation of error in the unaided EKF position estimate (continuous line) was evaluated with the more accurate optical motion measurements (broken line). The drift error was reset every 10s with the optical data measurement.

The position model uncertainty estimates are listed in Table 4-16. Like the Euler angle model, position error was observed to accumulate at a constant rate.

Direction	Error Variance at 1s Evaluation Intervals	Error Variance at 10s Evaluation Intervals	Estimated model error variance
North, X	$1.3\text{x}10^{-2}$ m^2	$1.1\text{x}10^{-1}$ m^2	$Q\{7,7\} = 1\text{x}10^{-3}$ m^2
West, Y	$1.0\text{x}10^{-2}$ m^2	$1.3\text{x}10^{-1}$ m^2	$Q\{8,8\} = 1\text{x}10^{-3}$ m^2
Depth, Z	$4.6\text{x}10^{-3}$ m^2	$5.6\text{x}10^{-2}$ m^2	$Q\{9,9\} = 5\text{x}10^{-4}$ m^2

Table 4-16. Position Model Errors – using optical data for reference.

4.4.5 Tether Disturbance Model Uncertainty

The tether disturbance states (T, α, β) were defined in ROV coordinates and modeled as constant in the earth fixed frame (Equations (3.32) and (3.33)). However, the actual tether disturbance fluctuated during ROV manoeuvres. The EKF estimate of tether disturbance did change throughout the manoeuvres, but only as a result of model

mismatch in the ROV acceleration. The gross approximations of the tether disturbance model produced large uncertainties in its estimates, which were reflected in large model error variance estimates of the tether disturbance states.

Unlike the other states, tether disturbance was not experimentally measured. A "truth" model [47, 48], in the form of the high fidelity cable and ROV simulation discussed in Section 1.5, was used to identify errors in the process model for the tether disturbance states. In the simulation, the ROV manoeuvred at 200m depth through the arbitrary path shown in Figure 4-18. The surface end of the tether mimicked conventional tether tending: the top end of the tether was deployed and retrieved to maintain a constant 20N tension; its location moved to keep the tether near the surface vertical.

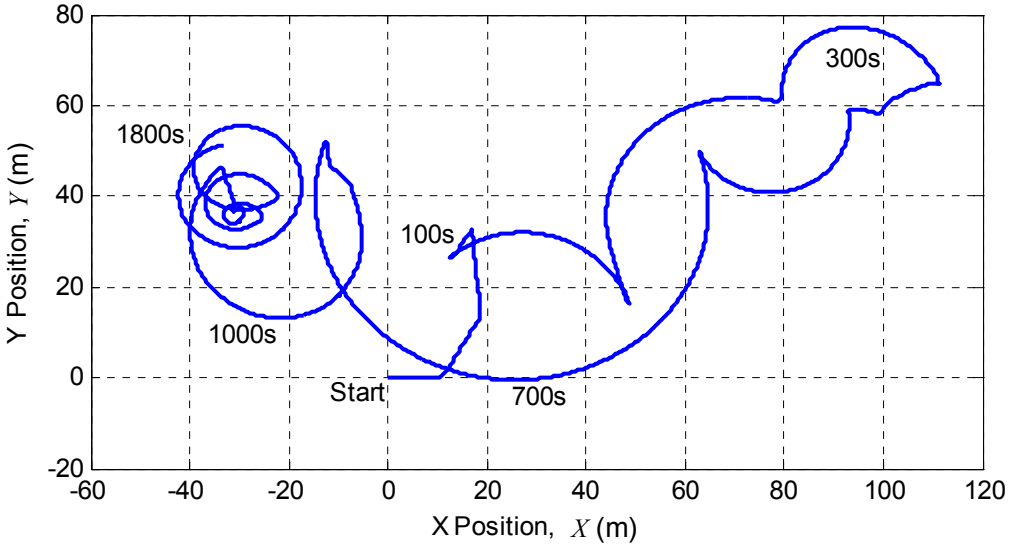

Figure 4-18. Manoeuvre for Tether Disturbance Model Error Identification (plan view). An 1800s manoeuvre was simulated at 200m depth, with the ROV starting at (0,0) and surging, swaying, and yawing through an arbitrary path.

The simulation recorded the tether force on the ROV, along with ROV position and velocity. The time-series for the simulated values of the tether disturbance states (T, α, β) were calculated from the simulation data using:

$$
\begin{aligned}
T &= \sqrt{T_x^2 + T_y^2 + T_z^2} \\
\alpha &= \tan^{-1}\left(T_y \Big/ T_x \right) \\
\beta &= \tan^{-1}\left(T_z \Big/ \sqrt{T_x^2 + T_y^2} \right)
\end{aligned}
\tag{4.5}
$$

In Equation (4.5), T_x, T_y and T_z represent the tether disturbance in ROV coordinates. The EKF tether disturbance model estimates ($\hat{T}_k, \hat{\alpha}_k, \hat{\beta}_k$), were calculated by using Equation (3.32) and Equation (3.33) to advance the simulated tension states by one Kalman time-step:

$$
\begin{aligned}
\hat{T}_k &= T_{k-1} \\
\hat{\alpha}_k &= \alpha_{k-1} + (t_k - t_{k-1}) \cdot (-r_{k-1}) \\
\hat{\beta}_k &= \beta_{k-1} + (t_k - t_{k-1}) \cdot (-p_{k-1} \sin \alpha_{k-1} - q_{k-1} \cos \alpha_{k-1})
\end{aligned}
\tag{4.6}
$$

The error in the EKF tension model was the difference between the estimated values ($\hat{T}_k, \hat{\alpha}_k, \hat{\beta}_k$) and the simulated values (T_k, α_k, β_k). Error in the tension state, *T*, increased during maneuver changes. Figure 4-19 compares the tension state error to acceleration of the ROV.

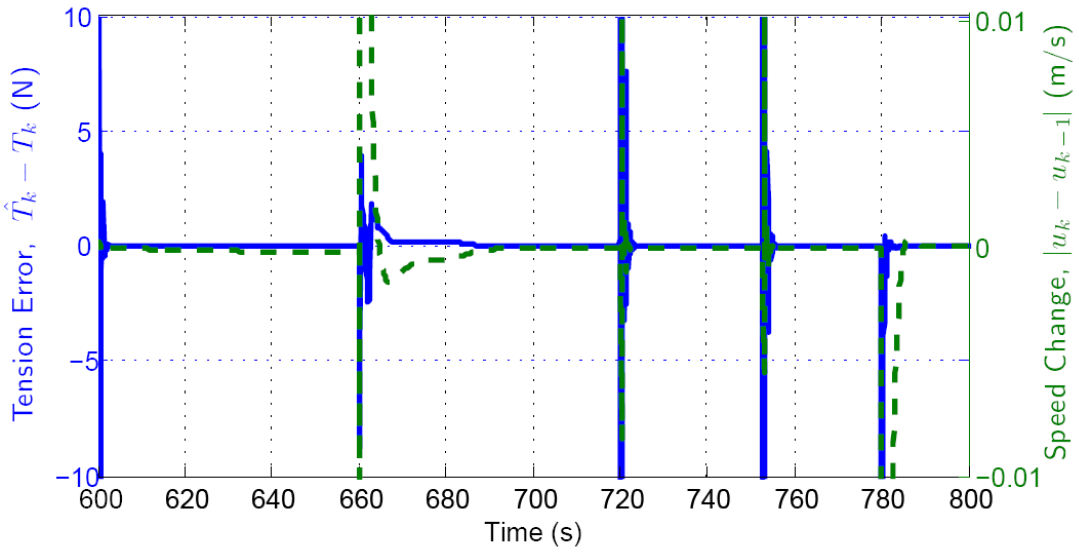

Figure 4-19. Influence of ROV Acceleration on Tether Tension. Tension change between 0.1s time-steps (solid) followed the constant tension model except during manoeuvre changes (at 600s, 660s, 720s, 750s, and 780s) as indicated by ROV acceleration (dashed).

The large increase in error of the EKF tether tension model during manoeuvre changes was accounted for by setting the estimated error variance, $Q\{13,13\}$ according to a time varying value based on the change in ROV speed between time-steps. A linear function modeled this relationship:

$$Q\{13,13\} = E[(\hat{T}_k - T_k)^2] \hat{=} 9\times10^{-1} + |u_k - u_{k-1}|\times10^3 \tag{4.7}$$

Propagation errors in the α and β models were more constant over the simulated manoeuvre, and therefore were estimated directly by taking the variance of the error observed in the EKF estimates. Table 4-17 lists the estimated error variances of the tether disturbance model.

State	Symbol	Model Error Variance
Tether Tension	T	$Q\{13,13\} = 9\times10^{-1} + \lvert u_k - u_{k-1}\rvert \times 10^3\,\mathrm{N}^2$
Tether Bearing	α	$Q\{14,14\} = 3.0\text{x}10^{-5}\ \mathrm{rad}^2$
Tether Inclination	β	$Q\{15,15\} = 6.0\text{x}10^{-4}\ \mathrm{rad}^2$

Table 4-17. Tether Disturbance Model Estimated Error Variance.

4.5 Parameter Identification Closing Remarks

The parameters that govern the ROV dynamics and Kalman gain calculations were quantified through analysis of the shallow water identification manoeuvre. Measurement error variances were estimated for each sensor used in the EKF. Relationships between thrust commands and actuated thrust forces were identified with bollard pull tests. ROV hydrodynamic parameters were identified by comparing the thrust forces with the resulting ROV velocity. The accuracy of the ROV dynamics in advancing each EKF state was also estimated. The EKF used these parameters to estimate the ROV position and velocity during the near surface test manoeuvre presented in Chapter 5 and the deepwater manoeuvre presented in Chapter 6.

Chapter 5. Near Surface Position Tracking Results

The EKF developed in Chapter 3 and Chapter 4 was tested with actual sensor data collected during a near surface test manoeuvre in the shallow water test facility. The accuracy of the EKF estimate was evaluated through comparison with the highly accurate position data provided by the optical motion measurements that were described in Subsection 4.1.2. The optical motion measurements were much more accurate and were refreshed at a much higher frequency than GPS which is the conventional reference for experimentally testing UUV KFs.

This chapter presents the experimental validation of the EKF via a near surface test manoeuvre in the shallow water test facility. The chapter starts with a description of the near surface test manoeuvre. Next the EKF position tracking performance is presented and compared against the conventional SBL performance. In Section 5.5, the merits of including the relatively expensive DVL are evaluated by examining the EKF performance with and without DVL measurements.

5.1 The Near Surface Test Manoeuvre

In the near surface manoeuvre, the ROV had to maintain a depth of less than 1m and stay within the confines of the shallow water test facility as long as the optical motion

measurement markers were connected to the ROV to avoid submerging the optical LED markers. EKF accuracy was directly verified only at times when sufficient markers were in field of view of the optical motion measurement system to yield a valid optically measured ROV position. The spatial domain of the test manoeuvre was expanded by: (1) disconnecting the communication line of the optical motion measurement system from the ROV mast part way through the test; (2) driving the ROV out into the marina and back; and (3) reconnecting the communication line before ending the test. Figure 5-1 shows a plan view of the test manoeuvre.

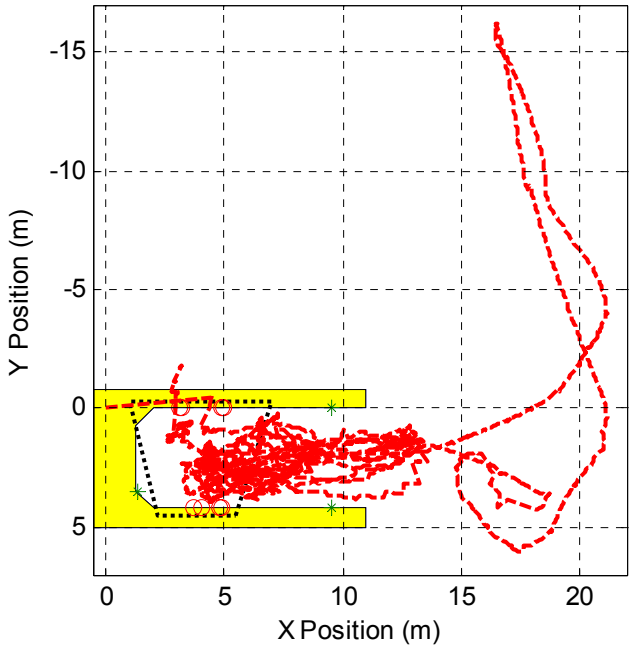

Figure 5-1. Plan View of the Near Surface Test Manoeuvre showing the EKF estimated ROV path (dashed line). Most of the manoeuvre was performed inside the shallow water test facility (shaded area denotes surrounding dock). When the ROV was within the field of view of the optical motion measurement system (dotted trapezoid), its position could be accurately tracked. To expand the test region, the ROV was driven out into the marina half way through the test.

The expansion of the test field into the marina extended the scale on which the EKF was tested. In addition, reconnecting the communication line of the optical motion measurement system for the last part of the manoeuvre identified any long term drift in the EKF position estimate and instability in the error estimate.

5.2 ROV Position Estimation

Tracking the ROV position in the horizontal plane is perhaps the most difficult but useful part of ROV navigation. The EKF estimated the ROV position based on acoustic ranging measurements and the estimate of the ROV velocity and orientation. In Figure 5-2, the time-series of the EKF estimate of horizontal position during the shallow water test is compared to the acoustic and optical position measurements. The EKF estimate of ROV depth was strongly influenced by the onboard depth sensor and is discussed separately in the next subsection.

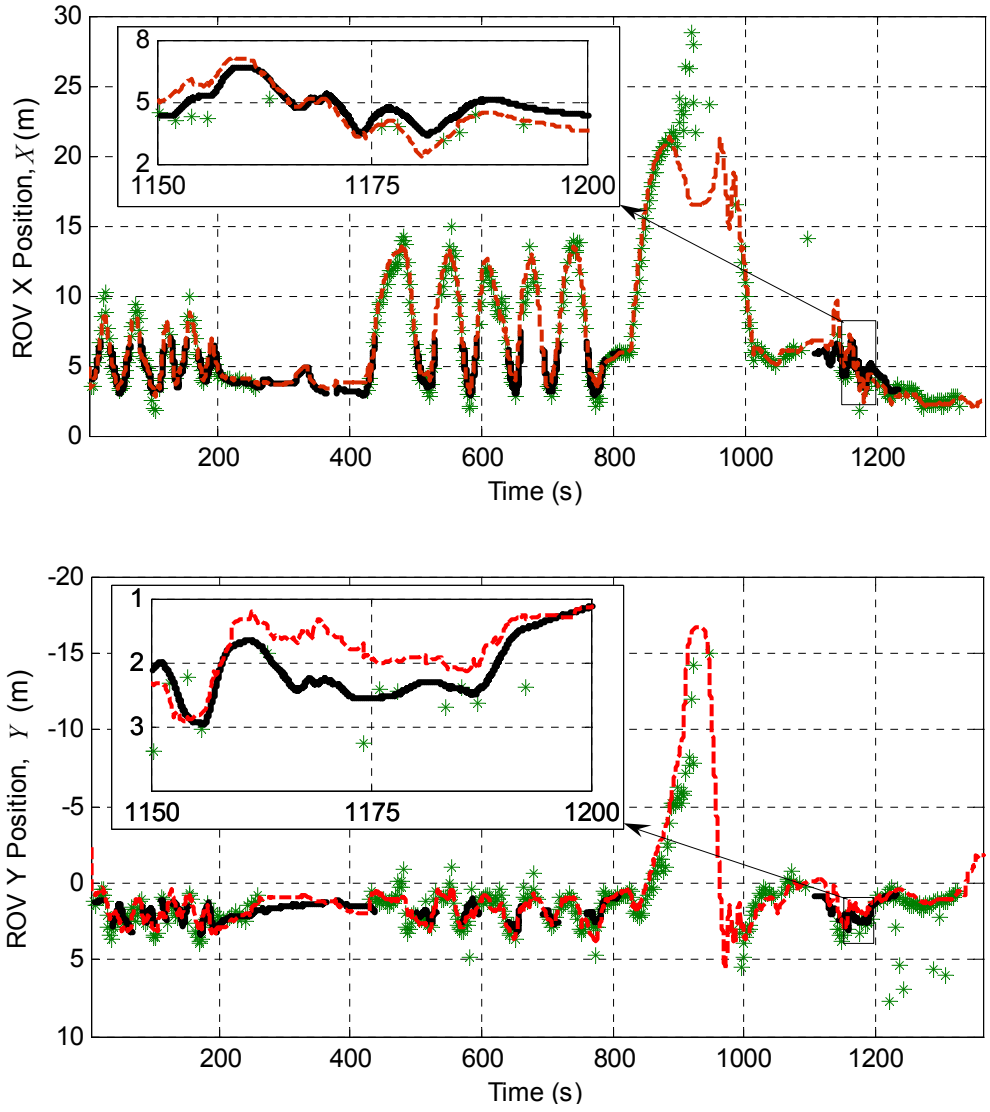

Figure 5-2. ROV Position during the Shallow Water Test. ROV horizontal position tracked with optical measurements (dark broken line), EKF estimation (dashed line), and SBL measurements (stars). The optical measurements were most accurate, but only available when the ROV mast was within the optical cameras' field of view. The EKF estimate used the same range measurements as the SBL algorithm, but also integrated velocity and orientation estimates to provide enhanced measurement accuracy.

The optical measurements were most accurate and used as a reference to calculate errors in the EKF estimate and the SBL measurements. The ROV positions based on optical measurements were linearly interpolated to synchronise with the EKF time-steps

within 0.1s of valid optical measurements. The same optical measurements calculated the SBL target transducer location, and were linearly interpolated to synchronise with SBL position measurements that were within 0.1s of valid optical measurements. Figure 5-3 shows the errors in the EKF X position estimate and the SBL X position measurements during the near surface test manoeuvre. Table 5-1 lists the RMS errors of the SBL measurements and the EKF estimates of both the X and Y positions.

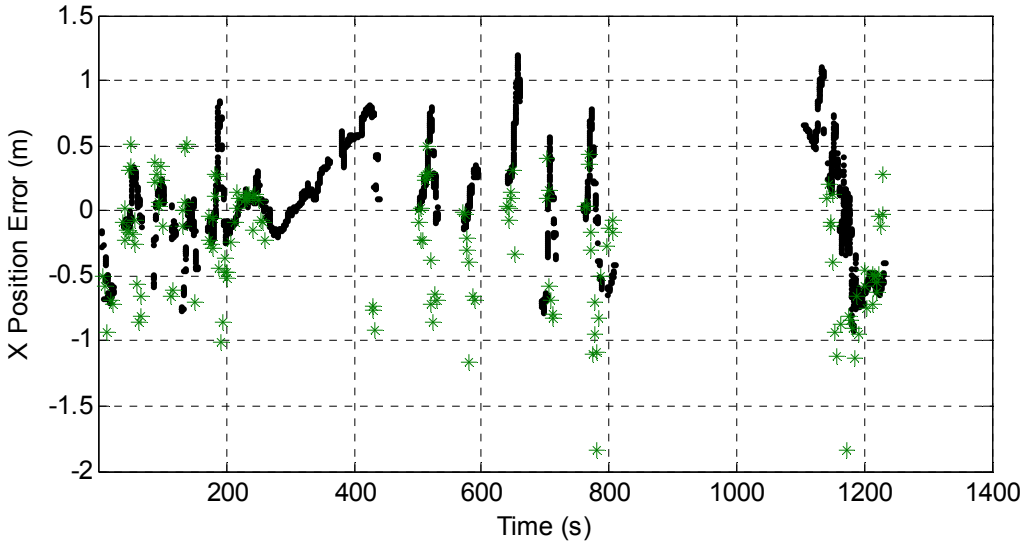

Figure 5-3. Shallow Water Position Error. X Position difference between optical position measurements and EKF estimate (dots appearing as broken lines) and SBL measurements (stars).

Coordinate	SBL RMS Error	EKF Position RMS Error
X	0.54 (2.2) m	0.42 m
Y	0.82 (0.9) m	0.52 m

Table 5-1. RMS Error of Position Estimates during the Near Surface Test Manoeuvre. Bracketed quantities are the variance that would have occurred if resampled to match the EKF rate.

The perils of underwater positioning were reduced with the EKF. The EKF position estimate was slightly more accurate and at a much higher rate than the standalone SBL

measurements. The SBL measurements were observed to drop out (such as between 260s and 420s) when the acoustic signal did not properly transmit, possibly due to excessive ambient noise, surfaced transducers, hardware error, or blockage of transmission path. Even when no acoustic measurements were available, the EKF accurately estimated the ROV position.

5.3 ROV Depth Estimation

The Falcon™ onboard depth sensor tracked the ROV depth with reasonable accuracy at nearly the same frequency as the EKF. However, the EKF estimate was more accurate than the sensor measurements. The estimated depth of the ROV during the near surface test manoeuvre is shown in Figure 5-4. The sensor's coarse 0.1 meter resolution and inclusion of the of DVL measured heave rate in the EKF contributed to the filter having the more accurate depth readings as shown in Table 5-2.

Coordinate	State	Depth Sensor RMS Error	EKF Depth RMS Error
Depth	Z	0.13m	0.086m

Table 5-2. RMS Error of Falcon™ Depth Sensor and the EKF Estimated Depth

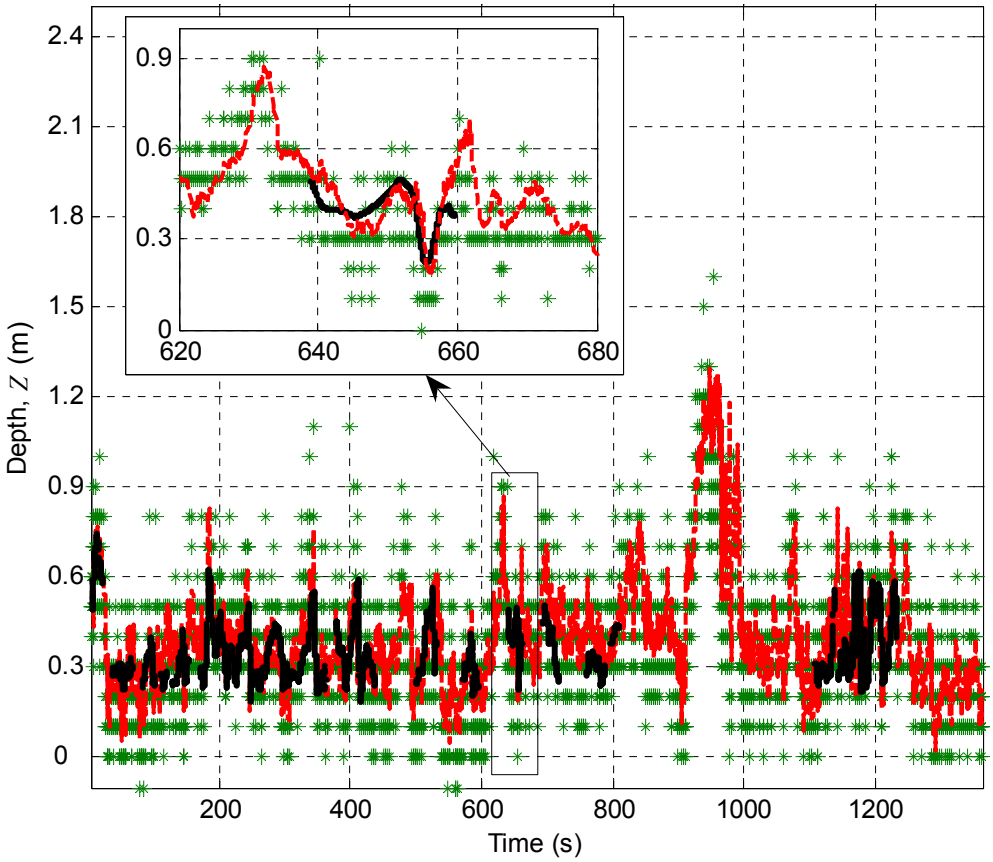

Figure 5-4. ROV Depth during the Near Surface Test. Depth was measured by the onboard depth sensor (star), estimated by the EKF (dashed line), and accurately tracked with optical measurements (broken line). Notice the 0.1m resolution of the depth sensor.

5.4 Tether Disturbance Estimation

Since no force transducer was available to measure the pull of the tether on the ROV, the absolute tether disturbance was not known. However, the tether was held slack throughout the near surface test manoeuvre, so the tether disturbance was assumed to be zero. The EKF estimate of tether disturbance is shown in Figure 5-5.

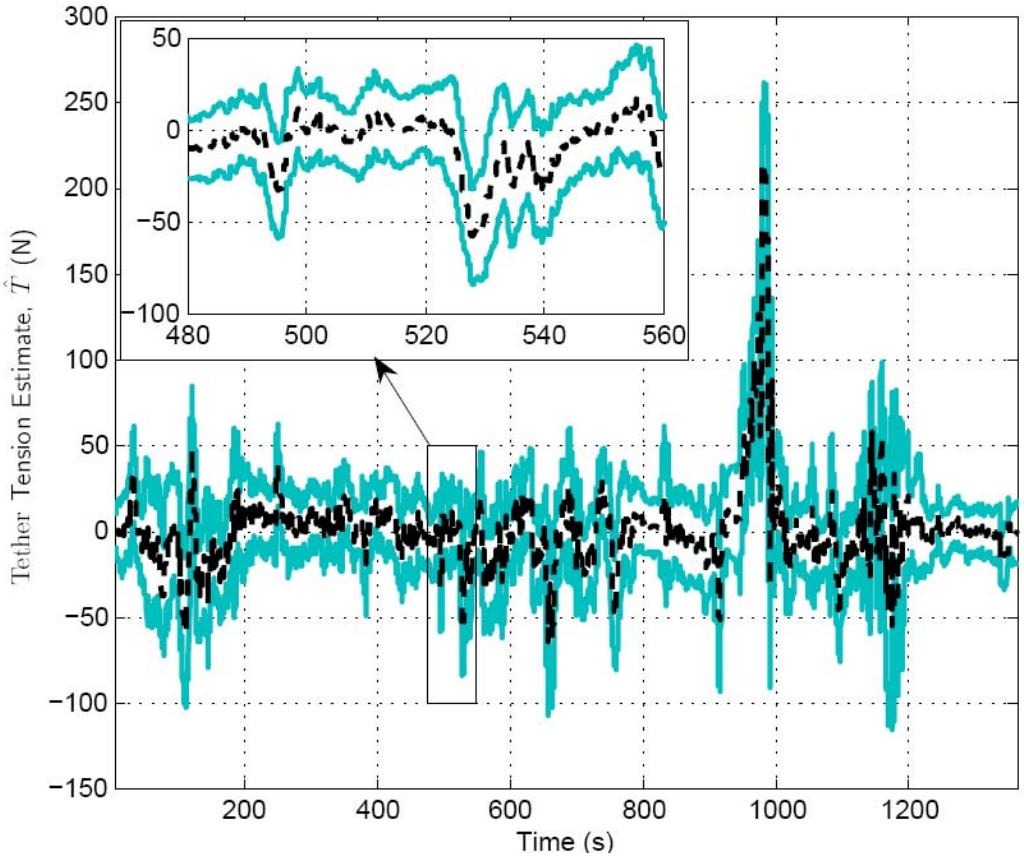

Figure 5-5. Tracking the Tether Tension. The EKF estimate of the tether tension (dashed line) is shown with one standard deviation confidence bounds (solid line). Notice the mean component of tether disturbance over a 10s time window was near zero, as expected because the tether remained slack in this test. The large estimates of tension (at 530s for example) occur during rapid manoeuvring when modeling error and measurement errors are large. The extreme spike in the estimate at 1000s was likely caused by an unmodeled external force, such as a collision.

The estimated tether disturbance remained less than 220N throughout the near surface test manoeuvre. Spikes in tether disturbance exceeding 50N were unlikely to occur with the test conditions, so the spikes larger than 50N were attributed to model mismatch with the true ROV dynamics. This mismatch could be attributed to coupling of hydrodynamic terms between DOFs, external forcing such as surface waves, and velocity dependence of the thruster forcing, which were emulated in the EKF model with the tether disturbance

term. The tether disturbance states were not included in the EKF to accurately detect the disturbance, but merely to approximate it in an effort to improve the kinetic model embedded in the filter.

5.5 DVL Contribution

The DVL is expensive and relatively large, making it difficult to justify in a budget and mount to the inspection class ROV. This section investigates the EKF performance without the aid of DVL measurements.

5.5.1 ROV Positioning without DVL

Figure 5-6 shows the same optical and acoustic position measurements as Figure 5-2, but now the EKF was not aided by the DVL measurements. The filtered estimate still accurately tracked ROV position during the acoustic positioning dropout at 250 seconds.

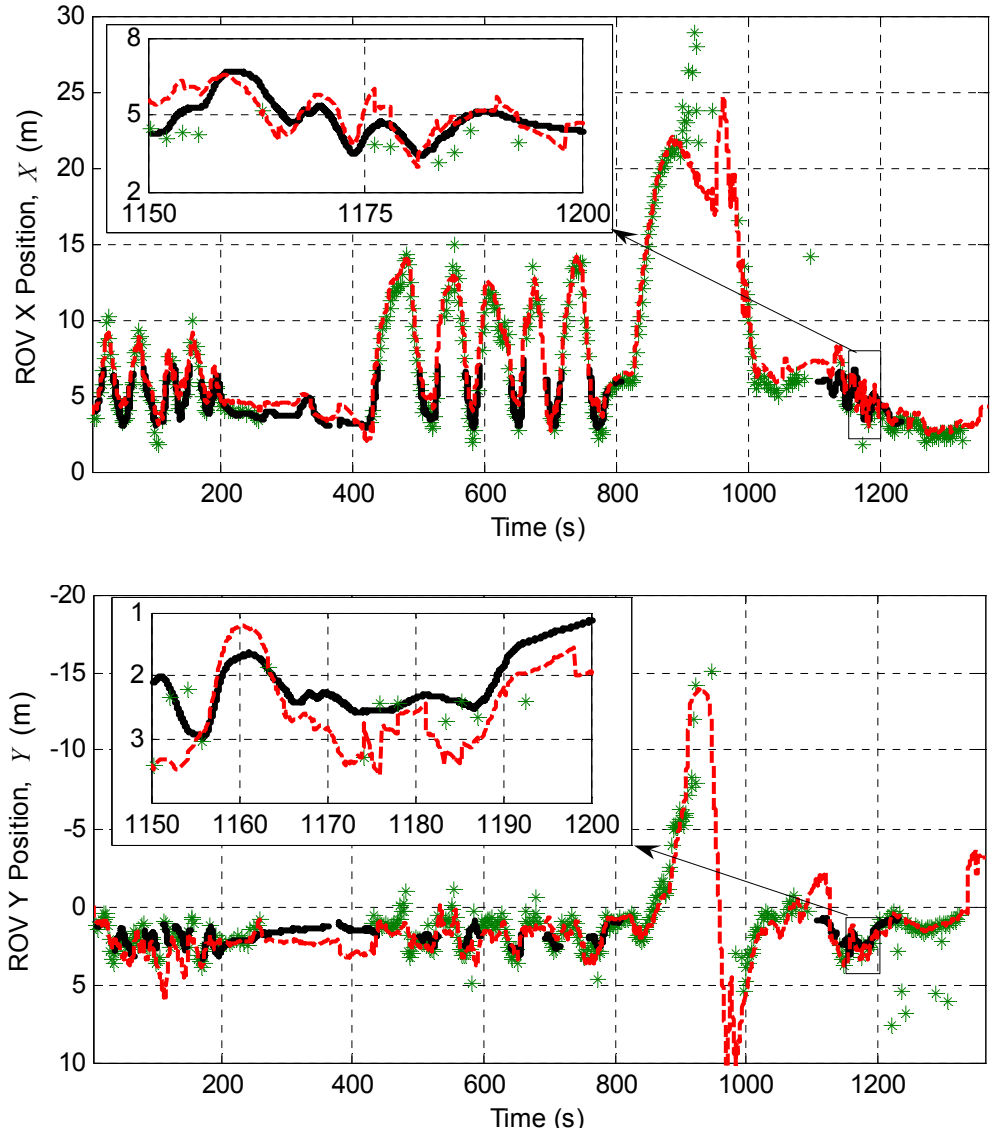

Figure 5-6. ROV Positioning without DVL. ROV horizontal position was tracked with optical measurements (broken line), EKF without DVL (dashed line), and SBL measurements (stars).

Table 5-3 lists the RMS errors of the SBL position measurements, the EKF position estimate aided by the DVL, and the EKF position estimate unaided by the DVL. Figure 5-7 shows the error time-series of each position tracking method.

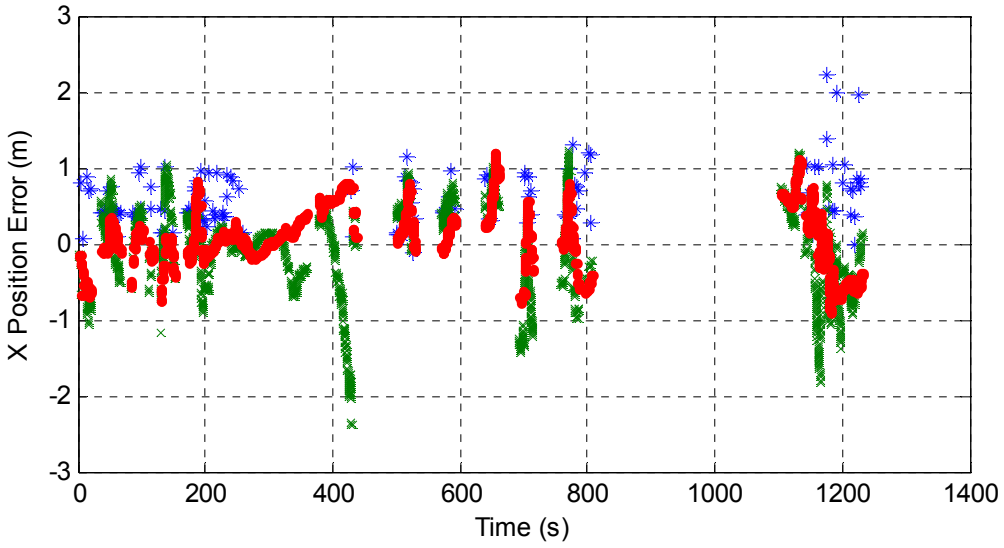

Figure 5-7. Position Tracking Errors for the full EKF (dot), the EKF un-aided by DVL (cross), and the SBL measurements (star).

Coordinate	Pilot RMS Error	Full EKF Position RMS Error	EKF w/o DVL RMS Error
X	0.54 (2.2) m	0.42 m	0.59 m
Y	0.82 (0.9) m	0.52 m	0.84 m

Table 5-3. Effect of DVL on Position Estimation Accuracy. Bracketed quantities are the variance that would have occurred if resampled to match the EKF rate.

Without the DVL measurements, the EKF estimate accuracy was degraded to below that of the stand alone SBL measurements. However, the filter was still able to provide greater tracking coverage than the SBL system. If the DVL is removed from the suite of navigation hardware, it is recommended that the position model uncertainty be re-identified using the method described in Subsection 4.4.4.

5.5.2 Velocity Tracking without DVL

Without the DVL, the EKF relied on the ROV kinetic model and the rate of change of the SBL position fixes to estimate the ROV velocity. Figure 5-8 shows the ROV surge velocity tracked by the DVL, the full EKF, and the EKF unaided by the DVL.

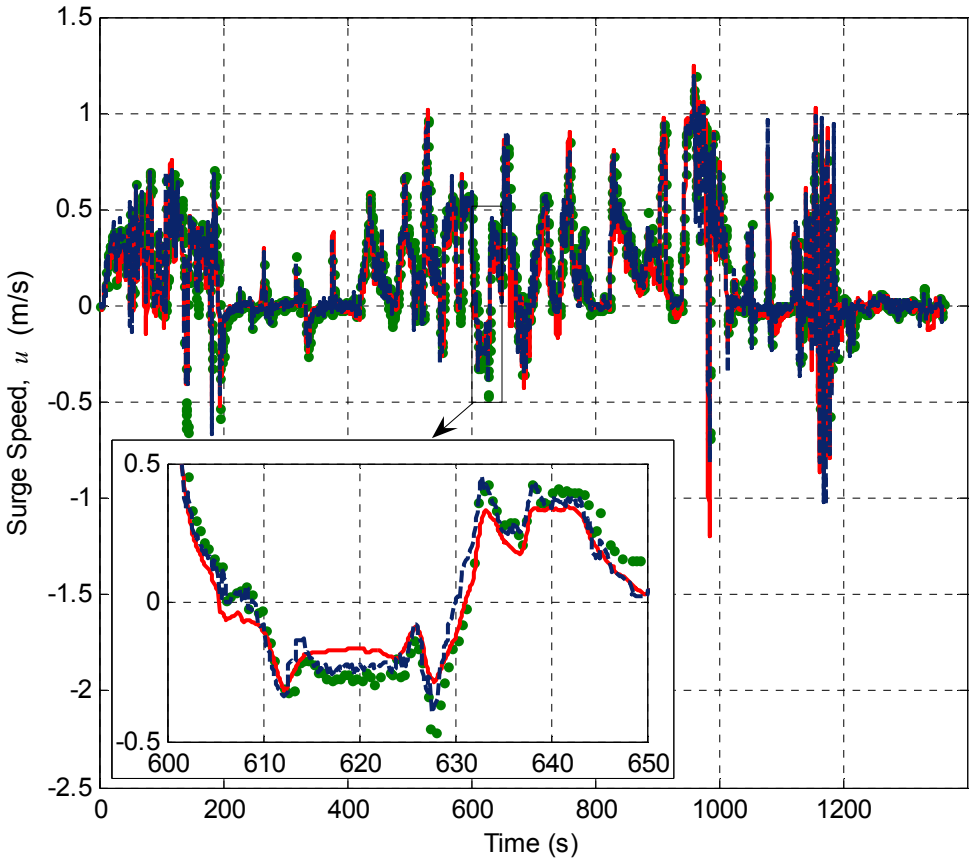

Figure 5-8. Surge Velocity Estimated by the EKF Unaided by DVL Measurements (solid line) compared with the full EKF (dotted line) and DVL measurements (dots).

Measurements of ROV velocity significantly more accurate than the EKF estimates and DVL measurements were not available for the near surface test manoeuvre. The RMS errors of the DVL measurements were calculated by assuming the error variances and biases measured during the stationary test presented in 4.2.3 were representative of all DVL measurements. The velocity estimate of the EKF aided by the DVL was expected to be at least as accurate as the DVL measurements. Accuracy of the velocity estimate of the EKF unaided by the DVL was calculated using the aided EKF as a reference. Table 5-4 lists the estimates of DVL measurement error and the unaided EKF velocity error.

Coordinate	State	DVL Uncertainty (Estimated RMS Error)	No DVL Velocity RMS Error
Surge	*u*	6.3 $x10^{-3}$ m/s	7.5$x10^{-3}$ m/s
Sway	*v*	8.9 $x10^{-3}$ m/s	8.3$x10^{-3}$ m/s
Heave	*w*	3.2 $x10^{-3}$ m/s	5.4$x10^{-3}$ m/s

Table 5-4. Velocity Tracking Accuracies. The DVL accuracy was measured with the stationary test presented in Subsection 4.2.3. Error in the EKF unaided by DVL measurements was calculated using the full EKF as a reference.

The RMS difference between the unaided EKF velocity estimate and the full EKF velocity estimate was on the order of the estimated DVL RMS errors. Therefore, the full EKF velocity estimate was not known to be significantly more accurate than the unaided EKF velocity estimate, and the RMS difference between the two only shows that the unaided EKF could estimate ROV velocity nearly as accurately as the DVL measurements.

5.6 Shallow Water Test Remarks

The EKF improved the accuracy of the position and orientation measurements. Furthermore, the filter provided position measurements at 10Hz, much more frequently than the SBL 0.5Hz measurements. Inclusion of the DVL measurements was found to be necessary for significantly improving the position tracking, even though the kinetic model enabled the EKF to estimate the ROV velocity with reasonable accuracy. Extrapolation of these near surface results to a full scale ocean manoeuvre is discussed in the next chapter.

Chapter 6. Simulated Deepwater Position Tracking

Most ROV operations occur at depths of 100m or more, beyond the safe working limits of human divers. While the shallow water test facility provided a unique opportunity to evaluate the navigation algorithm against the optical motion measurements, actual ROV operations experience longer SBL ranges and significant tether tensions due to the hydrodynamic forces that accumulate over the tether scope. The EKF performance at full ocean scale was evaluated using a numerical simulation that included the ROV, tether and instrument dynamics.

6.1 Deepwater Manoeuvre

ROV manoeuvres take on a variety of forms. Many missions, such as following a submerged pipe or documenting a biological monitoring transect, are along a straight line. Other objectives, such as finding a suitable attachment point for a recovery line, entail rapid turning and manoeuvring within a small area. To validate the proposed EKF at the ocean scale, a manoeuvre at 200m depth was simulated. In this manoeuvre the ROV starts with some rapid turns, proceeds to a 30m depth change, returns to its starting position before transiting to a waypoint 600m away, and finally holds its position. The waypoints of this manoeuvre are listed in Table 6-1, a plan view of the ROV path is

shown in Figure 6-1, and the tether profiles at notable times are shown in Figure 6-2. The simulated manoeuvre challenged the EKF to a level expected in typical deployments.

Time Started	Target Speed	Waypoint Location		
		X	Y	Z
0s	0.0m/s	0m	0m	200m
0s	1.5m/s	5m	5m	200m
13.1s	0.3m/s	-10m	10m	230m
99.4s	1.0m/s	0m	0m	240m
148.9s	1.0m/s	0m	0m	200m
246.3s	5.0m/s	600m	0m	200m
1080.7s	0.0m/s	600m	0m	200m

Table 6-1. Waypoints for the Simulated Manoeuvre.

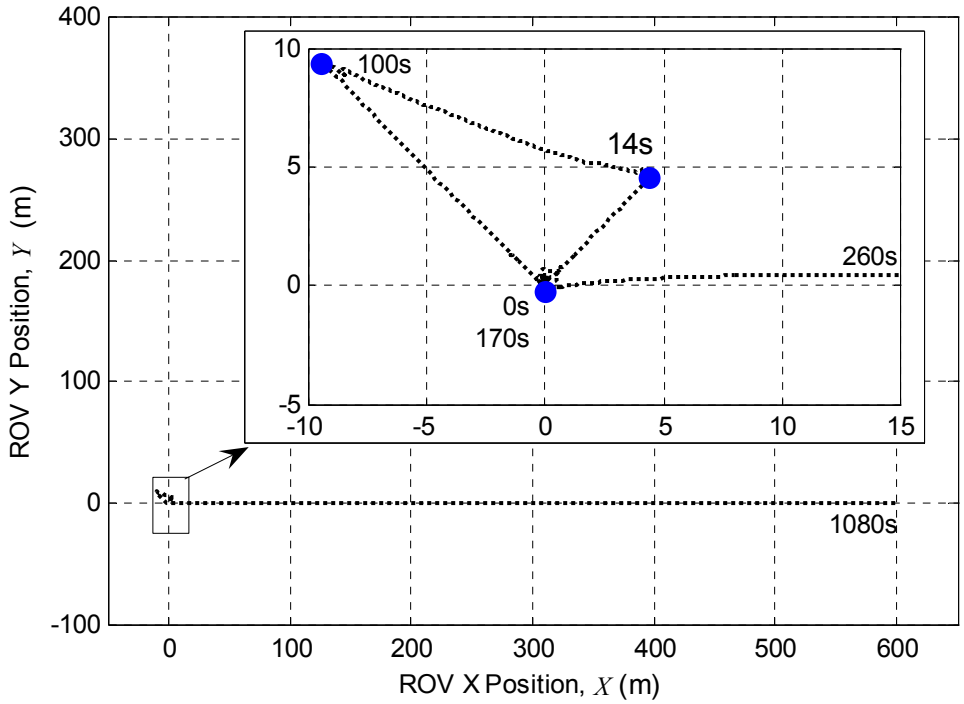

Figure 6-1. Plan View of ROV Position during the Deepwater Manoeuvre. The ROV starts at the origin, proceeds in the Y direction, returns to the origin, and finally proceeds in the X direction.

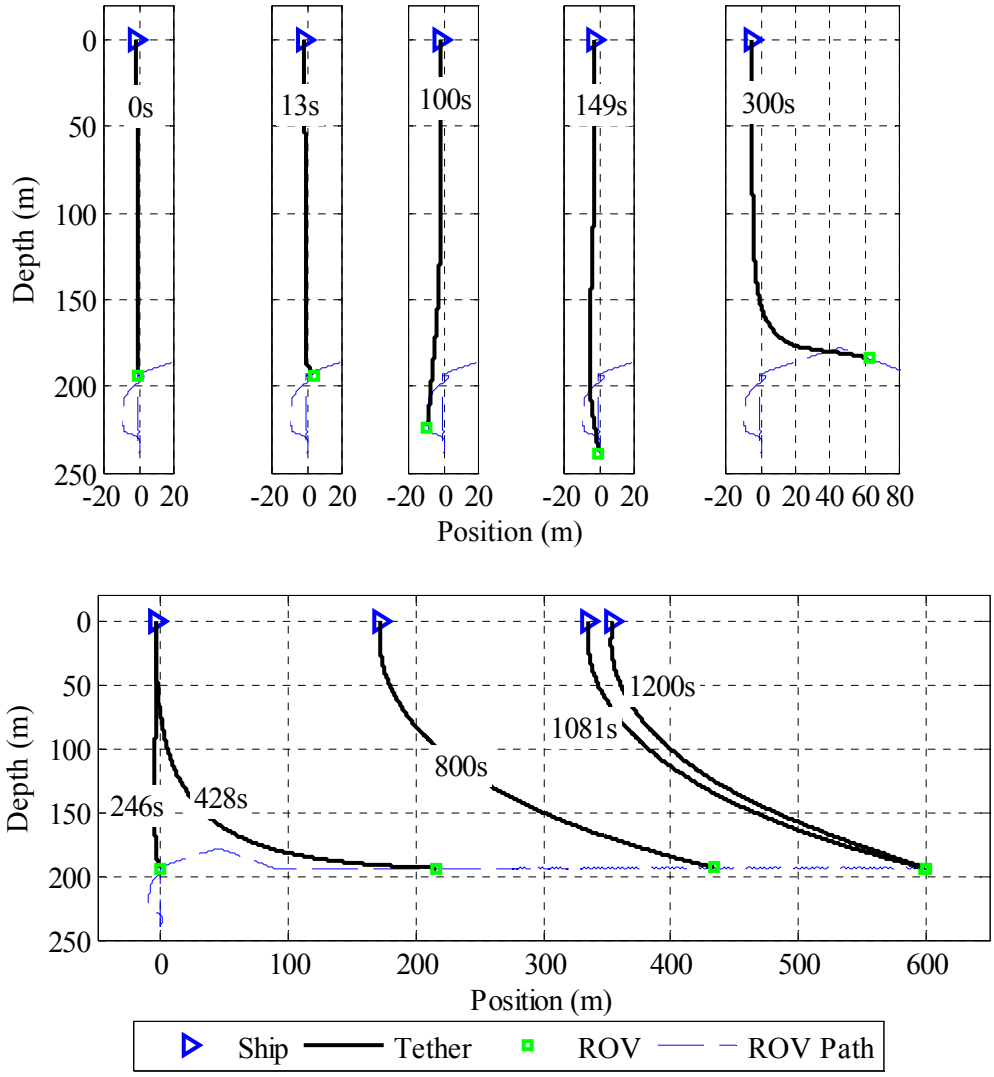

Figure 6-2. Tether Profiles During the Simulated Manoeuvre. 0s: ROV starts from rest. 149s: ROV at maximum manoeuvre depth of 240m. 246s: ROV starts transit. 428s: All 350m of tether is deployed. 1081s: ROV reaches waypoint and stops. 1200s: ROV holds position while ship approaches overhead.

6.2 Simulation Parameters

Provided the system dynamics were modelled accurately, the numerical simulation provided a controlled deepwater environment in which to evaluate the EKF. The deepwater manoeuvre was simulated with the conventional tether management scheme.

The tether properties remained the same as those used in the numerical simulations for the tether management development presented in Chapter 2.

With the exception of a more accurate tether disturbance model, the simulation's ROV model of the surge, sway, and heave DOF matched the translational model employed in the EKF. To mimic the uncertainty evident in the parameter identification process of Section 4.3, the ROV dynamic parameters used in the simulation were perturbed from the parameters values used in the EKF by the estimated standard deviation of each parameter. Table 6-2 lists the parameter values used in the EKF and the values used in the simulation that generated the deepwater test manoeuvre. These standard deviations were calculated by applying the regression method presented in Appendix A to the motion data collected with the shallow water tests.

Parameter	Symbol	Best Estimate Kalman Model	Perturbed Estimate Simulation Model
Surge Hydrodynamic Drag	D_u	88.9 N/(m/s)	109.2 N/(m/s)
	D_{uu}	183.75 N/(m/s)^2	169.5 N/(m/s)^2
Sway Hydrodynamic Drag	D_v	86.5 N/(m/s)	123.9 N/(m/s)
	D_{vv}	541.9 5 N/(m/s)^2	493.1 N/(m/s)^2
Heave Hydrodynamic Drag	D_w	173.2 N/(m/s)	225.9 N/(m/s)
	D_{ww}	230.25 N/(m/s)^2	140.7 N/(m/s)^2
Surge Inertia	m_u	281.0 kg	291.5 kg
Sway Inertia	m_v	223.8 kg	246.1 kg
Heave Inertia	m_w	509.6 kg	529.6 kg

Table 6-2. Simulation Parameters. The least squares fits of the parameter identification data were used for the kinetic model embedded in the EKF, so the parameters used for the simulation model were perturbed by one standard deviation.

6.3 Instrument Simulation

The deepwater simulation results for ROV position, orientation, and velocity, along with ship position, were sampled to generate sensor measurements. Random noise with a Gaussian distribution was added to the exact simulated values. The following subsections discuss how deepwater operation was expected to alter the measurement noise of each sensor from the shallow water operations where the noise properties were measured.

6.3.1 IMU Measurements

The IMU is a sealed unit which, aside from power and communication lines, does not interact with the local environment. The rate gyroscopes, accelerometers, and digitization hardware are sensitive to changes in temperature, but a thermocouple and pre-calibration mitigate temperature effects on the measurements. The IMU is expected to retain its shallow water noise variance and bias since its method of measurement is the same for deepwater operation.

6.3.2 Compass Measurements

The fluxgate magnetic compasses also have no physical contact with the surrounding ocean environment. They are sensitive to magnetic field disturbances, such as nearby thruster operation, or large steel vessels. Once the ROV is near the seafloor, away from external hard-iron sources, the compass is expected to operate as in the shallow water test facility, so its noise characteristics were retained.

6.3.3 Depth Sensor Measurements

The Falcon™ depth sensor measures the ambient water pressure to calculate depth in the range of 0m to 300m. The depth sensor was assumed to retain its noise variance, but

a 0.2m bias was added to the simulated measurements to account for errors in water density calibration. This bias is equivalent to a $1kg/m^3$ error in water density accumulated over the 200m nominal depth of the manoeuvre.

6.3.4 DVL Measurements

The DVL was also expected to retain its noise characteristics, as most operations are near the seafloor at altitudes less than those in the shallow water test. The 0.4s delay observed in the shallow water DVL measurements was also introduced in the simulated DVL measurements.

Often debris suspended in the water limit the visibility of the video camera to several meters or less. This requires the ROV to be within 1m of the seafloor to maintain site of it. The DVL only provides velocity measurements at altitudes between 0.5m and 65m. When the ROV is operating outside of this range, such as near the surface over deepwater or near the seafloor in poor visibility conditions, DVL measurements won't be available. Momentary DVL dropout was not directly simulated in this work, but the EKF was verified to function both with and without the DVL measurements.

6.3.5 SBL Range Measurements

The ranges reported by the SBL system were based on time of flight, with constant pulse frequency, so the error accrued in the SBL slant range measurements was not expected to vary significantly from those observed at the shallow water test facility. Signal amplitude would be lower for deepwater operations, so sensor dropout may occur more frequently. Sound speed may vary significantly between the ROV and the surface listening stations if a strong thermocline was present, which would cause additional error in range measurements. The reference stations' absolute locations, which were simulated

as mounted to a mobile vessel in deepwater ROV operations, would be less accurately known, stemming from errors in ship GPS and Motion Reference Unit (MRU) measurements.

6.3.6 SBL Reference Station Positioning

For ocean deployments, the SBL reference stations would be mounted to a surface vessel. The vessel position and orientation would be tracked with a GPS and MRU respectively. This work simulated operation from a 20m vessel with two reference stations on the corners of the transom, and one on the bow. Reference station locations in ship fixed coordinates are listed in Table 6-3

Reference Station	Coordinate	Symbol	Value
Port Aft	Forward	$x_{ref\,1}$	0.0 m
	Athwartships	$y_{ref\,1}$	-3.0 m
	Depth	$z_{ref\,1}$	0.5 m
Starboard Aft	Forward	$x_{ref\,2}$	0.0 m
	Athwartships	$y_{ref\,2}$	3.0 m
	Depth	$z_{ref\,2}$	0.5 m
Bow	Forward	$x_{ref\,3}$	20.0 m
	Athwartships	$y_{ref\,3}$	0.0 m
	Depth	$z_{ref\,3}$	0.5 m

Table 6-3. Ship Mounted Reference Station Locations. These locations were converted to an earth-fixed coordinate system using GPS and MRU measurements.

As listed in Table 6-4, white noise was added to the SBL reference station locations with a 1.5m standard deviation (based on Kongsberg Seapath™ 100 specifications) to model uncertainty in the GPS measurements. Furthermore, the MRU's orientation measurement error was assumed to contribute little to the reference station position error.

Moreover, since the SBL position measurements were all relative to the ship, any bias in ship position would directly transfer to bias in estimated ROV position.

Quantity	Symbol	Variance
Ship Position Measurement Noise	σ^2_{X-Ship} , σ^2_{Y-Ship}	2.25 m^2

Table 6-4. Ship Position Tracking Error Variance - estimated from GPS specifications, added to all three reference station locations.

6.3.7 Acoustic Position Tracking

For comparison purposes, the SBL measured ROV location was also simulated. The estimated SBL measurements were calculated by finding the non-linear least-squares fit to the ROV position based on the same simulated range measurements from each of the three reference transducers used by the EKF. The acoustically transmitted SBL depth measurements were also simulated and included in the SBL calculated positions.

6.4 EKF Modifications for Deepwater Applications

Unlike the stationary reference station configuration used in the shallow water test facility, the deepwater manoeuvre simulated reference stations attached to a moving ship hull. Reference station locations were calculated based on the ship's GPS and MRU measurements. The reference station position noise necessitated an increase in the variance parameter R_{SBL} to reflect the larger uncertainty in H_{SBL}. Range is a non-linear function of ship position. For small differences between the true reference station location $(X_{ref}, Y_{ref}, Z_{ref})$ and the estimated reference station location $(\hat{X}_{ref}, \hat{Y}_{ref}, \hat{Z}_{ref})$, a linearized range calculation suitably approximates the length of the displacement vector:

$$r \cong r_0 + (\hat{X}_{ref} - X_{ref})\frac{X_{ref} - X_{tar}}{r_0} + (\hat{Y}_{ref} - Y_{ref})\frac{Y_{ref} - Y_{tar}}{r_0} + (\hat{Z}_{ref} - Z_{ref})\frac{Z_{ref} - Z_{tar}}{r_0} \qquad (6.1)$$

In Equation (6.1), r denotes the range from the estimated reference station location to the target transducer location $(X_{tar}, Y_{tar}, Z_{tar})$, and r_0 denotes the range from the true reference station location to the target transducer location. The ship position error was expected to be much smaller than the ROV range to each reference station, so Equation (6.1) was applied to estimate the influence of ship position error on the range measurements. The corrected range error variance estimate, denoted σ_r^2, is the sum of the variance of errors in the acoustically measured range, denoted $\sigma_{r_0}^2$, and the error variance caused by uncertain reference station locations:

$$\sigma_r^2 = \sigma_{r_0}^2 + \frac{(X_{Ship} - X_{tar})^2}{r^2}\sigma_{X-Ship}^2 + \frac{(Y_{Ship} - Y_{tar})^2}{r^2}\sigma_{Y-Ship}^2 \tag{6.2}$$

The EKF adjusted to account for the increased range noise was employed to process the deepwater manoeuvre measurements simulated according to the method described in Section 6.3. The EKF estimates are compared to the true simulation states in the next section.

6.5 Deepwater Filter Performance Evaluation

The EKF estimates were compared against the true state values of the simulated deepwater manoeuvre. The importance of the DVL is again investigated by comparing the EKF performance with and without the DVL measurements. The RMS errors in the simulated measurements and the EKF estimates of ROV position and velocity are presented in the following subsections. The EKF estimate of tether disturbance is also compared to the tether disturbance calculated by the high fidelity numerical simulation.

6.5.1 Position Tracking

The accuracies of the EKF position estimate and of the simulated SBL measurements were quantified by comparison with the simulated position. Even though the acoustically measured range was modeled with constant accuracy, the longer acoustic slant ranges reduced the positioning accuracy. Table 6-5 lists the RMS position errors of the SBL, the fully aided EKF, and the EKF without DVL measurements.

Coordinate	SBL RMS Error	EKF RMS Error	EKF w/o DVL RMS Error
X	2.7 m	1.9 m	2.2 m
Y	17.2 m	3.5 m	9.2 m

Table 6-5. ROV Position Tracking Accuracy for the Deepwater Manoeuvre.

Both EKF estimates were more accurate than the SBL measurements. The EKF also provided position updates at 10Hz - much higher than the 0.5Hz nominal SBL rate.

The ROV X position was more accurately tracked than the Y position because the ship was aligned with X, and thus the SBL system's reference stations were spaced further along this direction. Were the ship to turn 90deg, the error proportions would be switched.

Figure 6-3 shows the ROV X Position during the deepwater manoeuvre, its estimate made by the SBL, and its estimate made by the EKF with and without the DVL measurements.

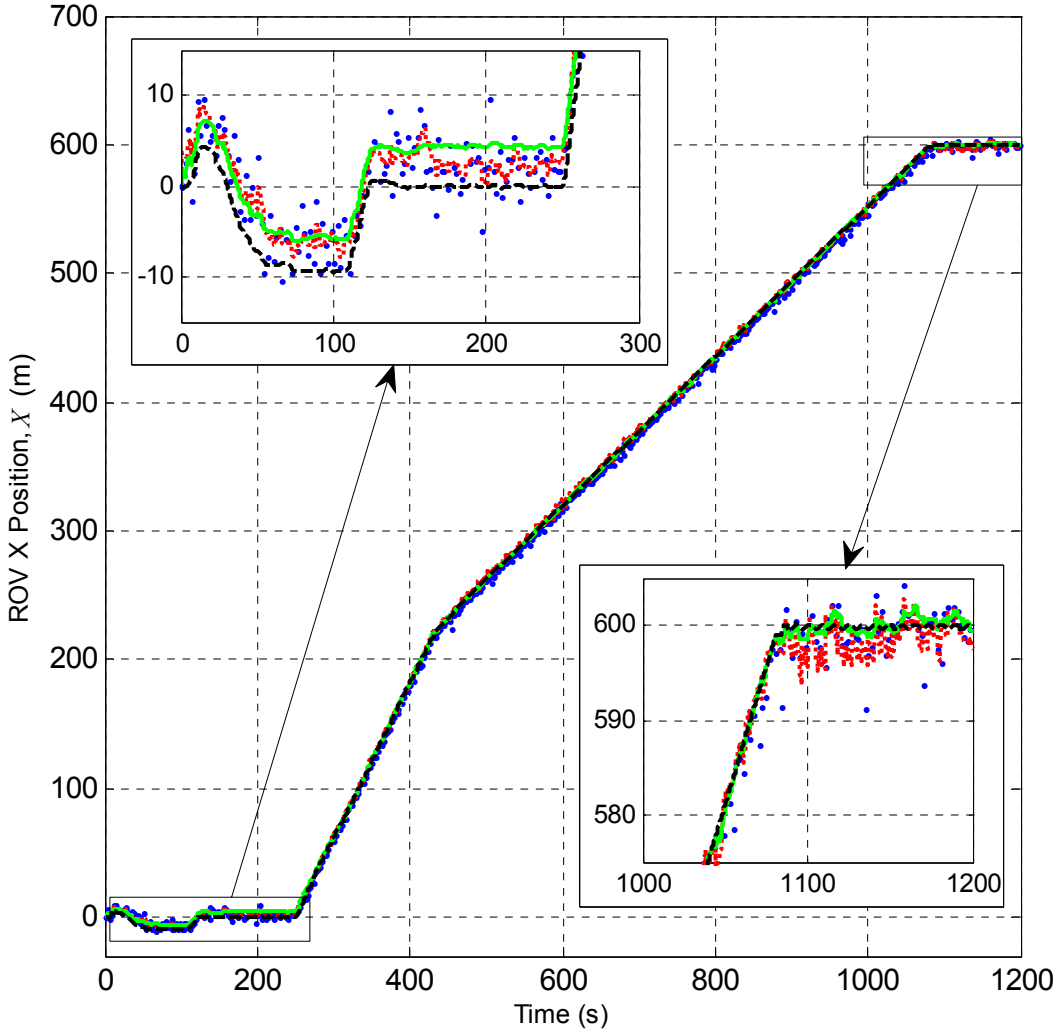

Figure 6-3. Simulated ROV X Position (dashed line) estimated with the complete EKF filter (solid line), EKF filter without DVL (dotted line), and SBL measurements (dots).

The EKF estimate was less accurate at the start of the manoeuvre, due to bias in the initial range measurements. At the end of the manoeuvre, the EKF closely tracked the ROV's true position.

Using the DVL measurements, the EKF placed more confidence in its velocity estimate and was less influenced by the noisy acoustic range measurements, providing smoother position estimates. Even without the DVL, the EKF kinetic model allowed quick response to velocity changes, such as the abrupt stop at the destination.

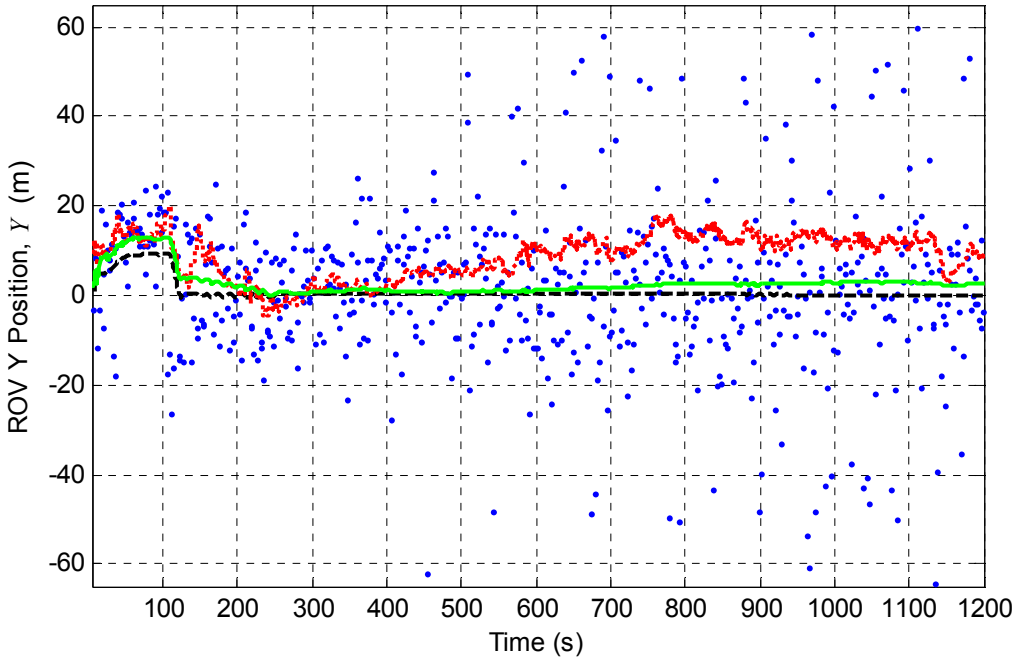

Figure 6-4. Simulated ROV Y Position (dashed line) estimated with the complete EKF filter (solid line), EKF filter without DVL (dotted line), and SBL measurements (dots).

Figure 6-4 shows the ROV Y Position during the deepwater manoeuvre. The SBL Y position error variance increased as the ROV moved further ahead of the ship. As the ROV moved horizontally away from the ship, the SBL position calculation increased reliance on the relative ranges measured by the reference transducers rather than than the more accurately measured target transducer depth.

The benefit of including the DVL in the EKF was more pronounced in the Y position estimate. The range measurements provide poor Y position resolution, so the improved velocity tracking provided by the DVL allowed the EKF to generate a smooth estimate.

6.5.2 Depth Tracking

The RMS errors in the simulated depth sensor measurements and the EKF depth estimates are shown in Table 6-6.

Coordinate	State	Depth Sensor RMS Error	EKF RMS Error	EKF w/o DVL RMS Error
Depth	Z	0.275 m	0.215 m	0.273 m

Table 6-6. Depth Tracking Accuracy during the Deepwater Manoeuvre.

Like in the shallow water tests, the full EKF estimate of depth was slightly better than the raw depth sensor measurements. Without the DVL, almost no accuracy improvement was obtained in using the EKF estimate over the raw depth measurements. Most of the error in all three sets of depth estimates was attributed to the 0.2 meter bias added to the simulated depth measurements.

6.5.3 ROV Velocity Tracking

The RMS error in the simulated DVL measurements and the EKF velocity measurements is shown in Table 6-7.

Direction	State	DVL measurements RMS Error	EKF RMS Error	EKF w/o DVL RMS Error
Surge	u	0.08 m/s	0.04 m/s	0.15 m/s
Sway	v	0.11 m/s	0.03 m/s	0.13 m/s
Heave	w	0.023 m/s	0.02 m/s	0.05 m/s

Table 6-7. Velocity Tracking Accuracy during the Deepwater Manoeuvre

Figure 6-5 shows the ROV surge velocity tracked by the DVL and the EKFs.

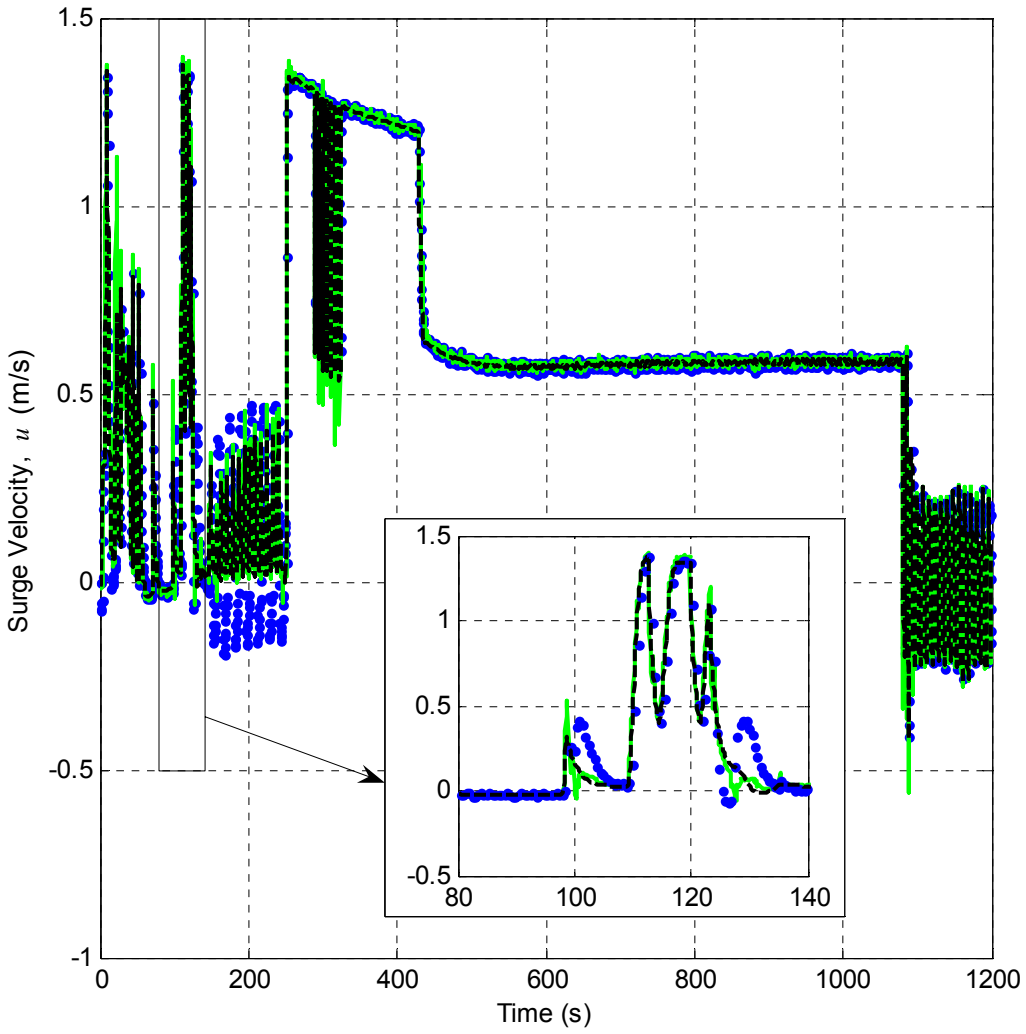

Figure 6-5. EKF Velocity Tracking Performance. The EKF estimate (solid line) of ROV surge velocity tracked the true velocity (dashed line) more accurately than the DVL measurements (dots) throughout the simulated manoeuvre. Notice the significant errors in the DVL measurements at 105s and 130s due to high ROV yaw rates.

The inclusion of the DVL offset from the ROV reference frame origin in the EKF allowed unbiased processing of the DVL measurements, even during rapid yawing activity.

6.5.4 Tether Disturbance Estimation

During the simulated manoeuvre, tension in the tether increased as the ROV accelerated forward. The tension plateaued at 428s when the entire tether was deployed, and returned to the controlled slack value once the ROV reached its final destination at 1081s. The EKF indirectly estimated the magnitude and direction of the tether disturbance. Figure 6-6 compares the EKF estimate of tether tension with the actual tension calculated with numerical simulation.

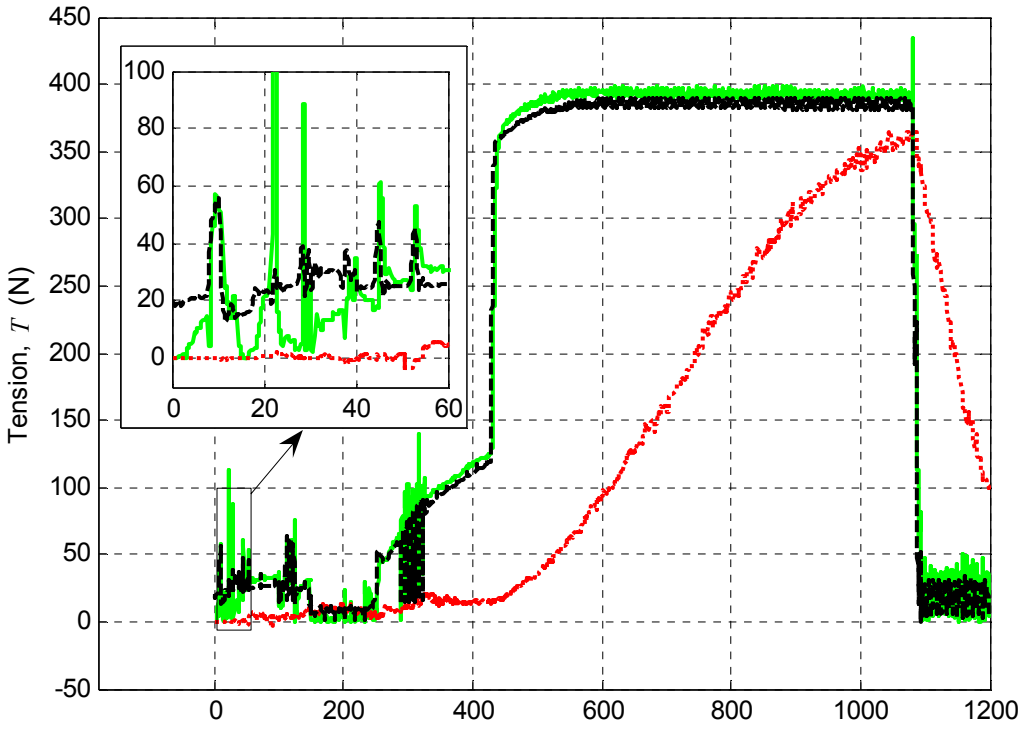

Figure 6-6. Tether Tension Estimation. The full EKF estimate of tether tension (solid line) closely tracked the actual tether tension (dashed), but without the DVL measurements, the EKF estimate exhibited slow response (dotted).

The DVL velocity measurements were used by the EKF to identify force imbalances in its kinetic model attributed to tether disturbance. Without these measurements, the EKF relied on SBL range measurements to correct the kinematic model. The high uncertainty

in ROV position calculated from range measurements slowed the EKF's response to changes in tether disturbance.

The ROV moved mostly in surge during the deepwater manoeuvre, so the tether tended to be towed out the aft end. Figure 6-7 shows the simulated tether bearing and the corresponding EKF estimate, α.

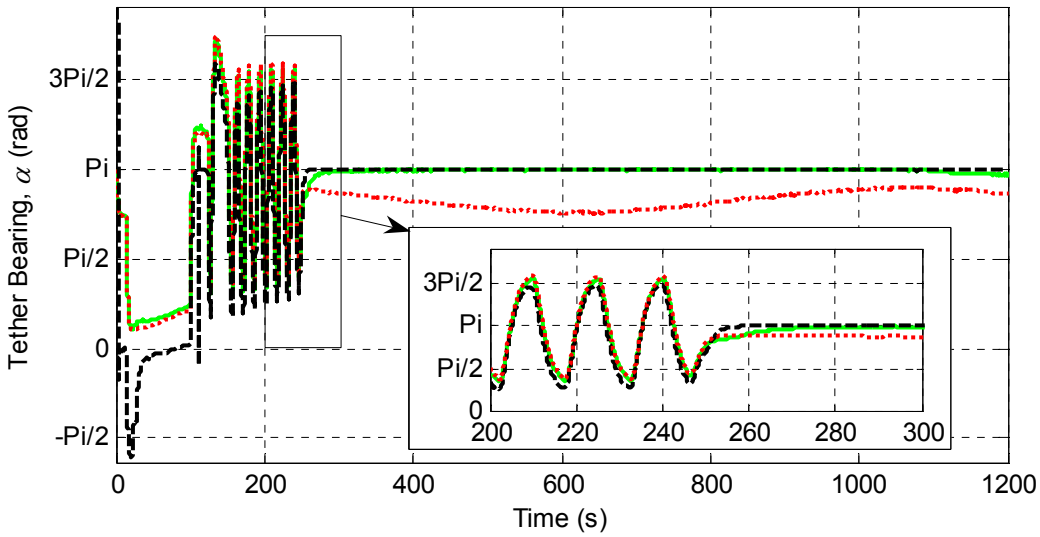

Figure 6-7. Tether Bearing Estimation. The EKF estimate (solid line) closely tracked the simulated (dashed line) tether bearing, α, except during the first 100s when the ROV performed lateral manoeuvres. Without the DVL measurements, the EKF estimate was degraded (dotted line).

The tether bearing was most accurately estimated by the full EKF when the tether tension was high. Apparent forcing caused by modelling inaccuracies, such as ocean currents and parameter estimation errors was also lumped into the tether disturbance estimate, so the actual tether disturbance was most accurately characterized by this estimate when it was large compared to the unmodeled forces.

Modeling the tether direction as constant in the earth-fixed reference frame closely matched the realized dynamics. Even when the ROV was rapidly yawing left and right from 150s to 250s, the tether bearing was accurately estimated by the EKF.

At the start of the manoeuvre, the tether left the ROV in a near vertical configuration as shown in Figure 6-2. When the transit manoeuvre started at 248s, the tether trailed out the aft end of the ROV, inclined slightly above horizontal. The estimated tether inclination, β, is compared to the simulation result in Figure 6-8.

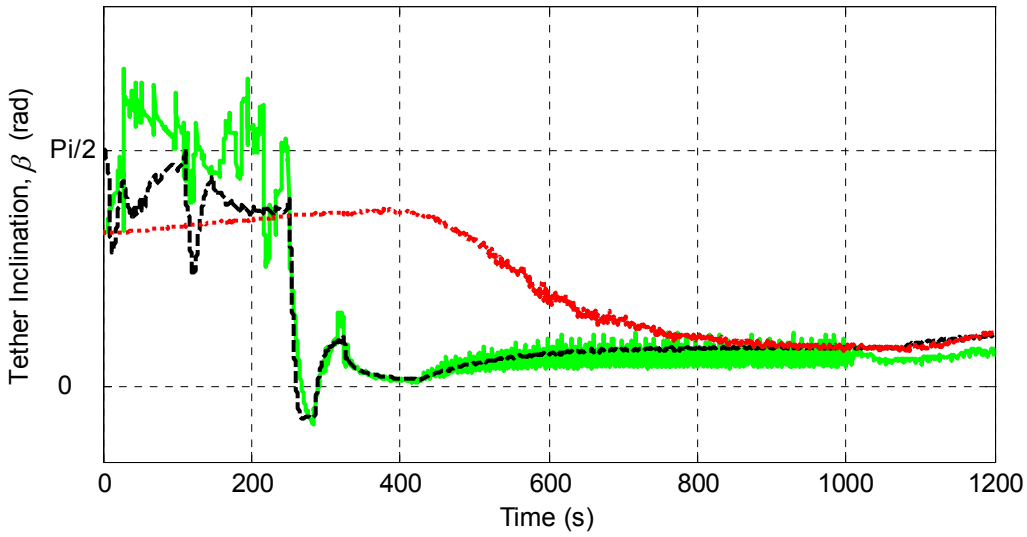

Figure 6-8. Tether Inclination Estimation. The full EKF (solid line) closely tracked the true simulated (dashed line) tether inclination, β. Without the DVL measurements, the EKF estimate exhibited slow dynamic response (dotted line).

The EKF estimate only roughly tracked the true tether inclination angle during the first 250s of the manoeuvre because unmodeled effects, such as heave-added mass error, were large compared to the tether tension. As with the tension estimate, without the DVL, the EKF did not have enough feedback to rapidly track changes in inclination angle.

The simulated manoeuvre assumed there was no ocean current. If the manoeuvre was performed in an ocean current, the added hydrodynamic drag on the ROV would bias the dynamics in a similar manner to tether disturbance. The EKF estimated tether disturbance would be tainted with the hydrodynamic disturbance. However, the main goal of accurately tracking the ROV position would still be obtained, as the unmodeled disturbances would be lumped into the tether disturbance states.

6.6 Deepwater Performance Remarks

When applied to the deepwater manoeuvres more likely to be performed with the Falcon™ ROV, the EKF retained the navigation accuracy improvements found in the shallow water tests. In moving to a ship based mounting configuration, the reference station spacing was found to impact the SBL measurement accuracy. SBL positioning RMS errors of 3m were calculated for the X direction and of 17m for the Y direction (which had a shorter baseline). The EKF provided more accurate position estimates with RMS errors of 1.9m and 3.5m in the X and Y directions, respectively. As with the shallow water manoeuvre, the DVL was found to contribute significantly to the EKF position estimate accuracy.

The EKF estimate of ROV velocity was more accurate than the raw DVL measurements because it removed the DVL measurement error caused by the instrument offset during rapid yawing. Even without the DVL, the EKF kinetic model allowed it to estimate the ROV velocity with accuracy nearly equal to that of the DVL measurements.

Chapter 7. Conclusions and Recommendations

7.1 Conclusions

Tether management schemes for the Falcon™ inspection class ROV were developed and tested with numerical simulation. A navigation suite, including instrumentation hardware, signal routing, and measurement filtering, was developed and installed on the Falcon™ and shown to provide position tracking superior to stand-alone SBL systems. The research objectives set in Section 1.4 have been completed with the results summarized in the following subsections.

7.1.1 Falcon™ ROV Parameters Identified.

The Falcon™ parameters with strong influence on the EKF model, namely the translational DOF hydrodynamic coefficients and the thruster mapping parameters were quantified with a series of shallow water tests. Tether material properties required for numerical simulation of the system were measured with mechanical tests.

7.1.2 Tether Management Schemes Developed

Driving the ship to lead the ROV was found to reduce tether disturbance for sustained manoeuvres. For long transects at 200m depth, a ship lead of 26m was found to produce the smallest tether disturbance. A demonstration transect manoeuvre which experienced

tether disturbances as high as 43N using conventional tether management was shown to experience only 20N of tether disturbance using an advanced tether management scheme. For transits at 200m, a ship lead of 90m was found to allow the highest sustained transit speed at slightly over 0.67m/s. Adding a depressor mass to the tether allowed transit speeds exceeding 1m/s. The tether management schemes were developed and tested on manoeuvres at 200m depth, but the same methodology is applicable to manoeuvres at other depths.

7.1.3 The EKF Developed

An EKF was designed and implemented on the Falcon™ ROV. The filter evolves position and velocity estimates using a kinetic translational model and kinematic rotational model of the ROV and refines the estimates with feedback from SBL, DVL, IMU, compass, and depth sensors. The Falcon™ thrust forces were tracked and provided as an input to the EKF kinetic translational model. The classical formulation of the KF was extended to account for nonlinearities in the ROV model and range measurement processing. The filter's measurement vector was also augmented to handle latency in the DVL and SBL measurements. Measurement noise was characterised and model uncertainty was quantified to determine the entries of the EKF process and measurement covariance matrices.

7.1.4 Identification of the Tether Disturbance Forces

Tether disturbance was modeled by the EKF as constant in the earth fixed frame. The EKF initialized and updated changes to the tether disturbance as mismatches between the model estimated forcing and the forcing that would create the system dynamics measured by the instruments, primarily the DVL.

Even without a load-cell for direct feedback, the EKF estimated tether disturbance with reasonable accuracy. No direct measure of tether disturbance was made during the shallow water test, but the EKF estimate of tether disturbance showed good correlation with simulated tether disturbance during the deepwater manoeuvre. Of all the sensors used in the EKF, the DVL provided the most useful feedback for resolving tether disturbance. Without the DVL, the tether disturbance estimate was slow to respond to changes in actual tether disturbance.

7.1.5 Experimental Testing of the Navigation System

The EKF performance was analysed with actual measurements taken during the shallow water test. Comparison with the highly accurate and high frequency optical position measurements allowed quantitative analysis of the EKF position estimate accuracy. The RMS errors of the EKF position estimate for the shallow water test manoeuvre were over 20% less than the SBL measurement errors and updated at constant time intervals at 10Hz. The DVL was an important contributor to the increased accuracy, and excluding its measurements from the EKF significantly increased the estimate errors. Table 7-1 summarizes the shallow water position tracking accuracy.

State	Symbol	Instrument RMS Error	EKF RMS Error	EKF w/o DVL RMS Error
X Position	X	0.54m	0.42m	0.59m
Y Position	Y	0.82m	0.52m	0.84m
Depth	Z	0.13m	0.09m	-

Table 7-1. Summary of Shallow Water Navigation Accuracy.

Numerical simulation was used to extend the shallow water results to the deepwater manoeuvres more commonly performed with the Falcon™ ROV. The increased slant ranges degraded the SBL positioning accuracy, but the EKF provided position estimates

with RMS errors less than 4m. Simulation results were also used to evaluate the accuracy of the velocity and tether disturbance states. Again, the estimated errors increased when the DVL was excluded from the EKF. Table 7-2 summarizes the deepwater position and velocity tracking accuracies.

State	Symbol	Instrument RMS Error	EKF RMS Error	EKF w/o DVL RMS Error
X Position	X	2.7 m	1.9 m	2.2 m
Y Position	Y	17.2 m	3.5 m	9.2 m
Depth	Z	0.275 m	0.215 m	0.273 m
Surge Speed	U	0.08 m/s	0.04 m/s	0.15 m/s
Sway Speed	V	0.11 m/s	0.03 m/s	0.13 m/s
Heave Speed	W	0.023 m/s	0.02 m/s	0.05 m/s

Table 7-2. Summary of the Simulated Deepwater Navigation Accuracy

7.2 Future Work

Tether management and underwater navigation are continuously developing fields of ROV operation. This work contributes to both fields, but more challenges remain to be overcome. Several areas for future research to extend the results of this work are listed in the following subsections.

7.2.1 Tether Disturbance Mapping

This work mapped tether disturbance over ship lead and steady-state transit speed for a 350m tether reaching to 200m depth. The dependence of tether scope and ROV depth on tether disturbance is needed to quickly extend the tether management schemes to all possible operating depths. For steady-state transit mapping, many relationships can be made by shape similarities. For instance, tether disturbance increases linearly with depth for configurations with the same scope to depth ratio.

7.2.2 Model Based Ship Dynamic Positioning

The performance of the PID controllers presented for depressor positioning [21] is challenged by the depressor depth sensitivity to ship motion and the lack of actuation to enact rapid horizontal acceleration. A controller embedded with a cable model such as in [18] may produce better schedules of ship position and winch activity to achieve desired depressor positioning. However, depressor position and velocity feedback will still be necessary to correct controller activity for the inaccuracies that are inevitable in models of flexible tethers.

7.2.3 ROV Collision Detection

All ROV models used in this work fail to capture the contact forces resulting from ROV collisions with the seafloor and other objects. A KF model is unlikely to have sufficient knowledge of objects surrounding the ROV to detect, let alone model collisions. However, the IMU acceleration measurements, thought to be too noisy to be of use for translational navigation, may provide clear indication of a collision by sensing the impact acceleration. Should a collision be detected, the estimated error variance of the kinetic model could be increased to account for the unmodeled contact forces.

7.2.4 Enhanced Tether Disturbance Estimation

The IMU's rate gyroscopes provide measurements with such accuracy and frequency that a kinetic rotational model was deemed unnecessary for the EKF used in this work. However, while a kinetic model is unlikely to improve ROV rotational rate estimation, it would improve tether disturbance estimation. The torque caused by tether disturbance could be inferred from imbalance between the model calculated rotational rates and the IMU measured rotational rates

Bibliography

[1] P. J. Beaujean, "High-speed high-frequency acoustic modem for image transmission in very shallow waters," in *Proc. OCEANS 2007*, IEEE, 2007.

[2] S. Wood, T. Allen, S. Kuhn, and J. Caldwell, "The development of an autonomous underwater powered glider for deep-sea biological, chemical and physical oceanography," in *Proc. OCEANS 2007*, IEEE, 2007.

[3] J. Refsnes, A. J. Sorensen, and K. Y. Pettersen, "Output feedback control of an auv with experimental results," in *Proc. 2007 Mediterranean Conference on Control and Automation*, IEEE, 2007.

[4] C. Silvestre and A. Pascoal, "Control of the infante auv using gain scheduled static output feedback," *Journal of Control Engineering Practice*, vol. 12, pp. 1501–1509, 2004.

[5] L. Rodrigues, P. Tavares, and M. Prado, "Sliding mode control of an auv in the diving and steering planes," in *Proc. OCEANS 1996*, vol. 2, pp. 576–583, IEEE, 1996.

[6] D. Kruger, R. Stolkin, A. Blum, and J. Briganti, "Optimal auv path planning for extended missions in complex, fast-flowing estuarine environments," in *Proc. International Conference on Robotics and Automation*, IEEE, 2007.

[7] P. Hagen, "Auv/uuv mission planning and real time control with the hugin operator system," in *Proc. OCEANS 2001*, vol. 1, pp. 468–473, IEEE, 2001.

[8] N. Palomeras, M. Carreras, P. Ridao, and E. Hernandez, "Mission control system for dam inspection with an auv," in *Proc. International Conference on Intelligent Robots and Systems*, pp. 2551–2556, IEEE, 2006.

[9] M. Narimani and M. Narimani, “Design of adaptive-sliding mode controller for positioning control of underwater robotics,” in *Proc. Canadian Conference on Electrical and Computer Engineering*, pp. 414–417, IEEE, 2007.

[10] S. Soylu, B. J. Buckham, and R. P. Podhorodeski, “Robust control of underwater vehicles with fault-tolerant infinity-norm thruster force allocation,” in *Proc. of OCEANS 2007*, IEEE, 2007.

[11] G. Conte, A. Serrani, and A. Perdon, “Rejecting the disturbances due to the umbilical's traction in rov's control,” in *Proc. OCEANS 1998*, vol. 3, pp. 1245–1249, IEEE, 1998.

[12] R. Kalman, “A new approach to linear filtering and prediction problems,” *Journal of Basic Engineering*, pp. 35–46, March 1960.

[13] H. Cox, “On the estimation of state variables and parameters for noisy dynamic systems,” *IEEE Transactions on Automatic Control*, vol. AC-9, pp. 5–12, Jan. 1964.

[14] B. Buckham, F. R. Driscoll, and M. Nahon, “Development of a finite element cable model for use in low-tension dynamics simulation,” *Journal of Applied Mechanics, Transactions ASME*, vol. 71, no. 4, pp. 476–485, 2004.

[15] S. Prabhakar, “Dynamics modeling and control of variable length remotely operated vehicle tether,” Master's thesis, University of Victoria, 2005.

[16] D. Steinke, “Design and simulation of a kalman filter for rov navigation,” Master's thesis, University of Victoria, 2005.

[17] L. Chauvier, G. Damy, J. Gilbert, and N. Pichon, “Optimal control of a deep-towed vehicle by optimization techniques,” in *Proc. OCEANS 1998*, vol. 3, pp. 1634–1639, IEEE, 1998.

[18] P. Williams, “Towing and winch control strategy for underwater vehicles in sheared currents,” *International Journal of Offshore and Polar Engineering*, vol. 16, no. 3, pp. 218–227, 2006.

[19] E. Dahlin, R. Ziemer, W. Wickstrom, and M. Horner, “Designing and tuning digital controllers,” *Instruments and Control Systems*, vol. 41, pp. 87–91, July 1968.

[20] T. Delmer, T. Stephens, and J. Tremills, “Numerical simulation of cable-towed acoustic arrays,” *J. Ocean Engineering*, vol. 15, no. 6, pp. 511–548, 1988.

[21] J. Zand, B. J. Buckham, D. Constantinescu, and S. Prabhakar, “Ship and winch regulation for remotely operated vehicle's waypoint navigation,” *International Journal of Offshore and Polar Engineering*, vol. 19, pp. 214–223, September 2009.

[22] M. Flagg, “Divetracker: characteristics and applications of an advanced dive mission control system,” in *Proc. OCEANS 1995*, vol. 3, pp. 1549–1556, IEEE, 1995.

[23] A. Alcocer, P. Oliveira, and A. Pascoal, “Study and implementation of an ekf gib-based underwater positioning system,” *Control Engineering Practice*, vol. 15, no. 6, pp. 689–701, 2006.

[24] J. Kinsey, R. M. Eustice, and L. L. Whitcomb, “A survey of underwater vehicle navigation: Recent advances and new challenges,” *Proc. IFAC*, vol. 7, 2006.

[25] M. Blain, S. Lemieux, and R. Houde, “Implementation of a rov navigation system using acoustic/doppler sensors and kalman filtering,” in *Proc. OCEANS 2003*, vol. 3, pp. 1255–1260, IEEE, 2003.

[26] E. Bachmann, R. McGhee, R. Whalen, R. Steven, R. Walker, J. Clynch, A. Healey, and X. Yun, “Evaluation of an integrated gps/ins system for shallow-water

auv navigation (sans)," in *Proc. Symposium on Autonomous Underwater Vehicle Technology*, pp. 268–275, IEEE, 1996.

[27] G. Ramadass, V. Jayakumar, S. Zacharia, S. Ramesh, S. Ramji, A. Nosov, V. Kuznetsov, S. Dremuchev, K. Kuznetsov, and A. Paramanov, "Integrated navigation system for remotely operable vehicle for 6000 m water depth," in *Proc. OCEANS 2007*, pp. 1038–1042, IEEE, 2007.

[28] K. Kim, P.-M. Lee, K. C.-M. Lee, B.-H. Jun, K. H.-T. Choi, J.-H. Lee, and S.-C. Ryu, "Underwater navigation based on the multiple sensor fusion for the deep-sea uuv system, hemire and henuvy," in *Proc. OCEANS 2007*, pp. 222–227, IEEE, 2007.

[29] M. B. Larsen, "High-performance doppler-inertial navigation - experimental results," in *Proc. OCEANS 2000*, vol. 2, pp. 1449–1456, IEEE, 2000.

[30] R. Hartman, W. Hawkinson, and K. Sweeney, "Tactical underwater navigation system (tuns)," in *Proc. Position Location and Navigation Symposium*, pp. 898–911, IEEE, 2008.

[31] G. Kantor, N. Fairfield, D. Jonak, and D. Wettergreen, "Experiments in navigation and mapping with a hovering auv," *Tracts in Advanced Robotics*, vol. 42, pp. 115–124, 2008.

[32] D. Leader, *Kalman Filter Estimation of Underwater Vehicle Position and Attitude Using a Doppler Velocity Aided Inertial Motion Unit*. PhD thesis, MIT, 1994.

[33] P.-M. Lee and B.-H. Jun, "Pseudo long base line navigation algorithm for underwater vehicles with inertial sensors and two acoustic range measurements," *Ocean Engineering*, vol. 34, pp. 416–425, 2007.

[34] R. Marthiniussen, J. Faugstadmo, and H. Jakobsen, "Hain: an integrated acoustic positioning and inertial navigation," in *Proc. OCEANS 2004*, vol. 3, pp. 1620–1628, IEEE, 2004.

[35] G. Grenon, P. An, S. Smith, and A. Healey, "Enhancement of the inertial navigation system for the morpheus autonomous underwater vehicles," *Journal of Oceanic Engineering*, vol. 26, pp. 548–60, Oct. 2001.

[36] X. Yun, G. Hernandez, E. Bachmann, R. McGhee, and A. Healey, "An integrated gps/ins navigation system for small auvs using an asynchronous kalman filter," in *Proc. Workshop on Autonomous Underwater Vehicles*, pp. 43–49, IEEE, 1998.

[37] T. Casey, B. Guimond, and J. Hu, "Underwater vehicle positioning based on time of arrival measurements from a single beacon," in *Proc. OCEANS 2007*, IEEE, 2007.

[38] A. Gadre and D. Stilwell, "A complete solution to underwater navigation in the presence of unknown currents based on range measurements from a single location," in *Proc. International Conference on Intelligent Robots and Systems*, pp. 1420–1425, IEEE, 2005.

[39] O. Hegrenaes, E. Berglund, and O. Hallingstad, "Model-aided inertial navigation for underwater vehicles," in *Proc. International Conference on Robotics and Automation*, pp. 1069–1076, IEEE, 2008.

[40] G. Jo and H. S. Choi, "Velocity-aided underwater navigation system using receding horizon kalman filter," *Journal of Oceanic Engineering*, vol. 31, no. 3, pp. 565–573, 2006.

[41] S. Hou, S. Peng, Z. Yan, and W. Zhang, "Research on the error model of ins/dvl system for autonomous underwater vehicle," in *Proc. International Conference on Automation and Logistics*, pp. 201–206, IEEE, 2008.

[42] B. Jalving and K. Gade, "Positioning accuracy for the hugin detailed seabed mapping uuv," in *Proc. OCEANS 1998*, pp. 108–112, IEEE, 1998.

[43] D. Steinke and B. Buckham, "A kalman filter for the navigation of remotely operated vehicles," in *Proc. OCEANS 2005*, vol. 1, pp. 581–588, IEEE, 2005.

[44] M. Vaz and M. Patel, "Transient behaviour of towed marine cables in two dimensions," *Applied Ocean Research*, vol. 17, no. 3, pp. 143–143, 1995.

[45] S. Hopland, "Investigation of cable behaviour in water during laying of fiberoptic submarine cables," *Proc. International Wire and Cable Symposium*, pp. 734–39, 1993.

[46] A. Gelb, J. F. Kasper, R. A. Nash, C. Price, and A. A. Sutherland, *Applied Optimal Estimation*. The M.I.T. Press, 1974. pp. 107-134, 182-190.

[47] P. S. Maybeck, *Stochastic Models, Estimation, and Control*. Academic Press, 1979. pp. 220-236.

[48] J. V. Candy, *Signal Processing: The Model-Based Approach*. McGraw-Hill, 1986. pp. 93-123.

Appendix A. Parameter Standard Deviations

For independently determined coefficients, such as added mass, the population standard deviation estimate is the ratio of output standard deviation to the input standard deviation. Assuming the variance of the data collected for the parameter identification is equal to the variance of the population of the ROV dynamics, equation (A.1) was used to calculate the estimate[1].

$$\hat{\sigma}_{\hat{\beta}} = \frac{s}{\sqrt{\sum (x_i - \bar{x})^2}} \tag{A.1}$$

The standard deviation estimate of parameters identified in pairs (such as quadratic drag) is more complicated, so the Matlab function *regstats* was used to perform the calculation. In this case the uncertainty in one parameter is closely coupled to uncertainty in the other parameter. Therefore, once one parameter is quantified (i.e. D_{uu}), regression must be performed again to find the other parameter's value (i.e. D_u) and standard deviation.

[1] J. L. Devore. *Probability and Statistics: For Engineering and The Sciences*. Brooks/Cole, 2004. pp. 522.

Parameter	Symbol	Best Estimate Kalman Model	Standard Deviation	Perturbed Estimate Simulation Model
Surge Hydrodynamic Drag	D_u	88.9	20.3	109.2 N/(m/s)
	D_{uu}	183.7	19.3	
		(164.9)	(4.6)	169.5 N/(m/s)^2
Sway Hydrodynamic Drag	D_v	86.5	37.4	123.9 N/(m/s)
	D_{vv}	541.9	62.6	
		(480.5)	(12.6)	493.1 N/(m/s)^2
Heave Hydrodynamic Drag	D_w	173.2	52.7	225.9 N/(m/s)
	D_{ww}	230.2	129.9	
		(105.2)	(35.4)	140.7 N/(m/s)^2
Surge Inertia	M_u	281.0	10.5	291.5 kg
Sway Inertia	M_u	223.8	22.2	246.1 kg
Heave Inertia	M_u	509.6	20.0	529.6 kg

Table A-1. Simulation Parameters. The least squares fits of the parameter identification data were used for the Kalman filter model, so the parameters used for the simulation model were perturbed by one standard deviation. Bracketed quantities are the unbiased estimate once the other parameter is perturbed.

Appendix B. Tether Material Properties

Material properties of the Falcon™ ROV's fibre-optic tether were measured with force-deflection tests. The tether provides power to the ROV through 4 large stranded copper wires and communication with 2 small fibre-optic lines and two small electrical signal wires. These wires are wrapped in a Vectran™ braided strength lining and two polyethylene jacket layers. Figure B-1 shows the cross-section of the tether.

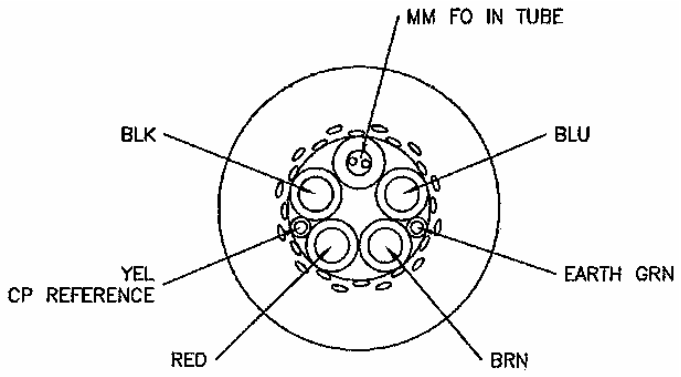

Figure B-1. Cross-section of the Falcon™ ROV's Tether. (Adapted from Seaeye Falcon™ Technical Manual)

B.1 Torsional Stiffness

Torsional stiffness relates how much an object twists to the torque applied. The elastic equation uses the product of Modulus of Rigidity, *G*, and the Polar Moment of Inertia of the cross-section, *J*, to model this relationship.

$$\phi = \frac{TL}{JG} \tag{2.1}$$

The product *JG* is the material property needed to model torsional stiffness in the tether. This property was measured by clamping one end of a 0.545m section of tether and applying torque to the other end. Torque was applied by applying small weights to a 0.125m lever arm attached to the free end of the tether.

Load, F (N)	Deflection, δ (mm)
0	-45
1	-30
2	-5
1	-15
0	-30
1	-7
2	8
3	33

Table B-1. Torsional Deflection Data. Loads were applied to a 0.125m lever arm and the load deflections were measured.

Angle of twist, ϕ, is calculated from the ratio of load deflection to lever arm length, l_{arm}.

$$\phi = \sin^{-1}\frac{\partial}{l_{arm}} \tag{2.2}$$

Applied torque was calculated by applying the cross-product of load and lever arm.

$$T = F \cdot l_{arm}\cos(\phi) \tag{2.3}$$

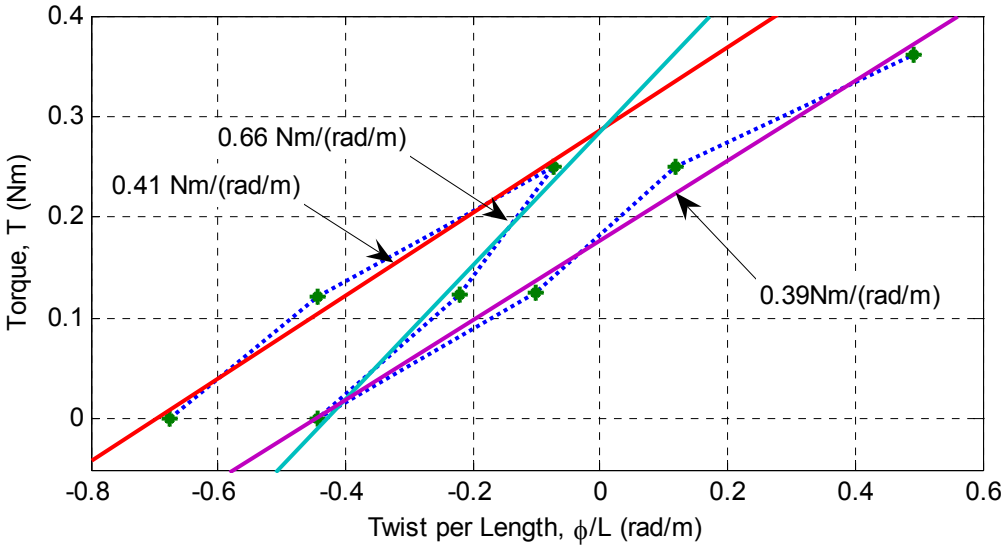

Figure B-2. Torque-Rotation Test to Identify Tether Torsional Stiffness. Notice the hysteresis present due to strong tether damping. Measured data (dots) is fitted with linear regression to estimate slope. An average slope of 0.5 Nm/(rad/m) is selected as the torsional stiffness.

The unbonded nature of the internal wires and plasticity of the polyethylene jackets are the likely cause of the hysteresis. Torsional stiffness is approximated as having a constant value of 0.5 Nm^2.

B.2 Bending Stiffness

Bending stiffness denotes the axial deflection of the tether resulting from moments about a radial direction. The elastic flexure equation uses Modulus of Elasticity, *E*, and Moment of Inertia, *I*, to model the relationship.

$$\partial = \frac{F \cdot l^3}{48EI} \tag{2.4}$$

The product *EI* was identified through a series of force deflection tests, where a 0.50m section of tether was supported at both ends and a load was applied at the center. The defection model equation for this configuration is used to calculate *EI* from the test data.

Load, F (N)	Deflection, δ (mm)
0	-5
2	5
4	15
6	25
8	40
10	60
8	60
6	55
4	50
2	40
0	30

Table B-2. 3-Point Bending Test Data. Loads were applied to the centre of 0.5m span.

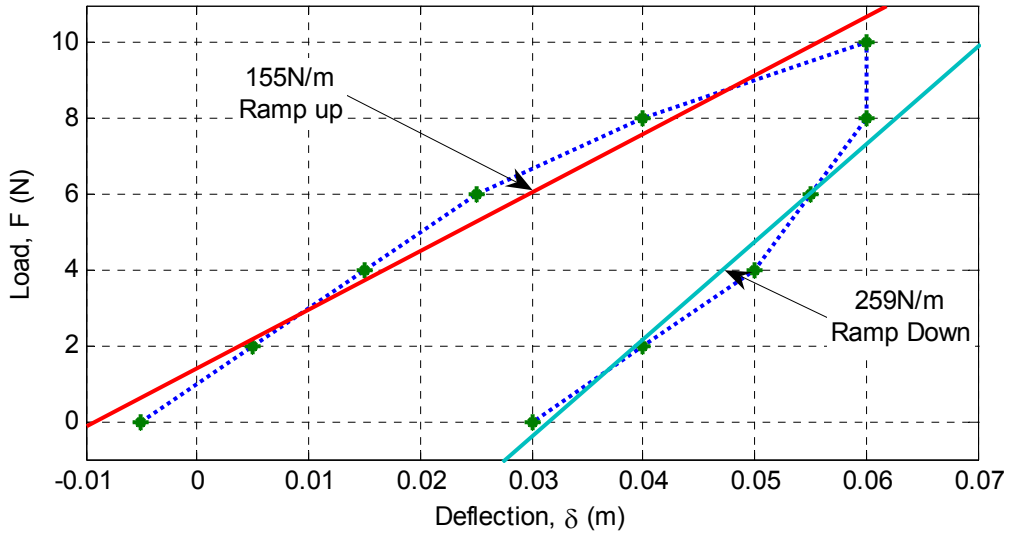

Figure B-3. 3-Point Bending Test to Identify Bending Stiffness *EI*.

Isolating *EI* in Equation reveals the slope of a force vs. deflection plot is related to *EI* by a constant factor of $L^3/48$.

Quantity	Symbol	Ramp Up	Ramp Down	Average
Force per Deflection	F/δ	155 N/m	259 N/m	207 N/m
Bending Stiffness	EI	0.40 Nm^2	0.67 Nm^2	0.54 Nm^2

Table B-3. Bending Stiffness

B.3 Axial Stiffness

Axial stiffness is calculated by assuming the tether stiffness is spatially uniform and algebraically manipulating the bending stiffness.

$$EA = EI \cdot \frac{A}{I} = EI \cdot \frac{4}{r^2} \tag{2.5}$$

Quantity	Symbol	Value
Axial Stiffness	EA	4.3 x 10^4 N

Table B-4. Axial Stiffness

Contrary to the assumption made in this calculation, the tether properties vary over the cross-section, so the axial stiffness value may contain inaccuracies. However, directly identifying the axial stiffness with an axial force – deflection test is also poorly conditioned since the elongations anticipated from typical tether loadings are less than 0.5%.